A Shape Memory Alloy-based biomimetic robotic Hand: design, modelling and experimental evaluation

Dissertation

zur Erlangung des Grades

des Doktors der Ingenieurwissenschaften

der Naturwissenschaftlich-Technischen Fakultät

der Universität des Saarlandes

von

Filomena Simone

Saarbrücken

2021

Tag des Kolloquiums:	11. März 2021
Dekan:	Prof. Dr. Jörn Erik Walter
Berichterstatter/in:	Prof. Dr.-Ing. Stefan Seelecke
	Prof. Dr.-Ing. Matthias Nienhaus
Vorsitzende/r:	Prof. Dr.-Ing. Rainer Müller
Akad. Mitarbeiter/in:	Dr. Michael Roland

Kurzfassung

Jedes Jahr werden weltweit bei mehr als 400.000 Menschen Amputationen der oberen Gliedmaßen durchgeführt. Prognosen gehen davon aus, dass sich diese Zahl bis zum Jahr 2050 verdoppeln wird. Hauptursachen der Amputationen sind Infektionen, Unfälle, Krebs oder Durchblutungsstörungen. Der Zugang zu prothetischer Versorgung ist besonders in den Entwicklungsländern stark eingeschränkt. Dies liegt vor allem an den hohen Kosten sowohl der im Handel erhältlichen Prothesen als auch des Rehabilitationsprozesses, den jeder Prothesenträger durchlaufen muss. Neben den hohen Kosten haben kommerziell erhältliche Handprothesen aufgrund ihres hohen Gewichts, des lauten Betriebes und auch des unnatürlichen Gefühls hohe Ablehnungsraten. Um diese Einschränkungen zu überwinden, wurden neue Materialien, wie z.B. Formgedächtnislegierungen (SMAs), als potenzielle Materialien für den Antrieb von Prothesen untersucht .

Um einen Beitrag zur Entwicklung von leistungsfähigen und erschwinglichen Handprothesen zu leisten, wird in dieser Arbeit die Entwicklung eines neuartigen und kostengünstigen Fünf-Finger-Handprototyps vorgestellt, der durch Drähte aus Formgedächtnislegierungen aktiviert wird. Die Doktorarbeit beginnt mit der Beschreibung der ersten Generation eines SMA-aktivierten Fingers. Zuerst wird der Aufbau und das Wirkungsprinzip des SMA Fingers erläutert und die Leistungs- und Bewegungsfähigkeit des Systems untersucht sowie Vor- und Nachteile des Prototyps dargestellt.

Anschließend, um die erreichbare Leistungsfähigkeit zu verbessern, wird eine zweite Generation von SMA-gesteuerten Fingern vorgestellt, die eine vollständig in 3D gedruckte Struktur aufweisen. Diese Fünffinger-Handprothese mit inhärent elastischen Fingern ermöglicht nicht nur das Greifen unterschiedlich geformter Objekte sondern auch das Heben und Halten schwerer Gegenstände.

Dieser neuartige Prototyp wird mit den wichtigsten bisher entwickelten Prothesen verglichen und die relevanten Vorteile insbesondere in Bezug auf geräuschlose Ansteuerung, Kosten, Gewicht, Reaktionszeit und Kraft hervorgehoben.

Abschließend wird ein Finite-Elemente-Modell entwickelt, mit Hilfe dessen die Fingerstruktur weiter optimiert und die Leistungsfähigkeit des SMA-Fingers noch verbessert werden kann.

Zusätzlich wird ein Konzentriertes-Parameter-Modell formuliert, um, in der Zukunft, eine leichtere Regelung des Systems zu ermöglichen. Dieses ist notwendig, da der SMA-Finger starke Nichtlinearitäten aufweist, die auf das hysteretische Verhalten der Formgedächtnislegierung zurückzuführen sind.

Abstract

Every year more the 400,000 people are subject to an upper limb amputation. Projections foresee that this number may double by the 2050. Infections, trauma, cancer, or complications that arise in blood vessels represent the main causes for amputations. The access to prosthetic care is worldwide extremely limited. This is mainly due to the high cost both of commercially available prostheses and of the rehabilitation procedure which every prostheses user has to endure. Aside from high costs, commercially available hand prostheses have faced high rejection rates, mainly due to the their heavy weight, noisy operation and also to the unnatural feel of the fingers. To overcome these limitations, new materials, such as Shape Memory Alloys (SMAs), have been considered as potential candidate actuators for these kind of devices.

In order to provide a contribution in the development of performant and easily affordable hand prostheses, the development of a novel and cost-effective five-fingered hand prototype actuated by Shape Memory Alloy (SMA) wires is presented in this work. The dissertation starts with the description of a first generation of a SMA actuated finger. Structure assemblage and performances in term of force, motion and reactiveness are investigated to highlight advantages and disadvantages of the prototype.

In order to improve the achievable performances, a second generation of SMA actuated finger having soft features is introduced. Its structure, a five-fingered hand prosthesis having intrinsically elastic fingers, capable to grasp several types of objects with a considerable force, and an entirely 3D printed structure is then presented. Comparing this prototype with the most important prostheses developed so far, relevant advantages especially in term of noiseless actuation, cost, weight, responsiveness and force can be highlighted.

A finite element based framework is then developed, to enable additional structure optimization and further improve the SMA finger performances. On the same time, a concentrated parameters physics-based model is formulated to allow, in the future, an easier control of the device, characterized by strong nonlinearities mainly due to the Shape Memory alloy hysteretic behavior.

Maybe what I really wanted was to prove I could do things right,
so when I looked in the mirror,
I'd see someone worthwhile.

[Chinese ballad]

Table of content

Introduction

During the late 1950s, the need to design devices capable of reproducing the functionality and versatility of the human hand gained the interest of many researchers. To achieve good manipulation capability and restrain the weight of the overall structure, several anthropomorphic hands have been proposed [1]–[8]. All these hands are actuated by electric motors, and are capable of high forces, high actuation speed, and great versatility [9]. However, these kind of prosthesis encountered high rejection rates by the users, mainly due to the rigidity of the artificial hands, their low grasping stability, their heavy weight, the noisy operation of actuators, as well as the unnatural feel and robot-like motion of the fingers [10]–[14].

A possible solution to overcome the limitation of electric motors consists of using pneumatic actuators in the gripping system. This leads to various advantages over conventional electric motor technology, such as mechanical simplicity and higher forces [15]–[18]. However, pneumatic solutions are unsuitable for applications in which a limited actuator volume is required, due to the need for a compressed air source, the requirement of bulky valves (which inevitably increase the weight of the device), the high noise production during actuation, and the compressible nature of gas that makes it difficult to achieve accurate control of position and/or force. Moreover, the need of pressurized air implies that additional masses, such as the air cylinder, need to be added to the overall system [16]–[20]. Price is another important aspect to not neglect. All commercially available hand prostheses are very expensive and, most of the time, the amputee cannot effort the price of both the device and the rehabilitation. Therefore, all currently used actuation technologies show some inherent limitations when used in prosthetic applications.

The main focus of this thesis is on Shape Memory Alloy (SMA). These materials, typically made of Ni–Ti alloys, undergo a phase transformation when exposed to heat [21]. Such a phase transformation results into a controllable contraction, which can be used for actuation. SMA technology is potentially attractive for the realization of artificial hands. In fact, SMA wires can be easily integrated in mechanical structures without requiring large amount of space and complex gearing mechanisms, therefore favoring the optimization of production costs. For these reasons, various prototypes of SMA-based hand prostheses have been developed in recent years [22]–[26]. Although preliminary results have shown high potential of SMA technology for prosthetic devices, none of the SMA prosthetic hands presented in literature so far can be considered mature enough to support amputees in typical real life operations. This is mainly due to the limited performance of the current prototypes [13], [26].

Following the research trends of recent literature on SMA robotic hands, this dissertation aims at overcoming some limitations of the existing active hand prosthesis, presenting a new prototype of SMA actuated hand.

The reminder of this work is organized as follow. In the first Chapter SMA materials are introduced and their working principle exposed. The single crystal and polycrystal versions of the MAS model for Shape memory alloy is then formulated. A first concept for cost effective 3D printed SMA hand having three active fingers is described and its performances evaluated in Chapter 2. A second improved version of the SMA hand with soft features (SMA Soft Hand) is described in Chapter 3.

In order to improve the proposed hand prototypes structure and performances, a finite element model is formulated in Chapter 4. A concentrated parameters physics-based model of the same structure, suited for control purposes and implemented in MATLAB environment is presented in Chapter 5.

In summary, this thesis demonstrates the effectiveness of SMA actuator technology when integrated in complex structure such as hand prostheses. It is also demonstrated how physics-based models are eligible to describe articulated systems actuated by shape memory alloys. This research work aims at increase the spreading of devices based on Shape Memory Alloys and gives a contribution in the design of price-affordable and functional prosthetic hands.

1 Shape Memory Alloys

Shape memory alloys are Nickel-Titanium (Ni-Ti) based materials able to remember their original un-deformed shape [21]. Therefore they are qualified as “smart materials”.

1.1 Material structure and operating principle

The physical key to “shape memory” lies in a phase transformation between a parent phase called austenite (A) and a produced phase called martensite (M) [27], [28]. For SMAs, this phase transformation involves a change of crystalline lattice between the phase A, also known as the “high temperature” phase, and a phase M, also known as the “low temperature” phase.

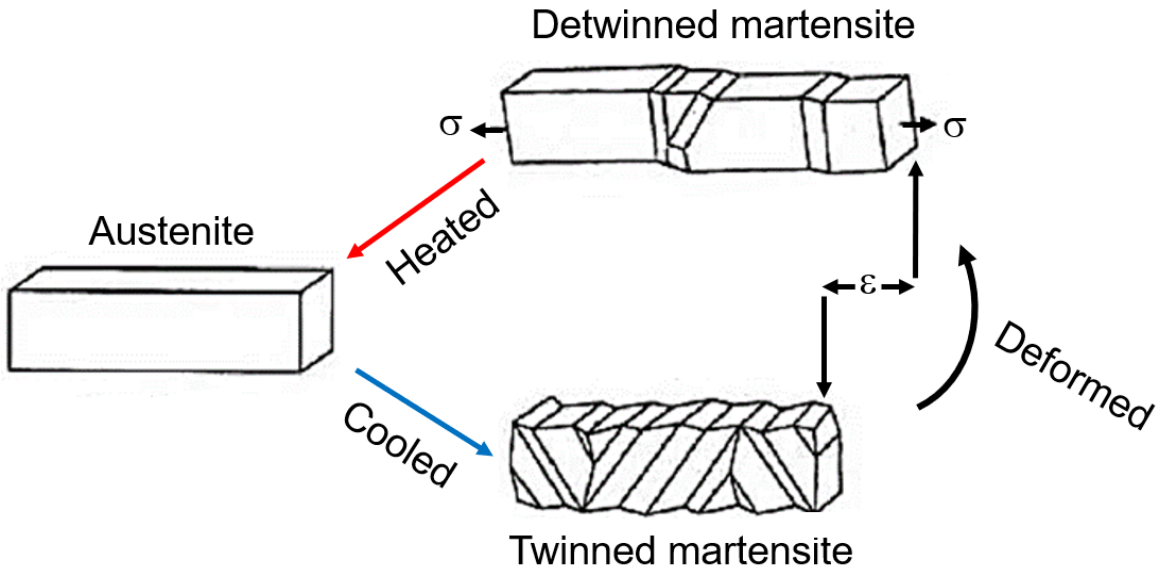

Figure 1.1: SMA working principle

When the SMA material is undeformed and at ambient temperature, in its lattice structure, several martensitic variants having different orientations and a rectangular shape are displaced, as shown in Figure 1.1. This configuration is called *Twinned Martensite* [29]. If a tensile stress is applied (σ), the variants are forced to change orientation according to the same preferred configuration (*Detwinned Martensite*). As result, a strain ε is induced in the alloy along the applied stress direction (Figure 1.1) and thus an elongation of the material occurs. In this status, if the material is heated up above a predefined temperature (called austenite start temperature A_s), a phase transformation is enabled in the material and the martensitic variants change in austenitic ones. If heating is continuously supplied, the material structure will endure the transformation until the austenite finish temperature (A_f)

is reached. At this point, the crystalline lattice is completely in austenitic phase. Since the austenitic variants have a square shape (see Figure 1.2), after the phase transformation, the material reduces its length. In this state, if the external stress is removed and the material cooled down to the martensitic finish temperature (M_f), the SMA alloy will regain the initial twinned martensite configuration, which has the same external dimensions of the austenite state material (due to the different orientations of each martensitic variant), but a different lattice structure (Figure 1.1). If the applied stress σ is maintained during the cooling process, the SMA alloy will come back to the detwinned martensite configuration. Under these conditions, a change in the alloy dimensions will be observed during the material phase transformation.
To have a better overview of the articulated behavior of these alloys, we can schematize it in a stress-strain diagram. This diagram is visible in Figure 1.2 and it shows a stress-strain hysteresis depending on temperature [30]. In principle, we can distinguish different working mechanisms: the one-way, the two-way, the pseudo-elastic and the rate effect [31], [32]. In the followings Sections, each of these effects will be described in detail.

1.1.1 One-way shape memory alloy effect

The focus of this Section is on the one-way shape memory effect (OWSME).
The phenomenon is described in Figure 1.2, where the SMA behavior is depicted depending on stress, strain and temperature. At room temperature (around 290K), without any external stress applied, the material crystal lattice shows a twinned martensite configuration (1). If an external stress is applied and therefore the material is loaded, the variants are forced to change and uniform their orientation (detwinned martensite configuration (2)). If now the external stress removed, the material keeps this configuration without recovering the twinned martensite one (3). In order to regain the original shape, the material has to be heated up to a temperature above A_f and let the phase transformation completely occur (4). The austenite variants have a different lattice structure but the same macro shape of the material in the twinned martensite configuration (see Figure 1.1). This behavior is called one-way shape memory. The material, indeed, remembers only “one shape” (the austenitic form) and, after any mechanical deformation, it needs to undergo a temperature induced phase transformation to recover the “memorized” original shape (Figure 1.3, left hand side).

1.1.2 Two-way shape memory effect

In Section 2.1, the one-way shape memory effect has been described as the ability of the material to remember the shape of the austenitic phase. In this Section the Two Way Shape Memory Effect (TWSME) will be described [33]. This effect cannot be listed among the intrinsic material properties (as for the OWSME), but it can be exhibited after specific thermomechanical treatments known as training procedures [34], [35].

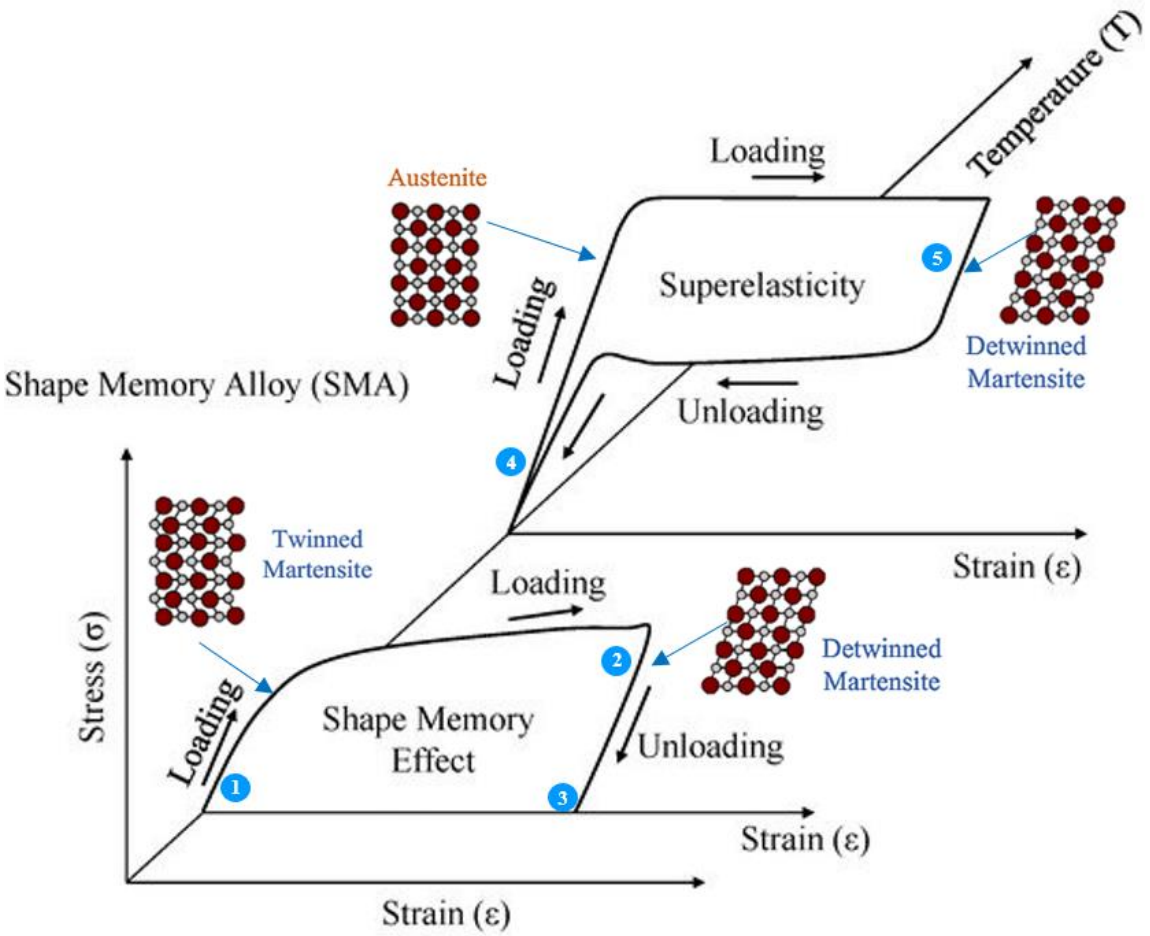

Figure 1.2: SMA behavior depending on temperature, stress and strain.

The TWSME consists in the capability of the material to remember both a desired martensite and austenite shape by changing the alloy temperature and inducing a phase transformation, without applying any external load or stress. The working principle is depicted in Figure 1.3, right hand side. At room temperature, the SMA material displays a predefined shape gained after an adequate training process. Increasing the temperature above the austenite start temperature A_s, the alloy undergoes a phase transformation and its changing in shape begins.

The complete transformation occurs when the temperature reaches the A_f value. In this situation, the material has achieved a perfect "clip shape" (according to Figure 1.3, right-hand side). When the cooling process starts and the alloy reaches the martensite start temperature M_s, the variants gradually reshape into a detwinned martensite configuration. This process is fully accomplished when the martensite finish temperature M_f *is* reached and the material then is completely back to its original starting configuration.

Figure 1.3: The three main effects in SMA materials. (Left hand side) One-way shape memory effect. (Center part) Pseudo-elasticity memory effect. (Right hand side) Two-way Memory effect.

1.1.3 Pseudo-elastic effect

The pseudo-elasticity is an additional effect of SMA materials, which describes the ability of these alloys to undergo a phase transformation without any change in the external temperature. This phenomenon occurs when the alloy is at a higher temperature of A_f and therefore, the material lattice is in austenite configuration, as shown in Figure 1.3, center part. In this situation, if an external stress is applied to the structure, a deformation and a transformation of the lattice crystals from austenitic to martensitic configuration are induced. Referring to Figure 1.3, center part, if the austenitic clip is deformed, a structural and phase transformation occurs in the material, changing it in a detwinned martensite deformed clip. If the stress is then removed, the material recovers automatically the austenitic clip shape. The pseudo-elastic effect is systematically described in Figure 1.2. The initial material configuration is defined by the load-free state at point 4. If a loading process is performed, the phase transformation occurs until the material presents only detwinned martensitic variants (Figure 1.2, point 5). Strains up to the 12% can be achieved without experiencing plastic deformations of the material. When the material is unloaded, according to the bottom hysteresis branch behavior, it recovers a fully austenitic lattice.
Ni-Ti alloys are the most widespread shape memory material, but, on the market, different kind of shape memory alloys are also available [36]. Each of them has different thermo-mechanical properties, in dependence from its material structure. For Ni-Ti alloys, the austenitic finish temperature is in the range of 90° C and therefore they need to be heated up above this temperature in order to show a pseudo-elastic behavior. For many different other shape memory alloys, the A_f is around 0°C and therefore at room temperature they are already in austenitic configurations.

1.1.4 Rate dependency effect

Before introducing the rate effect, let us recall that the forward transformation into martensite is exothermic (heat is released from the alloy to the environment) while the reverse transformation into austenite is endothermic, (heat is required and, in general, absorbed from the surroundings) [37]. As described in Section 2.3, if the external temperature is constant and above the A_f, the SMA alloy will show a pseudo-elastic behavior according to Figure 1.2 (points 4-5).

If the material is loaded, thermal energy can be added to the alloy if the heat generated during the exothermic forward transformation is not dissipated. If loading is performed slow enough, convective and conductive processes will remove this additional heat without noticeably raising the specimen temperature. If loading or unloading progresses too rapidly, the temperature of the specimen will rise during loading and fall during unloading, violating any isothermal assumptions [21]. Loading/unloading rates can change the shape of the hysteresis according to Figure 1.4. In this picture, three hystereses obtained for low strain rate (left hand side) and for higher rates (middle and right-hand side) are depicted. In case of low strain rate, the heat generated can be completely dissipated in the ambient surrounding the SMA material. Therefore, the process will occur under isothermal condition. In this case, the hysteresis presents a box-like shape and nearly flat plateaus during the phase transition. If fast loading/unloading processes are used, due to the heat increase during the process, the hysteresis will have a longer and bigger shape [38], [39].

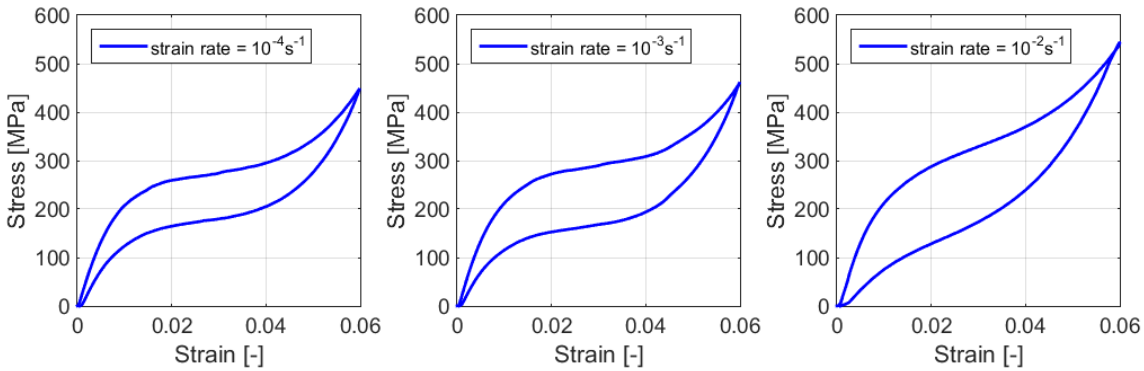

Figure 1.4: Rate effect on the SMA hysteresis shape. (Right hand side) Hysteresis related to a fast loading/ unloading process. (Left hand side) Hysteresis for a slow loading/unloading process under isothermal conditions.

Considering the stress-temperature relationship, a similar outcome can be achieved for external temperature below A_f, when the material does not show a pseudo-elastic behavior. In this case, if an external stress is acting on the material, the alloy variants are in the detwinned martensitic configuration (Figure 1.2 (point 3)). If the temperature raises with a slow rate, the phase transformation will occur slowly, such as it can be considered quasi-static. The stress-temperature hysteresis, in this case, will be shaped according with Figure 1.4, left hand side. On the other side, for high temperature rates, the phase transformation

will occur faster and the corresponding stress-temperature hysteresis will be wider and smoother, as shown in Figure 1.4, right hand side. These notions will be very important in Chapter 4, during the model parameter identification procedure.

1.2 Shape Memory Alloys Model

As stated in Section 1.1, SMA material exhibits a complex behavior, characterized by a temperature–dependent stress–strain hysteresis, which significantly complicates modeling and control of devices based on such technology. In literature, several constitutive models have been formulated to describe the behavior of SMA material, ranging from phenomenological to phase–space models and thermodynamic ones. Some important examples include models proposed by Boyd and Lagoudas [40], [41], Tanaka and Nagaki [42], Brinson [43],Liang and Rogers [44], Müller, Achenbach and Seelecke [45]–[47], and many others, e.g., [48]–[54].

Due to the high amount of computation effort required for the implementation of such models, they often appear as unsuitable for real–time applications. For this reason, most of the approaches presented in literature are based on black–box hysteresis operators, such as the ones proposed by Preisach [55]–[58], Krasnosel'skii–Pokrovskii [59], [60], and Prandtl–Ishlinskii [61]. These strategies lead in general to a highly accurate and computationally efficient description of the SMA hysteresis. On the other hand, this family of models is not well suited to predict the system behavior in response to change in external conditions (e.g., environmental temperature, deformation rate, load stress), since it lacks describing the underlying physical mechanisms. In order to use both a computationally efficient and a physics-based model, the Müller, Achenbach and Seelecke (MAS) model [62] will be introduced and used, in the next Chapters, for modeling purposes.

SMA materials are typically shaped in wires when used for actuation and sensing applications. Due to the wire geometry, typical application–oriented models are limited to the one–dimensional case. In general, when modeling the constitutive behavior of SMA alloys, a single–crystal (SC) approximation of the material structure is considered.

Quantitative predictions become poor in case the SMA material exhibit a polycrystalline (PC), rather than SC behavior. The use of one of the two versions, in general, is due to the desired level of the model accuracy and, above all, to the hysteresis shape to model. For these reasons, in the following, both single–crystal and polycrystalline SMA models will be described.

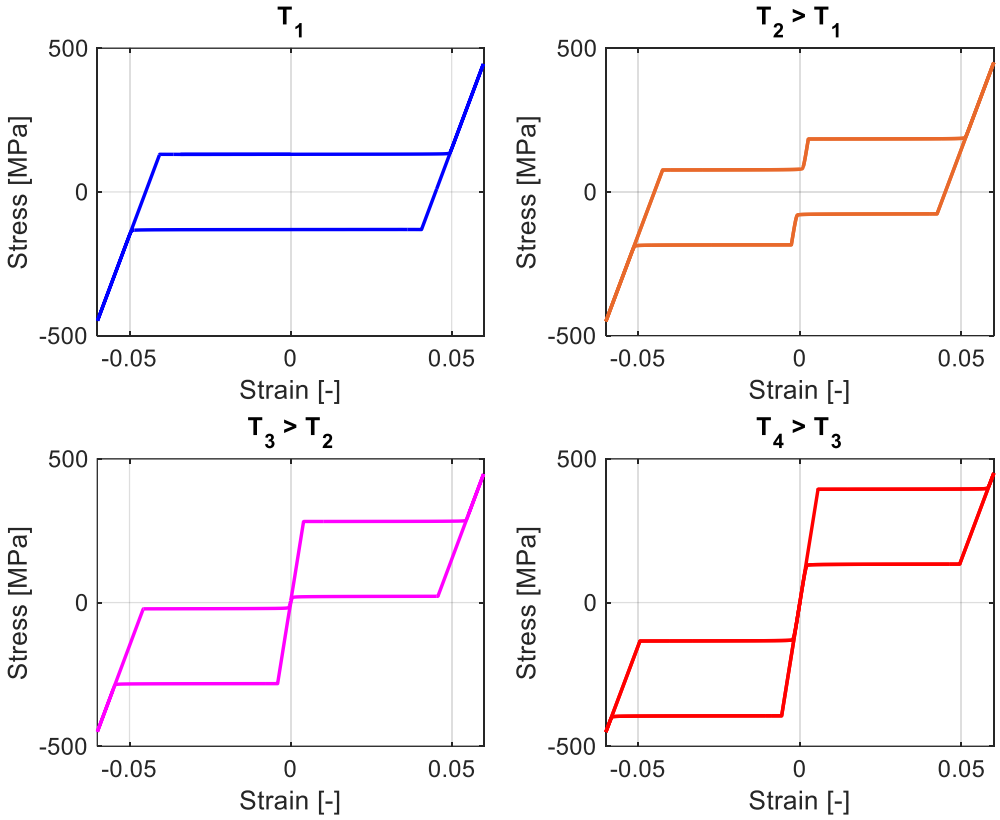

Figure 1.5 Simulated stress–strain hysteresis of SMA at different temperatures, using the SC model version.

1.2.1 Single-crystal model

This single-crystal version of the MAS model allows to describe the dynamic response and the thermo-mechanical coupling of one-dimensional SMA systems under a uniaxial load, within a thermodynamically consistent framework.

The MAS model considers a mesoscopic lattice layer as basic SMA element. It is assumed that three variants exist in the material crystal lattice, i.e., austenite *A* and two martensitic variants, having different orientations, M_+ and M_-. To each variant, a phase fraction is associated. The following relationship holds among phase fractions

$$x_A + x_+ + x_- = 1, \tag{1.1}$$

where x_A, x_+ and x_- are the phase fraction associated to *A*, M_+ and M_- respectively. To describe the phase fraction kinetics, the following equations are used

$$\frac{\partial x_+}{\partial t} = -p^{+A} x_+ + p^{A+} x_A, \tag{1.2}$$

$$\frac{\partial x_-}{\partial t} = -p^{-A} x_- + p^{A-} x_A, \tag{1.3}$$

where $p^{\alpha\beta}$ is the transition probability from phase α to phase β. Transition probabilities are derived via statistical thermodynamic considerations, and depend on both material stress σ and temperature T. They describe the probability for an ideal layer to overcome an energy barrier in the non-convex free-energy landscape. Their explicit expression is rather complex, and is omitted here for brevity (see [63] for details). The evolution of the temperature T in the SMA material is defined through the balance law of the internal energy, i.e.,

$$\rho c \frac{\partial T}{\partial t} = h\left(\frac{\partial x_+}{\partial t} + \frac{\partial x_-}{\partial t} \right) - \alpha_c S_v (T - T_0) + j(t) \quad , \tag{1.4}$$

where ρ is the material density, c is the specific heat, h is the latent heat of transformations, α_c is the heat transfer coefficient, S_v is the ratio between external surface and volume of the wire, and $j(t)$ is the volumetric density of Joule heating [64]. On the right-hand side of equation (1.4), the first term accounts for the rate-dependent heat generation and absorption due to the phase transformation, the second contribution represents the heat exchange between SMA and environment, and the last term represent the electric power density used as control input. Transition probabilities also depend on transformation stresses of austenitic and martensitic phases, given as follows

$$\sigma_A = \sigma_L + \frac{d\sigma}{dT}(T - T_L), \tag{1.5}$$

$$\sigma_M = \sigma_A - \Delta\sigma, \tag{1.6}$$

where σ_L is the transformation stress from martensite to austenite at reference temperature T_L, $d\sigma/dT$ is the gradient transformation stress with respect to the temperature, $\Delta\sigma$ is expressed as σ_A-σ_M and represents the hysteresis width. The model behavior is depicted in Figure 1.5, where the single-crystal SMA hysteresis is presented for different constant temperatures. It can be observed how increasing the temperature results in a splitting of the initial hysteresis loop into two separate hystereses, which move apart from each other's as the temperature further increase. The stress-strain SMA hysteresis, at different temperatures, simulated with the described model, is depicted in Figure 1.5.

*1.2.2 **Poly-crystal model***

Commercially available SMA wires exhibit a poly-crystal (PC) nature, due to inhomogeneities and to non–ideal material processing. As a result, the shape of the hysteresis is significantly more complex with respect to box shapes commonly used to model SC material. In addition, minor hysteresis loops appear when performing partial loading or unloading, further complicating the modeling of such material. To develop accurate simulation tools, a computationally efficient model, which takes into account the PC behavior of SMA material, is described in the following.

Recalling the MAS model formulation from the previous Section, equations (1.5)-(1.6) are valid only for its single-crystal version. In [62], to parametrize SMA polycrystallinity, it is

assumed that the transformation stresses depend not only on temperature, but also on the current material composition, i.e., the phase fractions. In addition, we point out that we are dealing with wire geometries, which cannot sustain compressive stresses. Since x_- is associated to a compressed state, for a wire we can assume that $x_- = 0$, and therefore the material composition is described by means of x_+ and x_A only. Under these assumptions, the transformation stresses of the polycrystalline SMA model are defined as follows:

$$\sigma_A(T, x_+) = \sigma_A(T_L, x_+) + \sigma_S(x_+)(T - T_L), \tag{1.7}$$

$$\sigma_M(T, x_+) = \sigma_M(T_L, x_+) + \sigma_S(x_+)(T - T_L), \tag{1.8}$$

Functions $\sigma_A(T_L, x_+)$ and $\sigma_M(T_L, x_+)$ describe the transformation stresses at reference temperature T_L, while the thermal scaling is accounted by the term proportional to $\sigma_S(x_+)$. This approach permits to represent a smooth, polycrystalline hysteresis in a computationally efficient way. By assuming $x_- = 0$ and also by considering equations (1.1) , (1.7) and (1.8), equations (1.2) - (1.4) can be rewritten as follows:

$$\frac{\partial x_+}{\partial t} = -p^{+A}(\sigma, x_+, T)x_+ + p^{A+}(\sigma, x_A, T)x_A \tag{1.9}$$

$$\rho c \frac{\partial T}{\partial t} = h\frac{\partial x_+}{\partial t} - \alpha_c S_v (T - T_0) + j(t), \tag{1.10}$$

$$\sigma = \frac{\varepsilon - \varepsilon_T x_+}{\dfrac{x_+}{E_M} + \dfrac{1 - x_+}{E_A}}, \tag{1.11}$$

Equations (1.9)-(1.11) completely describe the polycrystalline SMA model. We point out, however, that the presented approach permits to accurately describe the outer hysteresis loop only. In order to also predict internal hysteresis loops with great high accuracy, a bookkeeping algorithm has to be implemented [62]. For further information and details about the polycrystalline MAS model, please refer to [62].

1.3 SMA actuators based systems

In order to develop accurate simulation tools for model–based design optimization of real–life SMA devices, constitutive material models can be extended in order to describe the behavior of SMA devices, by properly including actuation and sensing dynamics, see, e.g., [63], [65]–[70].

The model presented in the previous Section permits the description of the intrinsic behavior of SMA material, i.e., it allows to simulate the resulting stress for a given strain and temperature. In order to use the model to simulate SMA wire actuators, we must properly relate material quantities (stress, strain, temperature) to corresponding measurable quantities (force, displacement, input power).

To convert stress σ into force *f*, and strain ε into wire length *l*, the following equations can be used:

$$f = \pi r_0^2 \sigma, \tag{1.12}$$

$$l = l_0 (1 + \varepsilon), \tag{1.13}$$

where r_0 and l_0 represent the cross–sectional radius and the length of the SMA wire in undeformed and fully austenitic phase. Note that we have adopted the notion of nominal stress, i.e., *f* is obtained as σ times the wire initial cross–sectional area rather than the current one, due to the relatively small strains involved within the considered material. It is possible to control the wire temperature by supplying an electric current and letting the resulting input power being the actuation signal. The relationship between input power and SMA temperature can be obtained by considering the internal energy balance equation, which results in the following PDE:

$$\rho_m V c \frac{\partial T}{\partial t} = -\alpha_c A_s (T - T_0) + J + \rho_m V H_+ \frac{\partial x_+}{\partial t}. \tag{1.14}$$

In (1.14), ρ_m is the volumetric mass density of the SMA wire, *V* is the wire volume ($V = \pi r_0^2 l_0$), *c* is the SMA specific heat, α_c is the convective cooling coefficient, A_s is the lateral surface of the SMA wire ($A_s = 2\pi r_0 l_0$), T_0 is the environmental temperature, *J* is the Joule heating, and finally H_+ represents the specific latent heats of phase transformations. The terms on the right–hand side of (1.14) represent the heat exchanged with the environment due to natural convection, the heat supplied to the wire via Joule effect, and the internal latent heat production due to M_+ phase transformation.
The overall SMA wire actuator model consists of a set of two PDEs, $T(0)$, $x_+(0)$, as initial conditions, as well as a profile for $l(t)$ or $J(t)$ for $t \geq 0$.

In many applications, we are interested in simulating the actuation stroke/force of SMA wires pre–loaded with a mechanical system, e.g., a mass–spring type of load or another SMA wire [65]. Simulations of SMA wires interacting with external mechanical systems can be easily performed within the proposed framework. In the following sub-sections, the SMA – spring and SMA-SMA configurations will be further analyzed.

1.3.1 SMA actuators: linear spring load

In this Section, the SMA – spring configuration will be investigated. In the system taken into account (see Figure 1.6), a SMA wire and a linear spring are arranged in agonistic configuration. When the SMA is activated, it undergoes a phase transformation, which leads to a shortening of its length. This effect causes the motion of the point P towards the reader´s left hand side and, thus, the elongation of the linear spring. As soon as the SMA

wire is deactivate, the spring restores its initial configuration and, on the same time, stretches the SMA wire, which recovers its initial martensitic length.

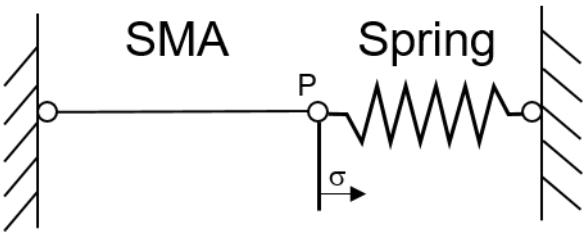

Figure 1.6: SMA wire preloaded with a linear spring.

A model of the overall system can be obtained by combining the SMA constitutive equations with the dynamic equation of the biasing system, which in the case of a mass–spring load is given as follows

$$m\ddot{l} + k\left(l - l_k\right) + f = 0, \tag{1.15}$$

where m, k, and l_k represent loading mass, spring stiffness, and spring pre–deflection, respectively. From the mechanical point of view, the working principle can be easily understood analyzing the diagrams in Figure 1.7. This picture represents a typical loading/unloading cycle in which the SMA wire is, at first, heated up above A_f, and then it is deactivated and cooled down by the air. This cycle is represented by a single-crystal SMA hysteresis, depicted for different temperatures, superimposed with a linear spring characteristic. For each configuration, the equilibrium solution is detected using the graphical method and, in the Figure 1.7, highlighted by a black circle. In the first situation (Figure 1.7, (A)), the wire is at room temperature and lays in equilibrium with a pre-compressed spring. The equilibrium point (the intersection between the two characteristics) is unique, and is located at the right-hand side branch of the SMA hysteresis.

The wire is in detwinned martensitic configuration. If the wire is activated via electric current, its temperature and transformation stress start to rise. Graphically, this effect is represented by a hysteresis, which starts to rise in the stress-strain diagram. Since the spring is not affected by this phenomenon, its characteristic remains unchanged. This leads to a shift of the equilibrium point according to the SMA wire behavior. In Figure 1.7 (B), the wire temperature is slightly increased and, thus, the equilibrium point is changed. In this configuration, the two characteristics intersect in two “possible” equilibrium points. Without any knowledge about the history of the full process, it would be impossible to understand which of the two points is the correct one. In this case, knowing that the temperature is increasing, we can easily assert that the point laying on the hysteresis bottom branch is the correct equilibrium point. If the temperature further increases, the equilibrium point keeps moving along the hysteresis bottom branch (Figure 1.7, (C)). When the temperature T_3 is reached (Figure 1.7, (D)), the point has reached the left hand side hysteresis branch, which means that the SMA wire is in austenitic configuration. During the wire cooling (Figure 1.7, (E-F)), the transformation stresses will start to decrease and

thus the hysteresis will move towards the bottom part of the stress-strain diagram. In this case, the equilibrium point will move along the upper hysteresis branch as shown in Figure 1.7, (E-F).

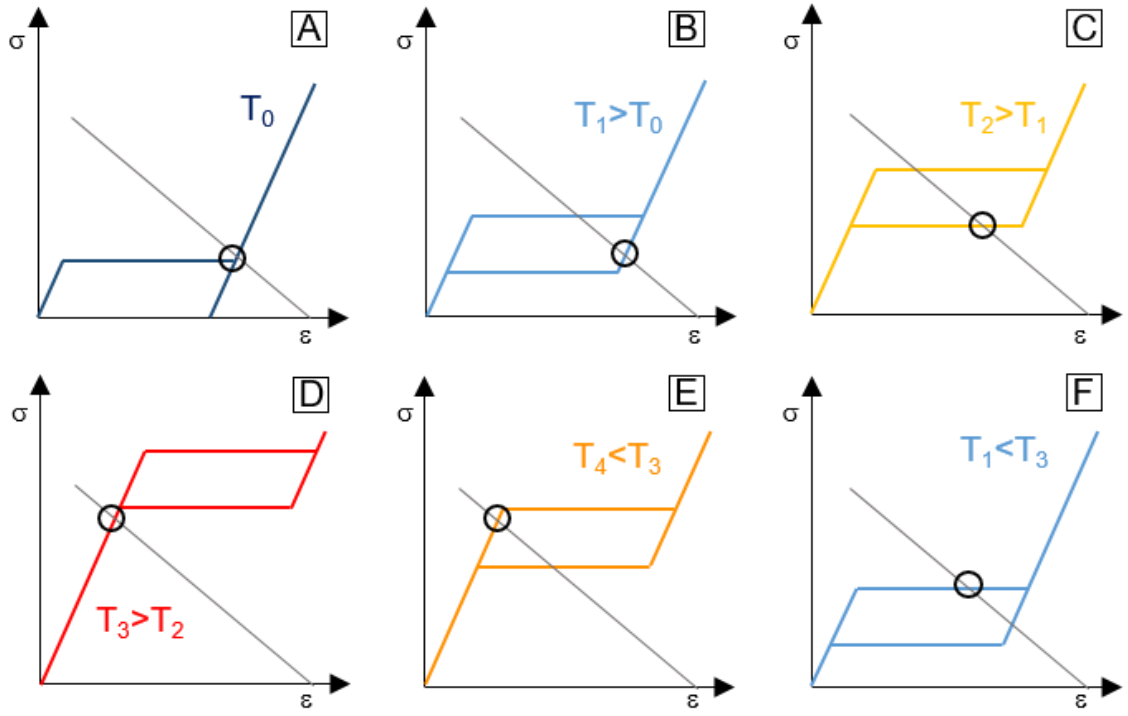

Figure 1.7: Qualitative stress-strain diagram representing the equilibrium behavior between single crystal SMA hysteresis and a linear spring characteristic during thermal loading and unloading cycle.

1.3.2 SMA actuators: shape memory alloy load

In this Section, the actuation topology, based on two SMA wires arranged in agonistic configuration (Figure 1.8), will be discussed. In this case, each of the two wires acts as a load for the other. In order to achieve motion, the wires do not have to be activated simultaneously. In this way, while one wire is activated (it is in austenitic phase), the other one is stretched and thus it is in detwinned martensitic phase. Referring to the system depicted in Figure 1.8, driving the two wires with alternate pulses, make the point P move horizontally, according to the SMA wires motion.

From the mechanical point of view, the working principle can be easily understood analyzing the diagrams in Figure 1.9. This picture represents a typical loading/unloading cycle in which the SMA wires are alternating activated. This cycle is represented by the single-crystal hysteresis of the wire at the left hand side of Figure 1.8 (here called SMA_1), superimposed with the single-crystal hysteresis of the wire at the right hand side of the same picture (called SMA_2). Since the two wires are in agonistic configuration, SMA_1, whom, for convention, has a negative displacement (Figure 1.8), has its hysteresis mirrored.

For each configuration, the equilibrium solution is detected using the graphical method and, in the Figure 1.9, highlighted by a black circle. In the first situation (Figure 1.9, (A)), the SMA_2 is at room temperature and lays in equilibrium with the SMA_1, which is already activated and in austenitic phase. The equilibrium point (the intersection between the two characteristics) is unique, and is located at the right-hand side branch of the hystereses. From this intersection, we can note that the SMA_2 is in detwinned martensitic phase. Starting from this configuration, the SMA_2 is activated via electric current. Its temperature and transformation stress start to rise. Graphically, this effect is represented by a hysteresis, which starts to move upward in the stress-strain diagram. On the same time, the SMA_1 is deactivated. In this case, its transformation stress will start to decrease and thus the hysteresis will move downwards.

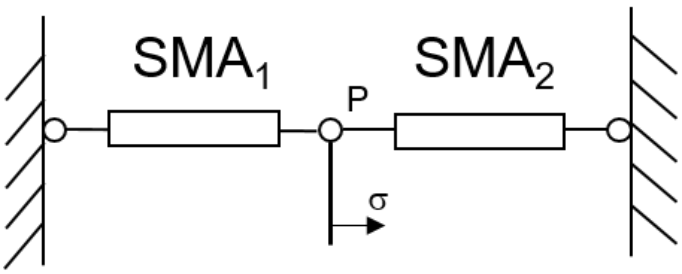

Figure 1.8: Two SMA wires in antagonistic configuration

In Figure 1.9 (B), the SMA_2 temperature is slightly increased, while the one of the SMA_1 is decreased. Nevertheless, the equilibrium point has not changed its absolute position in the stress-strain diagram. In this configuration, the two hystereses intersect in two "possible" equilibrium points. Without any knowledge about the history of the full process, it would be impossible to understand which of the two points is the correct one. In this case, knowing that the temperature of SMA_2 is increasing and the one of SMA_1 is decreasing, we can easily assert that the point laying on the hysteresis right hand side is the correct equilibrium point. If the SMA_2 temperature further increases and the one of SMA_1 decreases, the equilibrium point will keep moving along the SMA_2 hysteresis bottom branch and SMA_1 hysteresis upper branch. From Figure 1.9, (C), we notice that even if the temperatures of both wires (and thus their hystereses) are variated, the position of their intersection point is unchanged.

When the temperature T_3 and then T_4 are reached (Figure 1.9, (D-E)), the point has gained the left hand side of the hystereses, which means that the SMA_1 wire is fully in martensitic configuration, while the SMA_2 is still undergoing the phase transformation (the equilibrium point lays on the bottom branch of its hysteresis and not on the elastic branch). In Figure 1.9, (F), the two wires are fully transformed and a new equilibrium position is reached. The difference between the initial equilibrium point value (Figure 1.9, (A)) and its final value (Figure 1.9, (F)) represents the achievable system stroke, which can be easily relate to the maximum achievable motion for the system in Figure 1.8.

During the reverse process (SMA_2 cooled down and SMA_1 activated), the equilibrium point will move along the SMA_2 upper hysteresis branch and SMA_1 bottom hysteresis plateau.

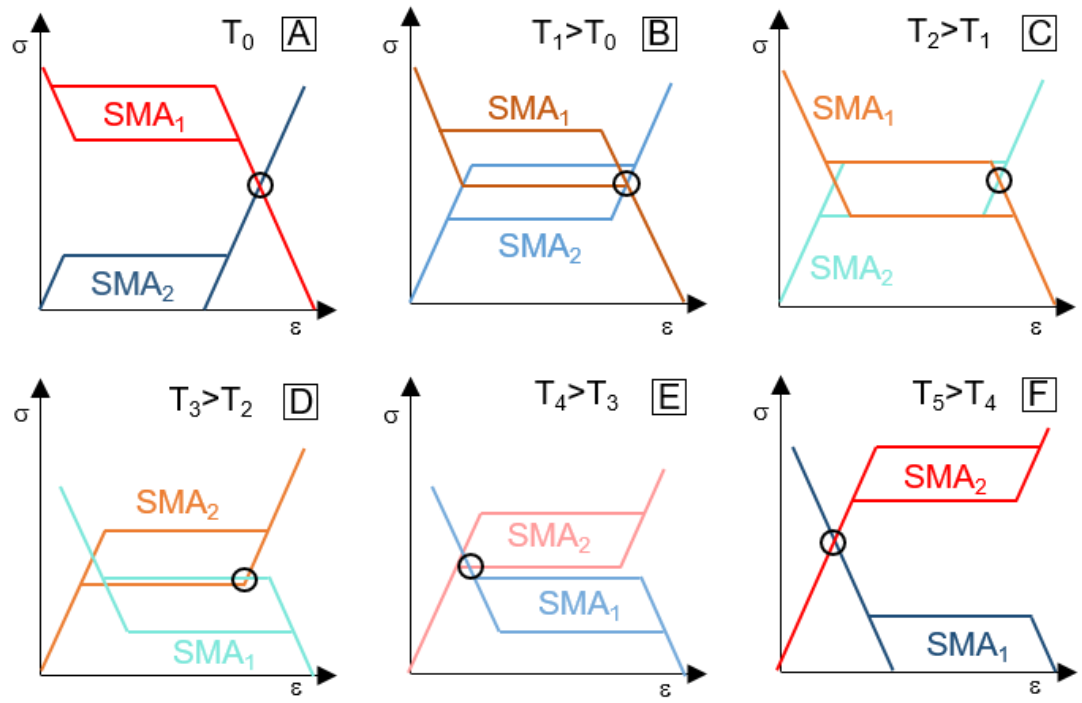

Figure 1.9: Qualitative stress-strain diagram representing the equilibrium behavior between two single crystal SMA wires in agonistic configuration during thermal loading and unloading cycle.

1.3.3 SMA actuators: self-sensing

From an electrical point of view, SMAs behave mostly as resistors. For self–sensing applications, it is of fundamental importance to characterize the relationship between SMA electrical resistance and state of the material. Once this relationship is available, it is possible to couple it with the actuator model in (1.15) to simulate the complete thermo–electro–mechanical response of the wire, or eventually use it for sensorless applications. In this way, it is possible to estimate a SMA based system displacement by measuring the SMA resistance behavior corresponding to a desired input power.

In Figure 1.10, the SMA wire stress-strain behavior to different power stimuli is compared to its change in resistance. For low values of power input (range 0-0.3 W), the change in resistance in the wire is really small, since the temperature induced in the wire is lower than its A_s temperature. In this case, the phase transformation is not enabled. A similar variation in resistance is observable for high input power values (range 0.6-1 W). In this case, the wire is already in austenite phase; therefore, the change in resistance is due to its pseudo-elastic behavior. Even if for these ranges the change is small, we can observe that the resistance has different absolute values, allowing us to understand in which status the

wire is. For intermediate input power values (range 0.4-0.55 W), the phase transformation occurs depending on the material induced strain. In this case, the resistance varies along its entire range as show in Figure 1.10, left hand side. For each value of input power, the SMA resistance behavior is mostly linear [21], which make the self-sensing approach a very appealing feature for SMA based actuators.

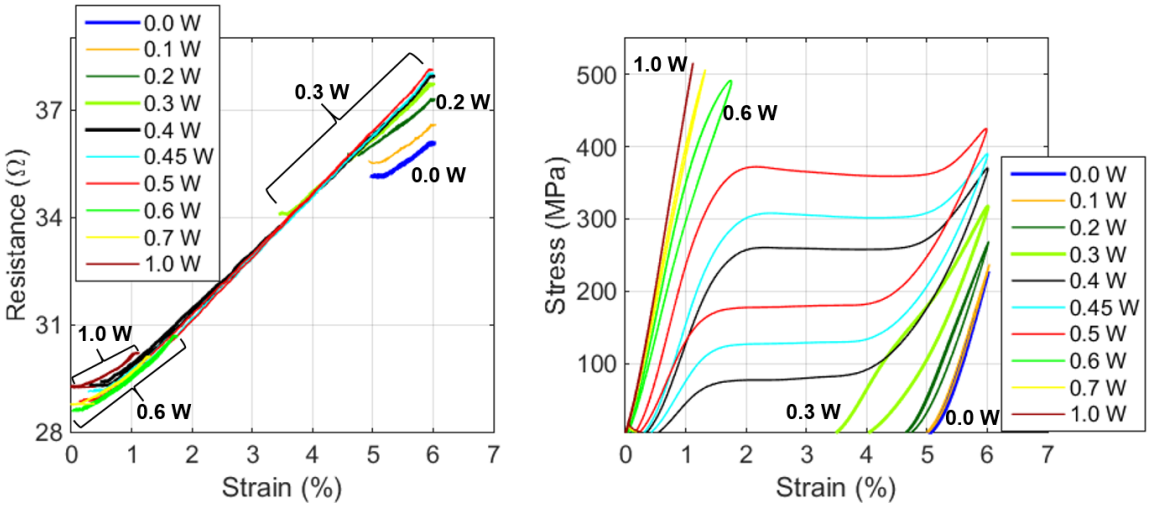

Figure 1.10: Behavior of a 76 μm diameter SMA wire actuated with different power input value. (Left hand side) Resistance- strain diagram. (Right hand side) Stress strain diagram.

For modelling purposes, the electrical resistance of a SMA wire can be computed as follows [65]:

$$R(\varepsilon, x_+, T) = \rho_e(x_+, T)\frac{l_0(1+\varepsilon)}{\pi r_0^2(1-\nu\varepsilon)^2}, \tag{1.16}$$

where R is the SMA resistance, ρ_e is the electrical resistivity of the material, and ν is the Poisson's ratio. The resistance depends on the strain due to the change in material length and radius. At the same time, the resistance also depends on material phase and temperature via the resistivity ρ_e. Quantity ρ_e is assumed to depend only on phases [67]. This assumption is true provided that a treatment process is realized during material manufacturing [71], [72]. Under these assumptions, the resistivity can be computed as

$$\rho_e(x_+, T) = \rho_{e+}(T)x_+ + \rho_{eA}(T)x_A. \tag{1.17}$$

Resistivity for each phase is assumed to increase linearly with temperature, according to the following laws

$$\rho_{e+}(T) = \rho_{e+}(T_0)(1+\alpha_+(T-T_0)), \tag{1.18}$$

$$\rho_{eA}(T) = \rho_{eA}(T_0)(1+\alpha_A(T-T_0)). \tag{1.19}$$

Quantities $\rho_{e+}(T_0)$, $\rho_{eA}(T_0)$, α_+, α_A represent constant material parameters.

2 SMA Hand prototype: 1st generation

The hand is the most articulated part of the human body, and also one of the organs deeply used in our daily life. During the last decades, researcher have tried to design devices (pneumatically actuated or electric motors driven) able to replicate the hand appearance and functionality [1]–[3]. Even if these devices are capable of great versatility and high forces, they faced high rejection rates, mainly due to the their heavy weight, noisy operation and also to the unnatural feel of the fingers [12]. To overcome limitations of conventional actuation technologies, new materials such as Shape Memory Alloys (SMAs) have been considered as potential candidate actuators for these kinds of devices. As introduced in the previous Chapter, SMAs, commonly based on Ni-Ti alloys, are materials which undergo a phase transformation when exposed to heat [73]. The phase transformation occurs with a significant change in geometry (up to 4-8%), which can be used to achieve actuation. Due to their small size and high flexibility, SMAs can be easily integrated in complex structures and used as actuators, without requiring any kind of mechanism for the motion transmission. The many features listed above have inspired many researcher to develop several hand prosthesis based on this technology [26], [74]. Despite the advantages introduced by SMA transducers, the prosthesis developed so far are still not able to completely fulfil the basic requirements for real life applications [11]. Moreover, the limited SMA stroke, together with the material hysteresis, significantly increase the difficulties in the design, model and control of devices based on this technology.

In this Chapter, a first novel concept for an artificial hand based on Shape Memory Alloys (SMA) transducers is described. The first part illustrates the hand fingers structure and its fabrication procedure. Then, to evaluate the hand fingers features and performance, experimental evaluations are realized and discussed. At the end of the Chapter, the hand assemblage is described and its performances while grasping different size and shape objects depicted.

2.1 Hand design requirements

In order to realize a device suitable to be used as a hand prosthesis without encountering rejections from the users, the following requirements has to be fulfilled [11], [13]:

- the overall weight has to be not higher than 500 gr;
- the dimensions have to respect the average human values;
- total force in the range of 50 N;

- finger phalanx motion speed in the range of 0.5 ms (for playing piano 0.1 ms);
- from 5 to 3 fingers (to grip the most used objects of daily life);
- the device has to be able to successfully perform daily life operations

Although preliminary results have shown high potential of SMA technology for prosthetic devices, none of the SMA prosthetic hands presented in literature so far can be considered mature enough to support amputees in typical real-life operations. This is mainly due to the limited performance of the current prototypes, mainly in term of force and versatility [13, 27]. In order to give a valuable contribution to this research field, a novel concept for a prosthetic hand is developed, according to the following design decisions:

- structure with average human hand dimensions [75];
- finger prototype hollow structure;
- SMA wires guided inside the structure, along the fingers.

These design guidelines ensure a lightweight, compact and non-complex structure. Guiding the SMA wires along the fingers guarantees a reduction of the prototype dimensions and avoids the use of motion transmission systems. According to this design strategy, one of the most important aspect to be initially investigated is the position of the wire inside the structure. In order to optimize it, a kinematic model is developed considering only the first two upper phalanxes of the finger. The model description and results are presented in the following Section.

2.2 SMA Finger Kinematic Model

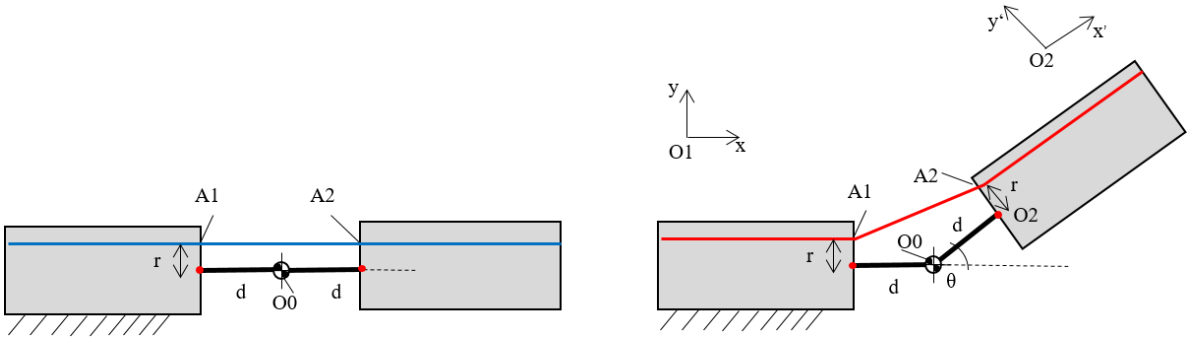

Figure 2.1: Sketch of tip and middle finger phalanxes with geometrical parameters. The line inside the structure evidences the SMA wire. (Left hand side) The finger in the initial position, with the SMA wire not actuated. (Right hand sire) Finger in the actuated configuration.

Let us consider a two finger phalanxes, having one fixed (middle phalanx) and the other free to rotate (tip phalanx), as shown in Figure 2.1. The SMA wire is located inside the

structure and fixed to the structure at both end sides. By design, it is free to slide along the phalanxes, in order to induce a rotation if actuated (Figure 2.1, right hand side).

By means of kinematic considerations, it is possible to predict the rotation angle of the phalanx in relation to the SMA induced strain. The rotation angle depends on joint geometry and on attachment point of the wire. In general, attaching or guiding the wire closer to the rotation axis of the phalanxes allows to achieve a larger joint rotation induced by a comparatively small contraction of the wires. On the other hand, this design solution decreases the torque resulting from the same force in the muscle wire necessary. The goal is to define an optimal location for the attachment point in such a way to achieve a full 90-degrees rotation with the available SMA wire strain and, at the same time, maximize the generated moment. Since SMA wires are intrinsically able to generate stresses up to 300 MPa in the actuated configuration while still maintaining good fatigue behavior, and since, at this early stage, the aim is to show the concept functionality, only kinematic relations will be investigated for design purpose.

In order to develop the kinematic model, we define the following quantities in Figure 2.1: attachment points of the wires, denoted as *A2* and *A1;* joint center *O0*; attachment point from the joint to the center of tip and middle phalanxes, denoted as *O2* and *O1* respectively; distance *r* between wire and joint attachment points on the same phalanx, where $r = \overline{A1O1} = \overline{A2O2}$; length of the segment that links the joint attachment points to the center of rotation *d*, where $d = \overline{O0O1} = \overline{O0O2}$; rotation angle θ. Let us also introduce the current reference system, attached to the top phalanx, having origin in *O2* with standard orientation and *x* axis directed according to $O0O2$, and fixed reference system, attached to the middle phalanx, having origin in *O1* with standard orientation and *x* axis directed according to $O1O0$. When the wire is not actuated, the angle θ equals zero.

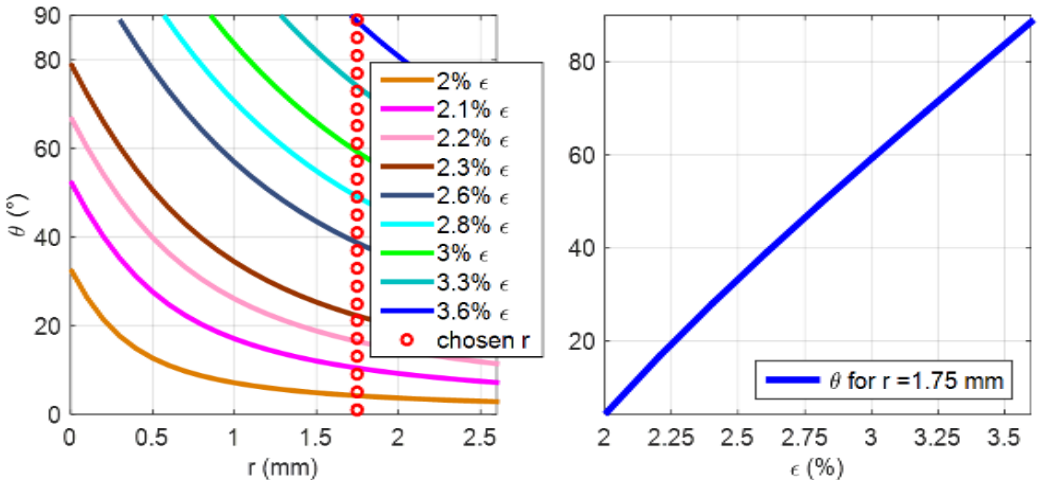

Figure 2.2: (Left hand side) Effect of the wire attachment point on the first phalanx bending angle induced by several SMA contraction rates. (Right hand side) Effect of the SMA possible induced contraction on the first phalanx bending angle.

Since the wire is constrained to slide along the holes inside the rigid phalanxes, a wire contraction is directly translated into a shortening of the segment $\overline{A1A2}$ (Figure 2.1). By using geometric relations, a kinematic model which relates θ to the actual contraction of the wire $\Delta L_{SMA} = \overline{A1A2}$ can be developed. We first define the coordinates of the following points:

$$A1^f : \begin{bmatrix} 0 \\ r \end{bmatrix}, \tag{2.1}$$

$$O2^f : \begin{bmatrix} d + d\cos\theta \\ d\sin\theta \end{bmatrix}, \tag{2.2}$$

$$A2^c : \begin{bmatrix} 0 \\ r \end{bmatrix}, \tag{2.3}$$

where superscripts *f* and *c* denote whether the coordinates are considered in the fixed or current frames, respectively. Then, it is possible to use coordinate transformations to express point *A2* in the fixed reference system, by using the following rotation matrix from current to reference system [76]

$$T_c^f = \begin{bmatrix} \cos\theta & -\sin\theta \\ \sin\theta & \cos\theta \end{bmatrix}. \tag{2.4}$$

Coordinates of point *A2* in the fixed system can then be expressed as

$$A2^f = O2^f + T_c^f A2^c. \tag{2.5}$$

By replacing (2.2)-(2.4) into (2.5), we obtain

$$A2^f = \begin{bmatrix} d + d\cos\theta - r\sin\theta \\ d\sin\theta + r\cos\theta \end{bmatrix}. \tag{2.6}$$

It is then possible to express the desired change in length of the SMA wire as follows

$$\Delta L_{SMA} = 2d - \sqrt{\left(d + d\cos\theta - r\sin\theta\right)^2 + \left(d\sin\theta + r\cos\theta - r\right)^2}, \tag{2.7}$$

where *2d* appearing on the right-hand side of (2.7) represents the length of segment $\overline{A1A2}$ in case $\theta = 0$. Quantity ΔL_{SMA} represents the portion of SMA wire which contracts during actuation. It is also possible to express this quantity as a function of the lengths of unactuated and actuated SMA wire, denoted as $L_{SMA,u}$ and $L_{SMA,a}$, respectively, as follows [77]

$$\Delta L_{SMA} = L_{SMA,u} - L_{SMA,a} . \tag{2.8}$$

By introducing the actuation strain ε as follows

$$\varepsilon = \frac{L_{SMA,u} - L_{SMA,a}}{L_{SMA,u}}, \tag{2.9}$$

it is possible to rewrite (2.8) as

$$\Delta L_{SMA} = \varepsilon L_{SMA,u} . \tag{2.10}$$

Finally, by equating (2.7) and (2.10) it is possible to achieve a mathematical relationship between actuation strain ε, bending angle θ, and initial geometry of the wire. The solution of this equation, for different SMA strains, is shown in Figure 2.2, left hand side. As stated before, the smaller the distance *r* between the wire attachment point and the joint rotational axis, the bigger the rotation induced in the phalanx. NiTi wires are generally capable of ~4.5% actuation strains, but in order to ensure a longer working life, we have chosen to exploit the SMA strain only up to 3.5% [78]. To protect the actuator structure (in particular the phalanx joints) from the high temperature of the actuated wire (around 90°C), to make the structure more robust, and to guarantee the maximum possible phalanx bending, the attachment point is chosen as *r* = 1.75 mm (red dots in Figure 2.2, upper part). Since in Figure 2.2 (right hand side), the maximum bending angle in the chosen strain range is 90 deg, the current wire configuration will only induces the bending of one phalanx, leaving the other finger phalanxes in the starting position.

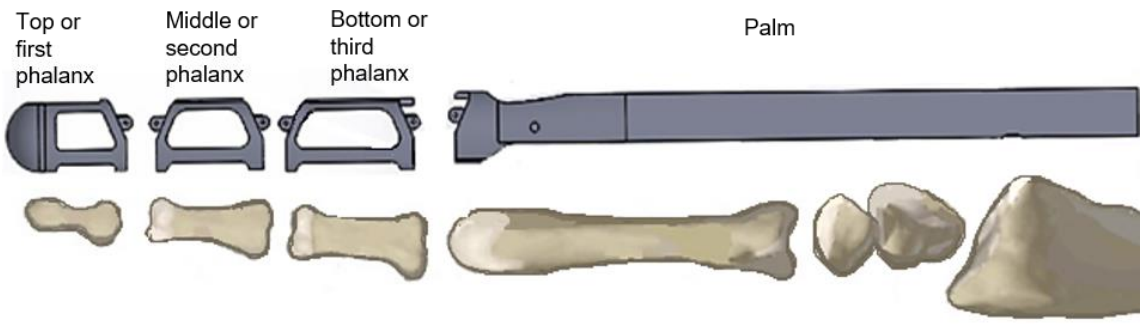

Figure 2.3: Analogy between the designed finger actuator and the human finger structure

2.3 SMA Finger Design

The design of the finger actuator is realized considering the result of the kinematic model exposed in Section 2.2 and the design requirements highlighted in Section 2.1 and, on the same time, taking inspiration from real human fingers.

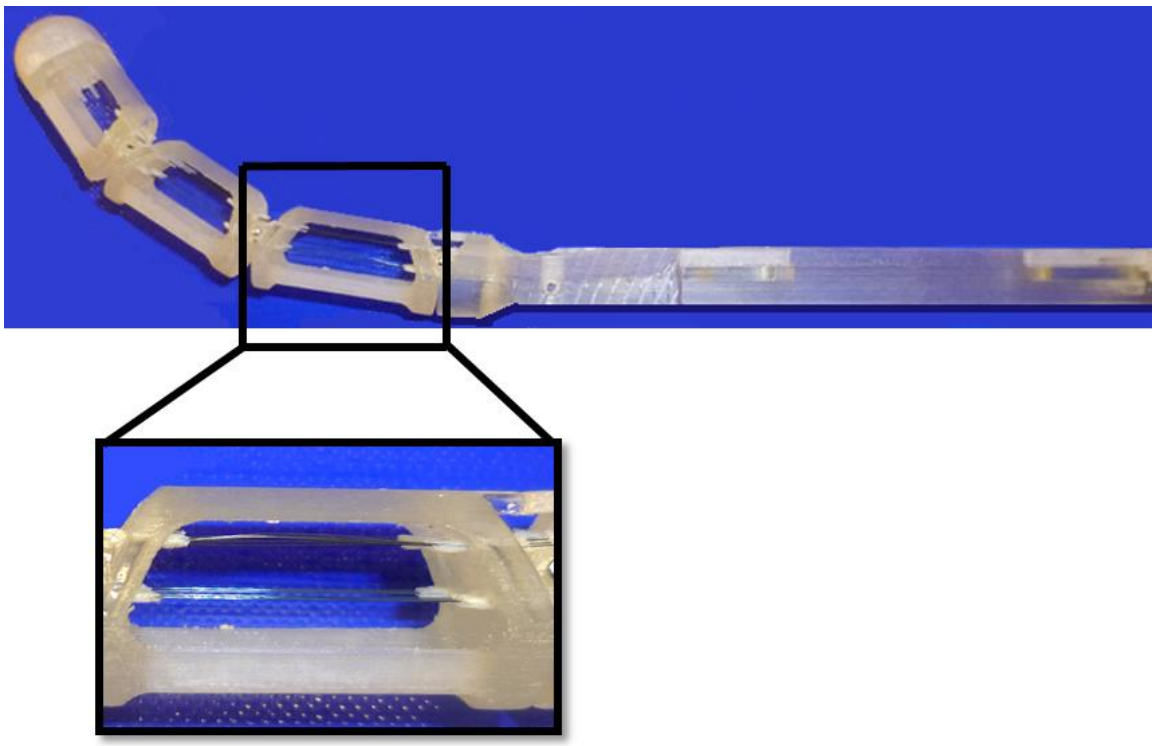

Figure 2.4: Detail of SMA finger actuator. Wires are inserted through tube guide and enveloped along the actuator.

A CAD model of the finger is shown in Figure 2.3. It is divided into four parts, each one dimensioned according to the average size of human finger's phalanx, metacarpus, and carpus [75]. For functional purposes, a small portion of the wrist is also considered as a part of the overall concept. To interconnect the phalanxes, the distal interphalangeal and the proximal interphalangeal joints are designed as 1-DOF rotational joints. The phalanxes have a hollow structure, in which the exterior part is made of different arc-shaped rounded holes (Figure 2.3), while the frontal part consists of homogeneous material. This design choice is introduced to ensure structural lightness and endurance during the actuation, avoiding undesired deformation of the structure during the bending of the finger. In the human body, the motion of the fingers is a result of the contraction of muscle fibers located in the arm. These muscles are linked to the finger phalanxes via robust tendons settled around the bones and anchored to them [75]. Similarly, to biological muscles, also SMA wires produce a contraction when actuated via an electric current. In order to ensure compactness and avoid contact between the wires and the grasping target, the wires are routed inside the finger structure, along each phalanx. For this purpose, internal holes with

a diameter of 0.5 mm are created. To allow bending motion of the phalanxes, an antagonist-protagonist wires configuration is adopted. In this way, a faster actuation than the one performed with a simpler SMA-spring configuration can be achieved, ensuring an active and precise bending (carried out by protagonist wires) and stretching (by antagonist wires) movements, depending on which wire is activated [26]. This comes, of course, at the expense of power consumption and number of wires necessary for the overall system.
Each finger phalanx is designed in such a way that the available small strain of SMA wires (in the range of 3.5% for safe operations [78]) can generate enough bending moment around the joint. As deduced from the kinematic model exposed in Section 2.2, to protect the actuator structure from the high temperature of the actuated wire (around 90°C), to make the structure more robust, and to guarantee the maximum possible phalanx bending, the attachment point is chosen as r = 1.75 mm (red dots in Figure 2.2, upper part). Since in Figure 2.2 (right hand side), the maximum bending angle in the chosen strain range is 90 deg, the current wire configuration is able to induce the bending of one phalanx, leaving the other finger phalanxes in the starting position. To allow also the bending of the middle phalanx, a second SMA wire has to be attached all along the actuator and fixed to the middle phalanx tip. In this way, the contraction of this second wire will induce a rotation of the middle phalanx only, independently on the motion of the top phalanx.
To allow a faster finger actuation and to avoid large time delays due to the SMA cooling time, Flexinol® SMA wires (Dynalloy, Inc. Tusten, CA) with a diameter of 0.1 mm are used as metal muscles [78]. To increase the overall actuation force, each wire is winded (bundle) along the finger structure. In this case, the total force is given by the sum of the individual forces of each wire. The wire arrangement inside each finger will be explained in more details in the Section 2.4.

Coefficient	Value (mm)
Finger	
Finger top phalanx length	20.5
Finger middle phalanx length	25
Finger bottom phalanx length	30
Finger stand length	160
Finger width	16
Finger thickness	15
SMA wires	
First protagonist wire total length	800
Second protagonist wire total length	760
Antagonist wire total length	1800

Table 2.1: Finger dimensions.

2.4 SMA Finger Fabrication

The building process of the SMA finger system is structured in several steps, reported in the following:

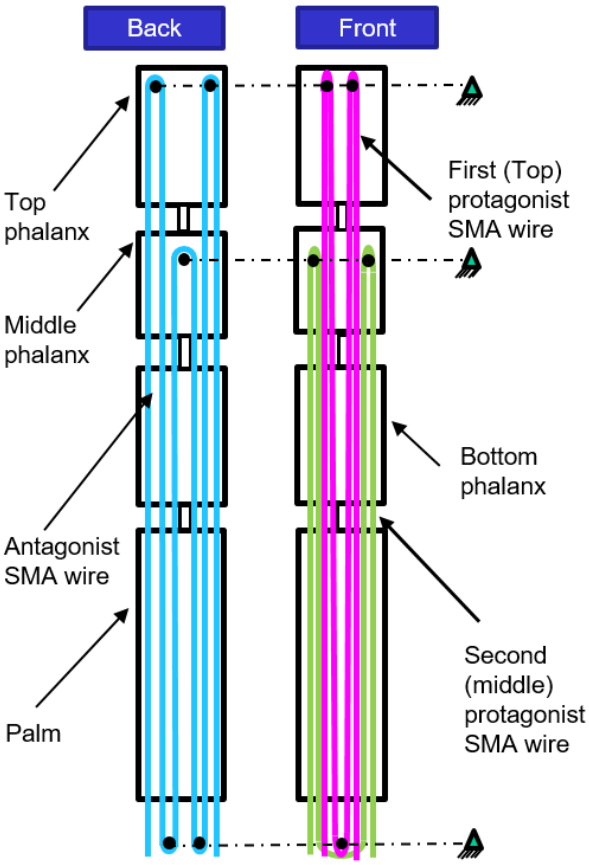

Figure 2.5: SMA actuated finger scheme that represents the SMA wires topology inside the structure and their wrapping point. On the right-hand side, the finger frontal part is shown and the two protagonist wires are represented in magenta and green. On the left-hand side, the finger back part is been schematized and the antagonist wire is represented in blue. The wires anchor points are also highlighted.

Step 1 : the SMA finger structure is designed in Solidworks, and then 3D printed with an Object Connex 500;

Step 2 : the printed parts are cleaned from impurities and then washed in isopropanol, to remove also the small residue. The joints are assembled using small metal pins. The result is a lightweight and strong skeleton;

Step 3 : small pieces of Teflon tubes are glued in the phalanxes, along the holes near the joints, as in Figure 2.4). This material is useful for its high temperature resistance and its small friction coefficient, which allows the SMA wires to smoothly slide within the tubes without thermally affect 3D printed material.

Step 4 : the protagonist wires (0.1 mm diameter Flexinol® SMA wires [78]) are integrated into the structure inside the tubes, as shown in Figure 2.4. During this process, each wire is wrapped along the phalanxes, around an anchor point. In particular, the first protagonist wire is wrapped twice around the top phalanx (magenta wire in Figure 2.5).

To induce an independent rotation of the second phalanx, also the second protagonist wire is wrapped twice along the finger palm up to the middle phalanx, excluding the top one (green wire in Figure 2.5). In this way, a bundle of eight wires mechanically in parallel is created. The use of bundle of SMA wires enables higher force in each finger phalanx.

Step 5 : the antagonist wire is wrapped three times along the phalanxes (blue wire in Figure 2.5) around the anchor points, creating in this way a bundle of six wires mechanically in parallel. To ensure a complete wire stretching for both phalanxes,

one of the loops is performed around the middle phalanx, excluding then the top one (see Figure 2.5).

In this case, only one antagonist wire is used to favor the rotation motion and to provide more gripping force.

Step 6 : wires are powered, one at each time, to let them fully transform in austenite phase. Subsequently, they are manually pre-strained in order to favor the detwinned martensite phase. This procedure ensures that each wire is in the same state during mounting.

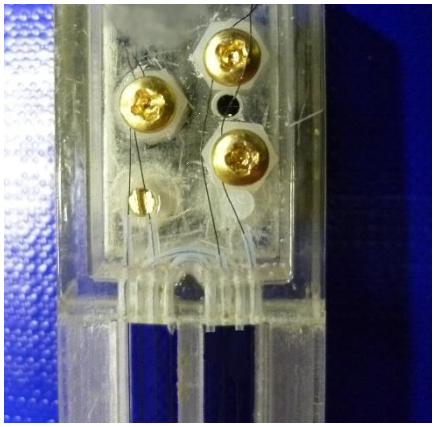

Figure 2.6: SMA wires mechanical connections in the finger prototype

Step 7 : Once pre-strained, the wires are clamped at the finger palm lower end. Due to the small wire diameter, conventional clamping mechanism can not be used. Therefore, each wire end is constrained by a screw and its corresponding nut (see Figure 2.6). In order to decouple mechanical and electrical connections, each nut is bonded, through a coil cable, to an electronic board, linked to a power source. In this way, any load acting on the SMA wires will not affect the electrical connections and vice versa.

The proposed wire arrangement gives full control over each finger phalanx position. All the wire lengths are included in Table 2.1. Since sufficient grasping capabilities can be ensured driving only the upper two finger phalanxes (tip and middle), the bottom phalanx is designed to be fixed. The entire prototype is shown in Figure 2.4 and has a weight of 25 gr, value below the real human finger weight [75].

2.5 SMA Finger Performance Evaluations

After the realization of the first SMA finger concept, several experiments are realized in order to evaluate the prototype performances. Figure 2.7 demonstrates the maximum achievable rotation angles for each joint. The motion starts with the finger completely stretched (Figure 2.7, (A)), with the antagonist SMA wires actuated. As soon as the antagonist wire are deactivated and the protagonist wire powered, the motion of the middle phalanx is enabled (Figure 2.7, (B)). When the middle phalanx reaches the face of the bottom phalanx, any further motion of the middle phalanx is prevented and, thus, the rotation of the tip phalanx is enabled (Figure 2.7, (C)). Due to design constrains, it is not possible in free space (without any external mechanical constrain) to induce the motion of the tip phalanx before generated the motion of the middle one.

In the following, displacement, force and self-sensing features are systematically evaluated by means of several experiments in order to demonstrate the prototype performances.

2.5.1 Self-sensing and displacement measurement

A Pulse Width Modulated (PWM) voltage controller is used to prescribe a command power to each set of wires. Power control is preferable to current/voltage control, because the power affects proportionally the equation governing SMA temperature evolution, while current/voltage enter in the same equation in a nonlinear way [64].

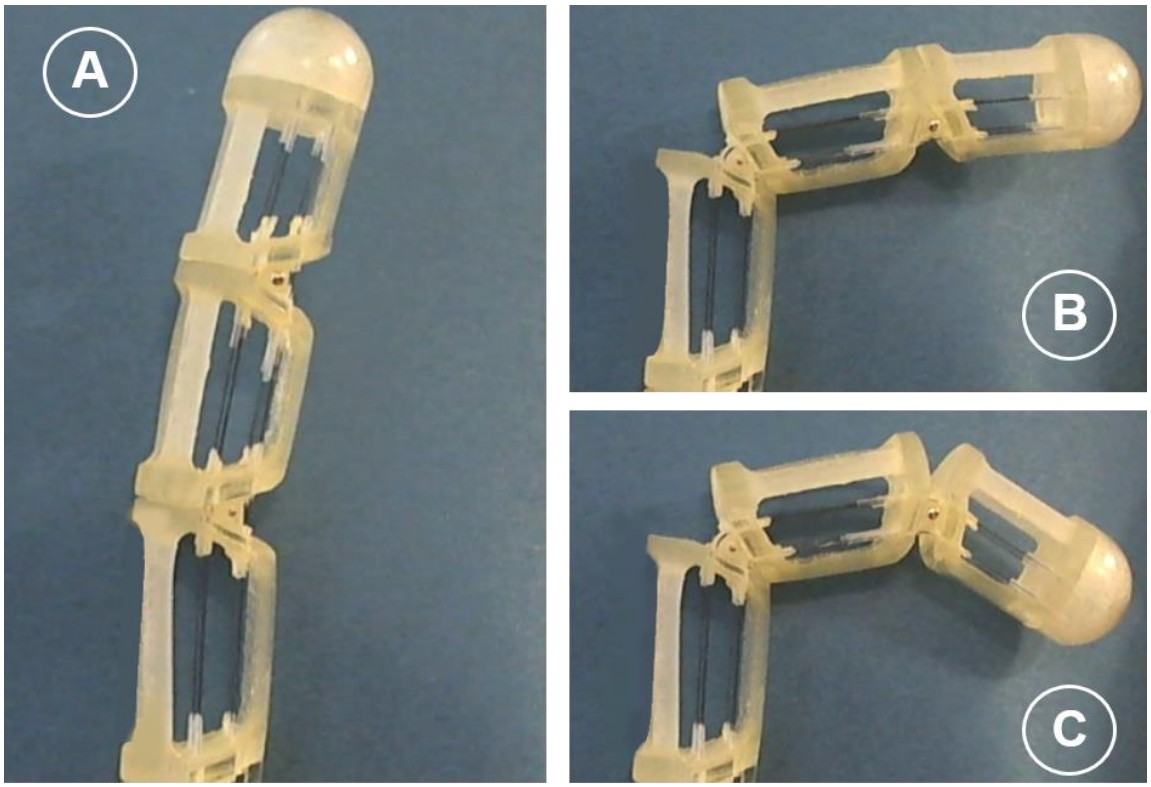

Figure 2.7: SMA Finger prototype maximum achievable rotation for each joint. (A) Fully stretched configuration. (B) Middle phalanx fully rotated. (C) Maximum rotation for top phalanx.

Since the temperature of the wire directly determines its actuation, power control turns out to be preferable in actuation applications.

We also remark that, when the wire is contracted due to heating, it undergoes a change in electrical resistance. If a constant power is achieved by means of a constant voltage, the change in resistance will induce a change in current as well, making the resulting power not constant. In this work, effective power regulation is obtained by using the method discussed in [79]. The approach is based on calculating the actual voltage command by dividing the desired power by the measured current. This allows for an automatic and robust compensation of resistance changes. We point out that the change in resistance occurring when actuating SMA wires can be also exploited for self-sensing [65]. In particular, it is possible to correlate the changes in resistance to changes in the wire length, and therefore in angular position θ. By measuring the SMA electrical resistance during actuation, it is then possible to reconstruct the mechanical rotation of the phalanxes without using

additional position sensors [79]. In the following, some experiments are conducted to investigate the relationships between input power, wires resistance, and displacement change. The power controller is built with a National Instruments (National Instruments Corporation, Austen, TX) cRIO-9074 real-time data acquisition system programmed with LabVIEW 2012. The voltage is applied to the SMA wires via a NI-9472 module that works as a digital switch, up to 30 V, at a switch time of 100 μs. A NI-9229 module is used to measure the voltage and an NI-9227 is used to measure the current. A 28 constant DC voltage source is used to supply the NI-9472.

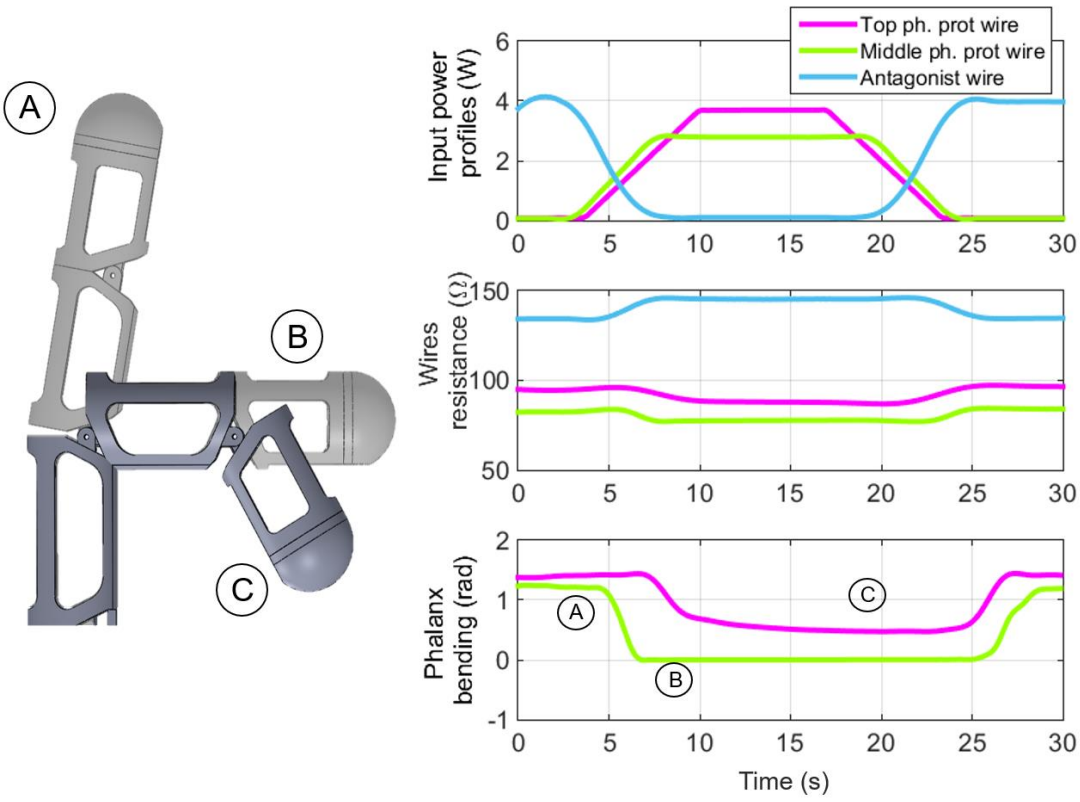

Figure 2.8: Power input profiles, Resistance and Displacement vs. Time for the three sets of SMA wires within one finger. Each curve refers to the wire having the same color in Figure 2.5.

During power control operation, an initial current and voltage measure is acquired while the switch of each wire is activated for 500 μs. This enables an initial calculation of nominal resistances and maximum powers for each wire. The FPGA program then compares the desired power with the maximum power calculated, and produces a PWM duty cycle which operates the NI-9472 switches, thus providing the desired power to each wire. The PWM is programmed with a fundamental frequency of 100 Hz. For each cycle, the voltage and current are measured during the on time of the PWM, and the new resistance and maximum power are calculated for the subsequent cycle. During testing, a host desktop computer running LabVIEW is used to send a desired power profile to each wire, and records voltage, current, resistance, and power data. LabVIEW is also interfaced with a Logitech web camera and synchronized with the NI measurement system. In each cycle a video frame of

the finger motion is acquired. The full video is then post processed via MATLAB, using built-in functions of the Computer Vision System Toolbox. Figure 2.8 shows the behavior of the three SMA wires during actuation. In this picture (upper part), a specific power profile is prescribed to the SMA wires. The maximum power depends on the wire length, and higher powers are applied to longer wires. To generate a full contraction-extension cycle of motion, the experiment starts with the antagonist wire completely actuated. The protagonist wires, then, are actuated according to the prescribed power profile. The theoretical results obtained in the Section 2.2 are confirmed by the middle phalanx angular displacement (Figure 2.8, lower part, green line). The top phalanx shows less motion than the one expected from the kinematic model.

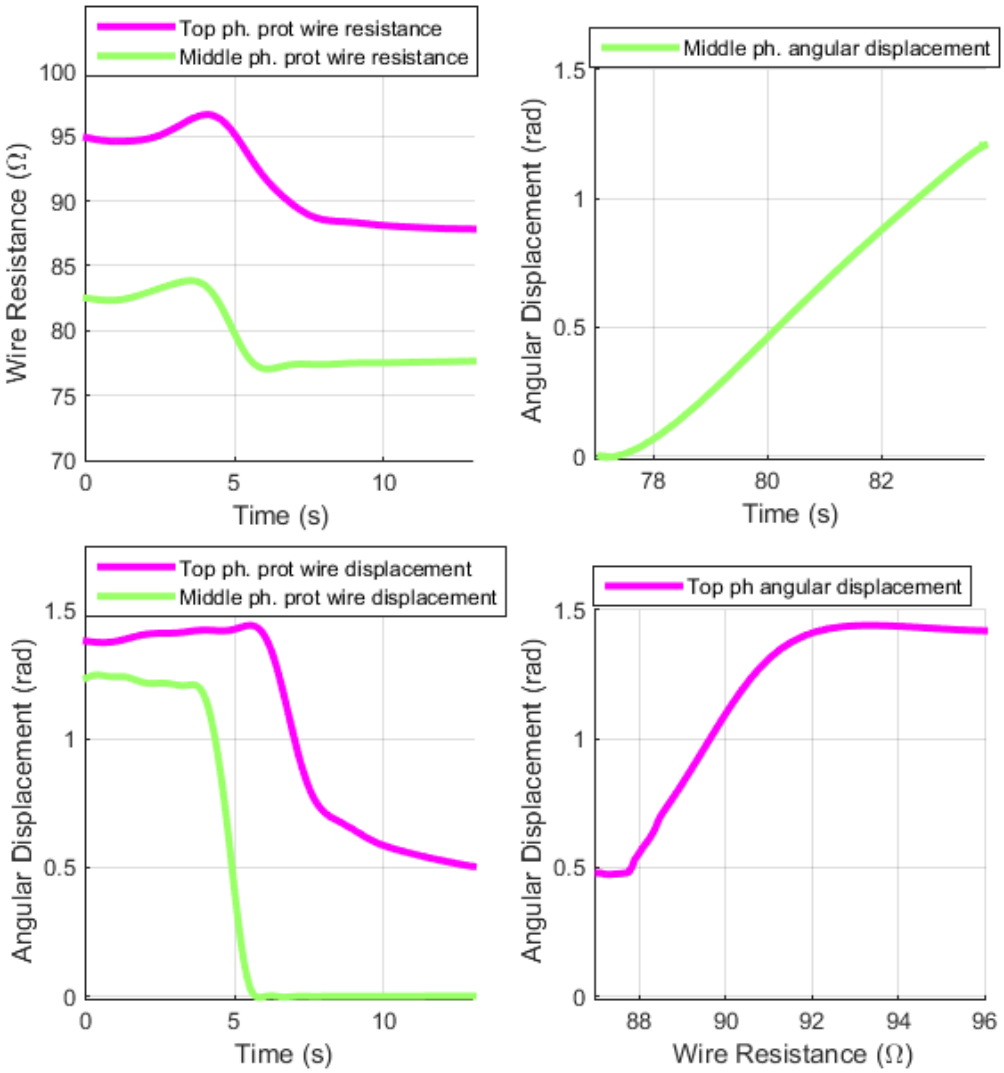

Figure 2.9: Finger behavior. (Left hand side) Zoom of Figure 2.8. (Right hand side**)** Displacement vs. Resistance for the middle (top part) and for the tip (bottom part) protagonist SMA wire. Each curve refers to the wire having the same color in Figure 2.5.

This mismatching may be due to friction induced by manufacturing imperfections, i.e., the Teflon tube length excess or glue deposit. Even if the protagonist wires are activated at the

same time, the motion is induced first at the middle phalanx joint and then at the tip. This happens because, according with Figure 2.5, both SMA protagonist wires across the middle joint but only few wires across the fist finger joint. For this reason, the induced moment at the middle joint is bigger than the one at the tip joint and, therefore, the middle phalanx joint moves first. Only when the middle joint is fully rotated, the tip joint starts to move, as visible in Figure 2.9 (left hand side, bottom part).

The change in resistance of the wires, shown in Figure 2.8 (center part), follows the motion of the extending finger, which can be also observed in Figure 2.8 (lower part). Even if the SMA wires are actuated at the same time, the change in resistance in one wire is independent of the changes in resistance in the other wires. From Figure 2.9 (left hand side), a perfect correspondence between the changing in resistance of the middle SMA wire (green line) and the middle phalanx behavior is highlighted. If vertical lines are drawn, a perfect correspondence between the start/end of the middle SMA wire changing in resistance and the start/end of the middle phalanx rotation (green lines) can be observed.

This correspondence is not visible for the top SMA wire (pink line). This happens because the resistance of this wire starts changing as soon as it is activated. Since the motion is induced at first at the middle phalanx joint, the top SMA wire contraction is suddenly translated into the rotation of the middle phalanx and not of the top one.

In Figure 2.9 (right hand side), the displacement-resistance relationship for the two protagonist SMA wires is depicted, highlighting its almost linear behavior in a well-defined range. By taking into account all of these aspects, in case of a single-wire system the angular position of the finger can be directly related to the resistance values of the wire. As discussed before, this feature is perfectly shown by the middle SMA wire (Figure 2.9 (right hand side, top part)). Let us focus our attention on Figure 2.9 (right hand side, bottom part), where the SMA resistance – finger rotation relationship is shown. As consequence of the wire arrangement inside the structure discussed before, we see a changing in resistance without inducing any motion at the top finger phalanx. As soon as the tip phalanx stars to move, the resistance-displacement characteristic becomes linear. In the last part, the characteristic becomes again flat, meaning that the top SMA wire is still contracting, but it is no more able to induce motion. This behavior could represent the presence of a hard stop (i.e. Teflon tubes) or of high frictions which prevent the phalanx rotation.

For the concept described in this research work, each SMA wire is coupled with the other wires in the same finger, making the exploitation of self-sensing for the determination of a unique finger spatial position not trivial. For this reason, more in-depth studies will be performed in future works in order to better understand this relationship.

2.5.2 Force measurements

In this Section, force measurements are shown for the first concept of the SMA finger. Since each phalanx is directly actuated by the same number of SMA wires, the

measurements are performed only from the middle phalanx. The experimental bench consists of a National Instruments (National Instruments Corporation Austen, TX) cRIO-9074 real- time data acquisition system programmed with LabVIEW 2012, connected with a NI 9237 and a NI 9472 modules. A load cell (Futek, LSB 200) is interfaced with the cRIO through the NI 9237 module. Using the NI 9472 module, the finger phalanxes are driven by an on/off voltage input signal ranging between 0-27 V and with a limited maximum current of 0.2 A (to avoid any wire damage), as suggested in [78]. The load cell is hold to a breadboard through a slide (THORLAB® modules) that allows motion in the 3 spatial directions. In this way, it is always possible to locate the load cell perpendicularly to the finger phalanxes, independently of the finger configuration. To ensure an accurate load cell positioning and to measure the finger angular displacement for every experiment, a Logitech webcam is added to the bench and interfaced with LabVIEW.

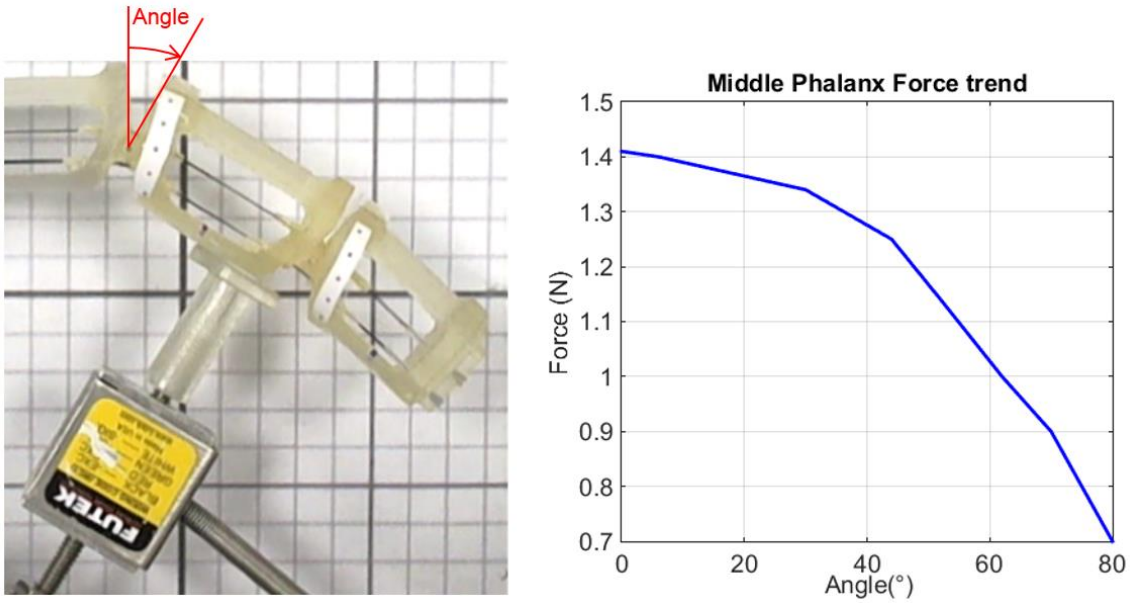

Figure 2.10: (Left-hand side) Force evaluation area and measured bending angle during force evaluation trend. (Right-hand side) Middle phalanx force trend.

As discussed in the previous Sections, the force of each finger is easily scalable depending on the number of SMA wires. Therefore, the purpose of this set of experiments is to obtain a first quantification of the force exhibited from the protagonist SMA wires. These measurements will then be used for future improvements of the design.

Since the force measured from the load cell is not uniform along the phalanx (it increases by measuring closer to the center of rotation), we choose the top of the middle phalanx as force evaluation point, as shown in Figure 2.10 (left hand side). Figure 2.11 (left hand side, bottom part) shows the maximum force measured by giving a 27 V step shaped voltage input (Figure 2.11 (left hand side, top part)), and starting with a fully straight finger. By relating the input signal to the force measurement, the settling times for the rising and falling force steps are about 1 s and 1.5 s, respectively. This difference in time is related to the number of SMA wires involved in the actuation (4 wires for the middle phalanx bending

and 2 wires for the stretching), and also to the different anchor point used for rounding the wires, as shown in Figure 2.5. These settling time values strongly depend on the input power used in these experiments, which is kept below the safety limits suggested by the manufacturer [78]. Better performances can be further obtained, e.g., by using short pulses of higher magnitude supply voltages in order to increase the wire response time [80], [81], or by means of closed loop algorithms. In Figure 2.11 (right hand side, top part), the force of the first protagonist SMA wire, always evaluated at the middle phalanx, is depicted. Even if the first protagonist SMA wire has the same number of windings of the second protagonist SMA wire, the force evaluated in this case is smaller. This because, in this case, the moment of the SMA wire at the tip has a bigger lever arm of the wires connected to the middle phalanx, and therefore, the correspondent measured force is smaller.

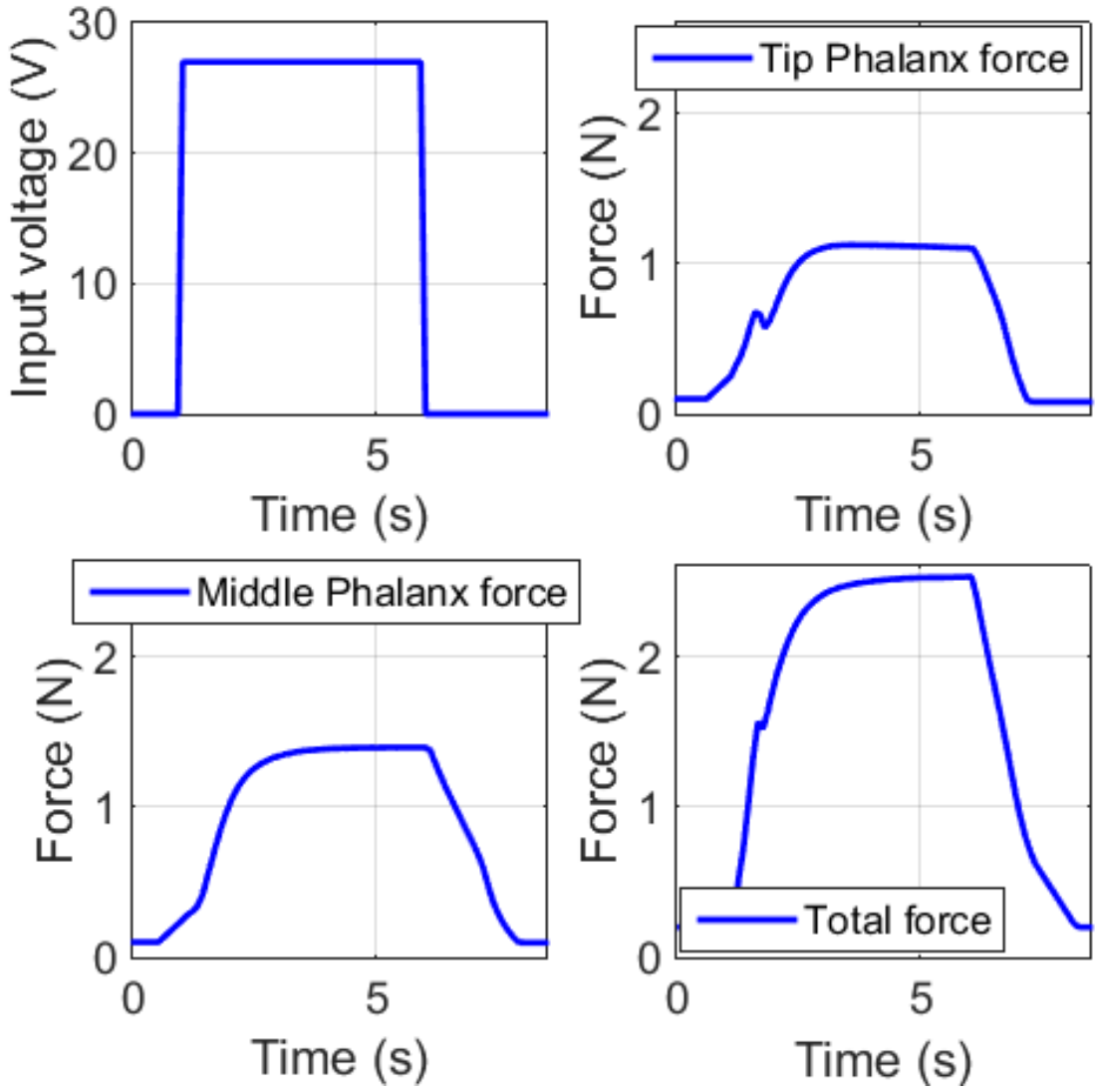

Figure 2.11 : Force measured at the middle point of the middle phalanx actuating (left hand side, bottom part) the second protagonist SMA wire, (right hand side, top part) the first protagonist SMA wire and (right hand side, bottom part) both SMA wires, for a predetermined input (left hand side, top part).

Observing the first protagonist SMA wires force characteristic in Figure 2.11 (right hand side, top part), a hump can be noticed in the rising path.
This behavior could be connected to a potential loss of force due to a slight rotation of the second phalanx joint during the experiment. Further evaluations need to be realized by means of mathematical models in order to completely understand this behavior. In Figure 2.11 (right hand side, bottom part), the force measured at the middle phalanx actuating both protagonist SMA wires is represented. We can observe that this force value is too small in comparison to the real human one.
Due to the structure and to the arrangement of the wires, the exerted finger force is not constant but depends on the finger configuration. For this reason, set of experiments focused on detecting the force trend are performed varying the finger bending angle (Figure 2.10, right-hand side) when only the second SMA wire is activated. Also in this case, the middle phalanx topper part (the area most distant form the center of rotation) is chosen for the force valuation. In this way, the minimum force trend is captured and showed in Figure 2.10. From this picture, it is possible to notice that the maximum force is measured when the angle equals zero, i.e., when the finger is fully extended. Moreover, the achievable force decreases nonlinearly with increasing bending angle. Maximum and minimum forces, corresponding to 0° and 80°, equal 1.4 N and 0.7 N, respectively. This force drop may be related to the friction between the SMA wires and the Teflon tubes edges.

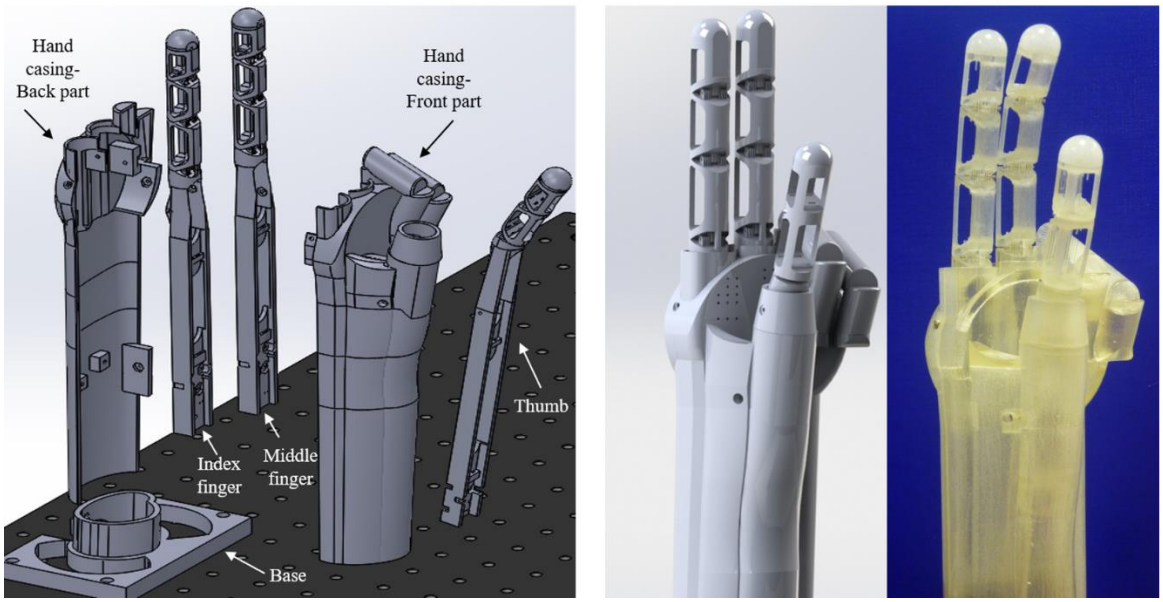

Figure 2.12: SMA actuated hand. (Left hand side). Exploded view of the SMA prosthetic gripper. (Right hand side). Progression of SMA prosthetic gripper from the 3D model to the full system.

2.6 SMA Hand concept

The human hand is a remarkably mobile and malleable mechanism. A wide variety of functionalities can be achieved by means of the unique structure of this organ, which consists of 23 DOF. It is possible to distinguish two groups of elements in the human hand skeleton, i.e., the fixed and the mobile ones [75]. Since the elements of the first group have only a structural function and since the prototype presented in this Chapter represents a first concept for a SMA actuated hand, they are not considered in the engineering design. To further simplify the design, since a successful grasping process is still possible by using the thumb, the index, and the middle fingers only, the ring finger and the little finger are designed to be not movable. This choice introduces a slight simplification in the structure while ensuring, at the same time, effective gripping functionality.

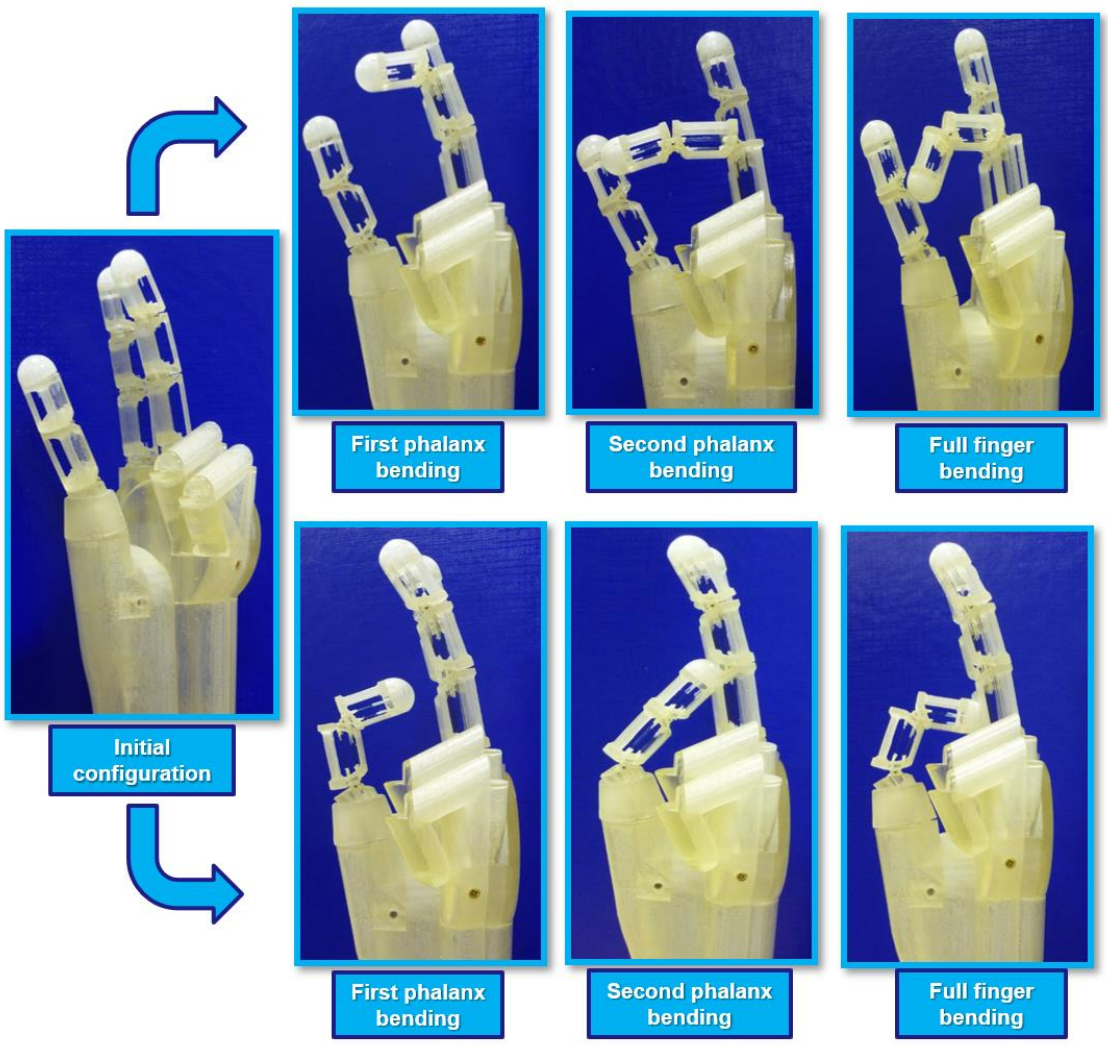

Figure 2.13: Possible hand configurations when the middle finger bending movement is induced (top) and when the thumb finger bending movement is performed (bottom). In both the situations, the initial position is represented, on the left, by the fingers in their fully stretched position (only antagonist SMA wires activated). In the next frames, going from

left to right, switching the actuation form the antagonist wires to the protagonist ones in the middle/thumb finger, the bending of the first, second and then both phalanxes are performed

2.6.1 SMA Hand design

The bio-inspired SMA gripper consists of three SMA fingers, a two-component external casing, and a supporting base (Figure 2.12, left hand side). The entire structure is modular, to enable quick replacement of parts if needed. The middle and the index fingers have the same structure, made of 3 phalanxes and a palm (that mimics the fixed bones in the human palm), while the thumb does not have the bottom phalanx, in agreement with human thumb [75]. Moreover, the palm of the thumb has a different shape in relation to the middle finger [75].

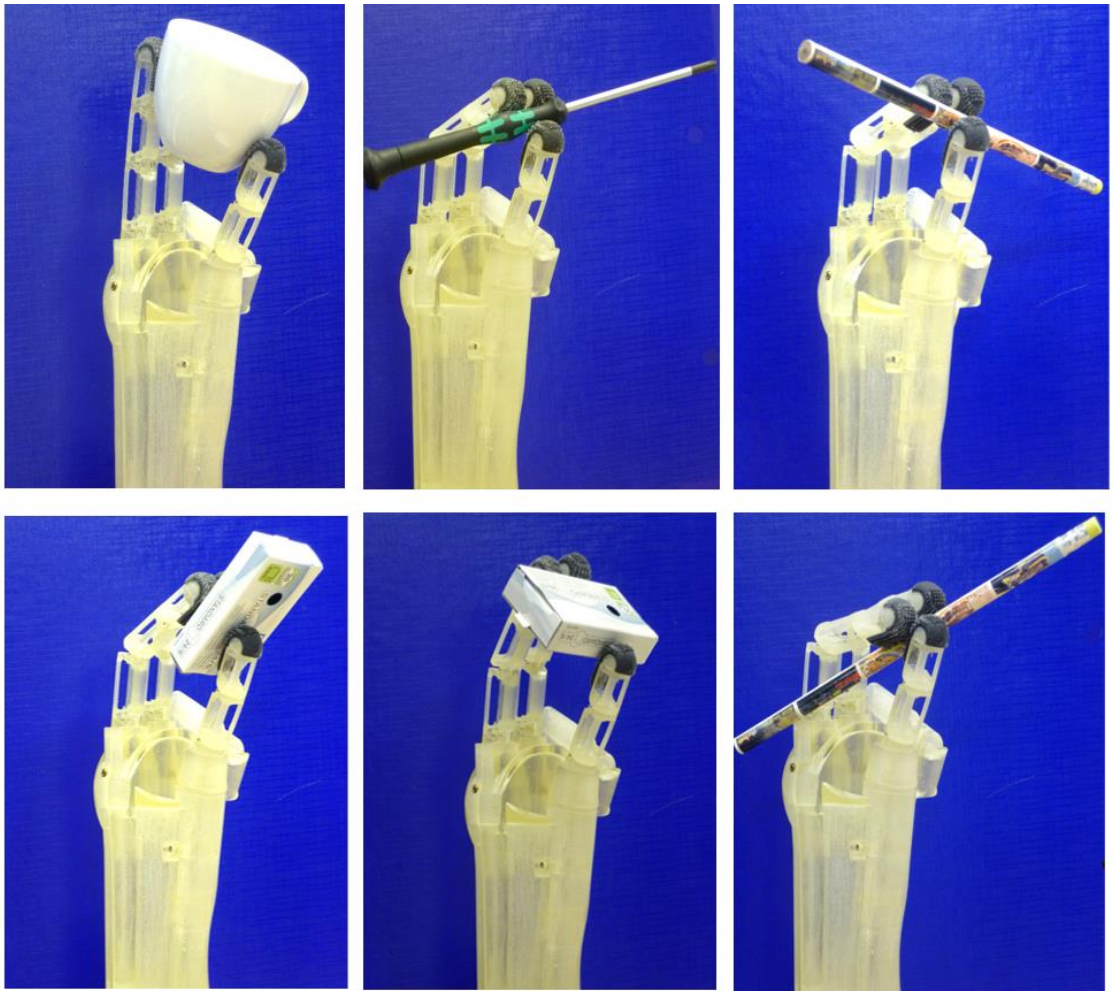

Figure 2.14: Some of the possible object which could be grasped by the gripper. In the upper frames, going from left to right, the grasping of a coffee cup, a screwdriver, a pencil is performed. In the bottom frames, going from left to right, the grasping of a rectangular box along the shorter side and bigger side and of a pencil in writing posture are demonstrated.

The joint between the thumb and the palm, indeed, is tilted by 45 deg with respect to the relaxed human thumb, in such a way the thumb is located in front of the other two fingers. This design solution allows for a better gripping of objects with bigger size. The system is designed in Solidworks [82], and then printed with an Object Connex [83] using Object Vero White Plus Full Cure 835 as printing material, as shown in Figure 2.12, right hand side. Its dimensions are reported in Table 2.2. To resemble the shape of human hand and arm, passive rigid ring and little fingers are also realized and included in the overall system. To ensure a lightweight structure, the hand is internally hollow. For demonstration purposes, a base is also included at the bottom, as shown in Figure 2.12, left hand side. The bottom base is also used to host the driving electronics.

2.6.2 SMA Hand motion and grasping evaluation

In order to demonstrate the SMA hand versatility, several achievable configurations are performed and the results displayed in Figure 2.14.
Starting from left to right in Figure 2.14, in the first frame, the actuator is shown with all fingers in the fully stretched position. In this configuration, only the antagonist wires of the three fingers are actuated. In the second frame, the first phalanx rotated position for the thumb (upper part) and for the middle finger (lower part) is displayed. In this case, the antagonist wires are no longer actuated, and only the protagonist SMA wires connected to the top phalanx are powered. In the third frame, only the protagonist SMA wires attached to the middle phalanx are actuated in order to perform the second phalanx bending while, in the last frame, full finger bending is achieved by actuating both protagonist wires for both fingers.
In Figure 2.14, a variety of achievable grasping configurations are depicted. Starting from left to right, upper frames, the actuator performs the grasping of a coffee cup, a screwdriver (with an irregular surface), and a pencil. In the bottom frames, the grasping of a rectangular box along its shorter and bigger side is performed, and the gripping of a pencil in writing posture is demonstrated. Note that, to improve the handling capabilities, some soft finger cups were 3D printed, using a rubber like material (Object Vero Black Plus Full Cure 875, in black in Figure 2.14).

Coefficient	Value (mm)
Hand	
Hand full length	315
Hand palm width	75
Hand wrist width	56
Hand palm length	55
Hand tip index- tip thumb distance	62

Table 2.2: SMA hand dimensions.

All the performed experiments demonstrate the effectiveness of the SMA hand in grasping several items with different sizes and shapes. During the tests, several difficulties are observed during the grasping of spherical objects, mainly due to the chosen design which prevents any abduction/adduction motion of the thumb. This design makes challenging also the grasping of big objects, since the maximum distance between the index and the thumb is smaller than the human one. Moreover, due to the small forces performed by each finger, much below the human hand capabilities, the handling of heavy objects is not feasible.

2.7 Summary and Chapter conclusion

In this Chapter, a concept for a new SMA-actuated biomimetic hand, aiming at emulating the biological structure of the human one, has been developed. In the structure of each finger, SMA wires are integrated in protagonist-antagonist muscle pair configurations, in order to enable versatile control and a comparatively fast rotation of the finger joints. The result is a versatile system that has a lightweight, robust, and low-cost structure.
Some experiments have been performed in order to measure the motion of each finger phalanx. Complete rotation with a satisfactorily responsive finger motion is obtained, with settling times of 1÷1.5 s for a ramp-shaped input (which ensures safety operating conditions for the material), thanks to small diameter SMA wires which allow higher surface-to-volume ratio. Moreover, a wire resistance change related to the wire measured motion (contraction/extension), and then to a finger change in configuration, has been measured and documented. This relation will enable future implementation of self-sensing concepts to track the finger motion without external position sensors.
Force measurements have also been realized to quantify the finger force. At first, a maximum force of 1.4 N of each phalanx has been evaluated. Then, a force trend has been obtained for the middle phalanx in order to quantify the force change in relation to different finger configurations. The SMA finger dynamic responsiveness has been evaluated in relation to a desired voltage input, showing a step response with 1 s and 1.5 s settling time for rising and falling fronts, respectively. Such a response time has been obtained, once again, by controlling the SMA wires under the safety limits suggested by the manufacturer [33]. The design of the full SMA hand has been presented and described. Its performance while handling different size and shapes objects has been investigated.
The prototype described in this Chapter demonstrates the validity of the proposed concept. The performances evaluated are sufficient for accomplishing several daily life operations, but, on the other hand, the measured finger force is still smaller than the average human one. Beside this, due to the limited space between the thumb and the index and to the high structure rigidity, objects with a medium/large size, generally handleable by an average-size human hand, result difficult or even impossible to grasp. All these limitations restrain the application of the introduced concept.

While performing the tests aiming at evaluating the prototype performances, undesired behaviors have been observed, i.e. wire residual strains, friction, uncomplete finger rotation, force hump. In particular, as a consequence of the SMA wire arrangement inside the fingers structure (electrically in series and mechanically in parallel), during the finger activation, contacts among some wires of the same bundle have been observed. As immediate consequence of this situation, an unexpected decreasing of the resistance of the entire bundle has been measured. This undesired phenomenon induces an increasing of the electrical current flowing inside the bundle and thus provokes possible damages. Furthermore, when this situation occurs, the self-sensing approach results impracticable.
All these undesired behaviors are strictly related to the chosen design.
We have to point out that, the mounting process of the SMA hand prototype is entirely based on handcraft work. Very good handcraft capabilities are especially required while inserting the 100µm diameter SMA wires along the finger phalanxes, inside the 0.25 mm diameter Teflon tubes. A standardization of the entire process described in Section 2.4 results quite difficult.
Considering all these aspects, an improvement of the overall structure is strongly needed.
In the following Chapter, in order to address all the biggest limitations related to the first generation of the SMA Hand, a second design concept will be introduced.

3 Second Generation SMA Hand Design

The design of a device able to reproduce all the functionalities of a human hand has been a challenge for many researchers since the late 1950'. As remarked in the previous Chapter, up to date, the most performant prototypes (in term of force, speed, and versatility) are designed with a rigid structure [1]–[6], [10], [69]. Despite the remarkable performances achieved by hand prostheses with rigid links, they have encountered high rejection rate by the users mainly due to the rigidity of the structure, their heavy weight and their noisy motion [11]–[13], [84]. Soft robotic hands represent a valuable alternative to this technology [84]. The increased compliance of these devices confers an intrinsic robustness to manipulation and, at the same time, safe features (due to their high mechanical compliance) which are highly desirable by the users [85]. For these reasons, soft robotic hands represent a big improvement towards the development of a human-like hand device. A first example of flexible hand is presented in [84]. In here, the authors introduce a underactuated two-finger prototype with reconfigurable joints actuated by two DC motors. From literature [86]–[88] it can be seen how most of the current soft hand prototypes are driven through pneumatic actuators. Even if pneumatic actuation represents the most used and effective solution in soft robotics, it exhibits several limitations when used for hand prosthesis applications. The requirement of a compressed air source together with its transportation systems (e.g., tubes, valves) inevitably increases the weight of the overall prototype, thus it is unsuitable for portable devices. Recently, a number of researchers started to prefer the use of electric motors in combination with deformable finger joints to design soft prostheses. The biggest advantage of this technology over pneumatic solutions is represented by compactness [89], [90]. Nevertheless, electric motors are still characterized by some limitations within the context of soft robotics, such as the requirement of rigid motion transmissions, heavy weight and noisy motion [12].
Due to the intrinsic elasticity and material properties of Shape Memory Alloys, it is possible to successfully use this material as a viable alternative actuator technology for soft prosthetic hands [91]–[93].
In order to overcome the main limitations of the SMA Hand concept described in Chapter 2, i.e., low force, rigid structure and handcrafted wires assemblage, and, at the same time, exploit the advantages of soft robotics technology, a new SMA actuated hand prototype having soft features is introduced in this new Chapter.

The remainder of this Chapter is organized as follows. Section 3.1 describes the design of the second generation of the SMA finger. Section 3.2 provides information about the prototype fabrication procedure. In Section 3.3, several experiments are performed with the goal of evaluating the prototype performances in term of force, motion and reactiveness. In Section 3.4, the SMA hand prototype design is introduced and its grasping capabilities

analyzed. The performance of this prototype while used as end effector of an *UR5* robotic arm are then described. Finally, a discussion over the SMA hand prototype capabilities in comparison with the most important commercially available prostheses is exposed. In Section 3.5, some concluding remarks and future research directions are outlined.

3.1 Finger design

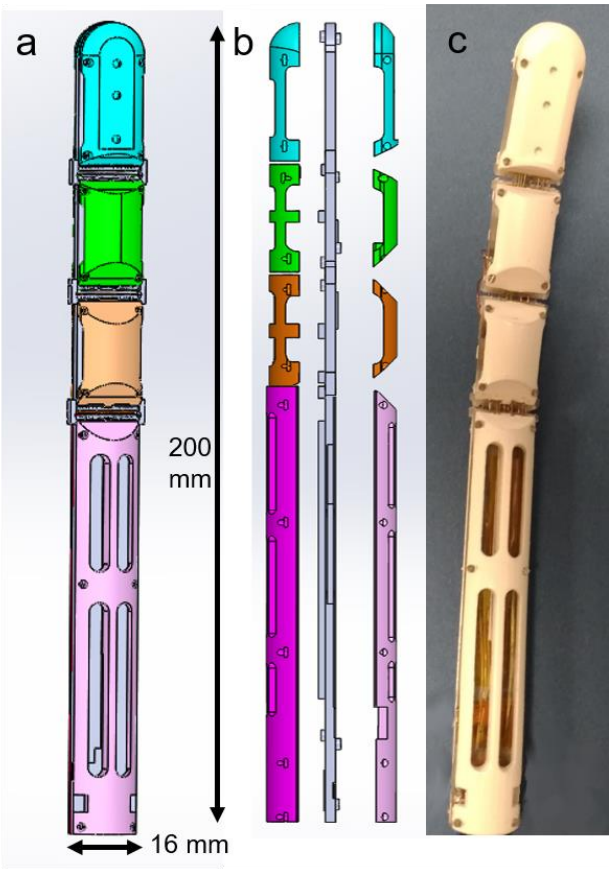

Figure 3.1: Finger structure. (a) CAD model of the full finger structure. Each phalanx is depicted with a different color. (b) Finger side split view. In grey the central part, where the SMA wires are fixed. The colored parts represent the external cover, which protects the SMA wires. (c) Printed and assembled finger prototype

In order to design a bio-inspired finger which is also functional and simple, the DOFs not strictly related to a grasping motion are neglected in this work [75]. The result is a 3 DOF prototype. Each finger has a modular structure. It is formed by three phalanxes and a stand, which represent the finger bone inside the palm, as shown in Figure 3.1. Each phalanx has a hollow structure in order to increase the overall lightness, while, to avoid undesired deformations, an arc shape pattern is used to design the finger cavities. Each finger has a modular structure composed by 9 parts, i.e. the external ones (colored parts in Figure 3.1

(b)), which have only a protection function, and the central parts (depicted in gray in Figure 3.1 (b)), which encapsulate all the SMA wires. Biologically, the human fingers are actuated by muscles located inside the arm and connected to each phalanx through tendons. Taking inspiration from the human biology, the SMA wires are collocated along the finger structure. When actuated via an electric current, the induced contraction is directly converted into the finger phalanx motion, acting at the same time as muscles and tendons. During the contraction, each SMA wire changes its electrical resistance according to the current length. Therefore, it is possible to relate its change in resistance to the finger motion and rotation [94]. According to this behavior, the SMA wires act also as nerves. Several SMA wire diameters are available on the market, ranging from 25 μm up to 500 μm [95]. In general, a thick wire is able to exert high forces but shows long cooling time when is not powered. Thanks to a better surface per volume ratio, thinner wires require a shorter cooling time than thicker ones but, on the other hand, are not able to exert high forces.
For these reasons, in order to achieve significant forces in the same range of human ones [75], bundles of 100 μm diameter SMA wires are used in this work [95]. Each SMA bundle is composed by 9 wires welded to a 10×5 mm stainless steel sheet, according to the procedure described in [96].

Coefficient	Value (mm)
Middle/Index/Ring/Little finger	
Finger top phalanx length	37
Finger middle phalanx length	29
Finger bottom phalanx length	30
Finger stand length	104
Finger width	16
Finger thickness	15
Thumb finger	
Finger top phalanx length	37
Finger bottom phalanx length	29
Finger stand length	90
Finger width	16
Finger thickness	15
Hand	
Hand full length	200
Hand palm width	116
Hand wrist width	85
Hand palm length	110
Hand wrist length	60
Tip prot. bundle length	55
Mid prot. bund length	165
Bot prot. bundle length	116
Tip ant. bundle length	61.5
Mid ant. bundle length	170
Bot ant. bundle length	122

Table 3.1: SMA hand system dimensions.

This process permits to systematically produce bundles of SMA wires having a repeatable and reliable behavior, since each wire is welded in the same state.
Due to limitations introduced by the welding process, each SMA wires needs to have a minimum distance of 1 mm with its 2 neighbor wires. Therefore, only five SMA wires can be welded on a 5 mm thick metal sheet. In order to maximize the number of wires, a "sandwich" shape bundle formed by two metal sheet laying on each other, having four and five wires respectively, is manufactured (as shown in Figure 3.2). According to Figure 3.2, the wires in the top bundle are properly placed in order not to overlap any wire of the bottom bundle. A copper tape is then wrapped around the two metal sheets at both sandwich bundle ends, in order to hold the sub-bundles together and power them at the same time. Metal screws are used to fix it to the finger structure. As for the previous SMA finger prototype, in order to enable the motion, a protagonist-antagonist configuration is adopted. This solution permits to achieve faster actuation speed in comparison to a conventional SMA-spring configuration, ensuring a stretching (carried out by antagonist wires) and bending (by protagonist wires) motion of each phalanx depending on which bundle is activated [26]. Each finger is designed in order to achieve the desired motion range by exploiting a SMA strain of only 3.5%, which represents the safe value for high lifetime [95]. The SMA wires dimensioning is obtained by means of kinematic and dynamic models formulated in [94], [97].

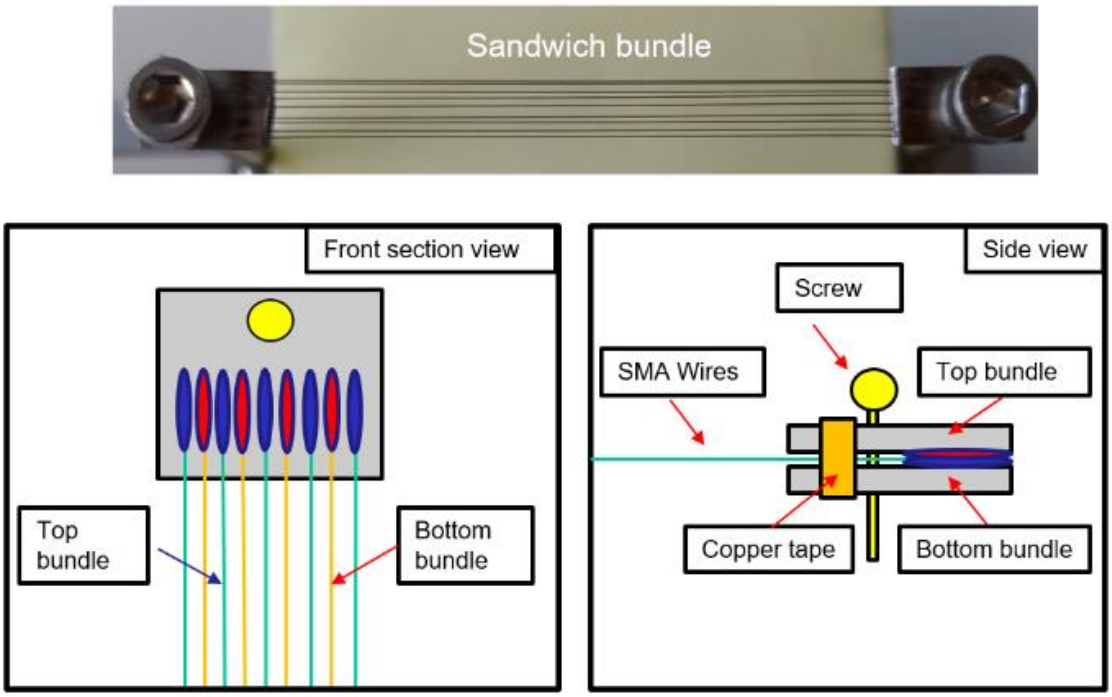

Figure 3.2: Design of the "sandwich" bundle. (Top view) Figure of the welded "sandwich bundle". (Bottom view) Sketch of the bundle structure. All its parts are highlighted.

3.1.1 Soft joints design

In order to enable a soft behavior in the hand prototype, each finger joint is designed to be flexible. As main requirement, the joint has to be designed to fit in the center part of the SMA finger (Figure 3.1 (b)), which is 2.5 mm thick.
Several elements, such as steel trusses [98] or polymer strips [90], can be integrated in the structure in order to design a soft joint. Despite their effectiveness, these solutions are hard to manufacture in an accurate way (i.e., steel trusses). In addition, it is difficult to achieve their miniaturization while ensuring effective compensation of all undesired moments. For this reason, superelastic SMA wires are chosen as passive components to connect each finger phalanx. This Nickel-Titanium alloys is characterized by a high lifetime and is commercially available already shaped as wire [95]. On the one hand, conventional actuating SMA wires are manufactured such that their austenite finish temperature is on the order of 90 °C. In this way, the transformation from martensite to austenite, and the subsequent length contraction, can be effectively triggered by an electric current. On the other hand, superelastic SMA wires are in full austenitic state already at room temperature. However, as explained in Chapter 1, when subject to a mechanical stress, they undergo a transformation from austenite to martensite, which is completely reverted as soon as the load is removed. By means of this effect, they can sustain an elastic deformation up to 10 % [21]. This feature makes superelastic SMAs suitable to be integrated as flexible joints in soft robotics structures.
In order to preserve the optimized hand design as in [97], the hinge joints are directly replaced by the superelastic SMA wires located along the joint vertical axis. In this configuration, the superelastic wires exert a passive stretching force in the structure, thus working against the protagonist SMA bundles. This design solution permits to decrease the number of active antagonists SMA bundles, decreasing also the amount of input power needed to actuate the fingers. In order to design a flexible joint which is also stiff enough to sustain the structure and provide a restoring force to the protagonist wires, different superelastic SMA wires topologies are tested.

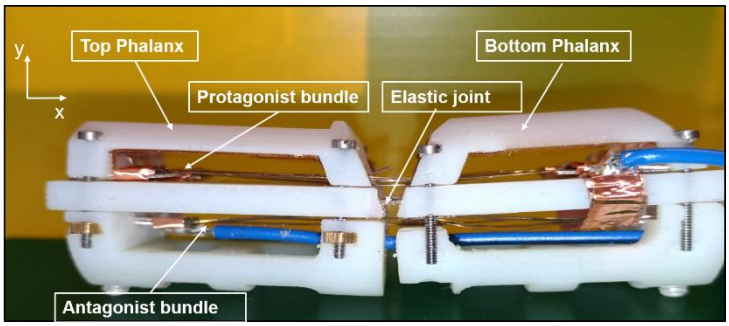

Figure 3.3: Two-phalanx finger prototype.

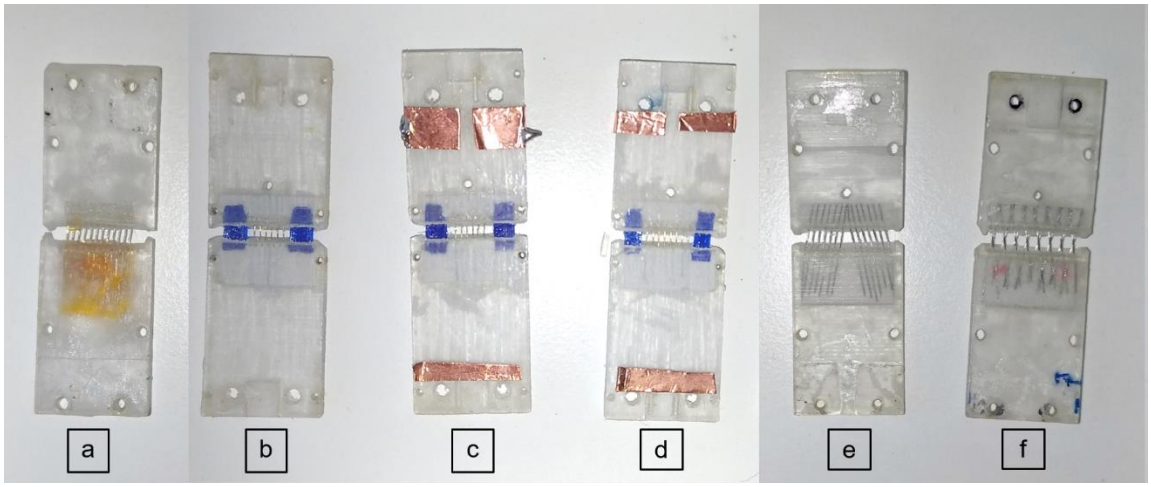

Figure 3.4: Superelastic SMA wires arrangement on a single phalanx. (a) vertical arrangement. (b) inclined arrangement. (c) x-shape arrangement.

To validate the different concepts, the two-phalanx finger prototype shown in Figure 3.3 is used. This prototype is composed by two central parts, in which three actuating bundles are located (two protagonist and one antagonist, respectively).
Four external parts are also used to protect the internal structure (blue and green parts in Figure 3.1 (b)). The central parts are connected by a soft joint while the external ones are held together through screws. This prototype represents the tip and middle phalanxes of the finger shown in Figure 3.1 (b) (in blue and green colors). As a first solution, the superelastic SMA wires are vertically arranged as shown in (Figure 3.4 (a)). After several tests performed varying the number of SMA wires in the joint, it can be noticed that this topology does not permit to compensate all undesired moments induced in the structure by the actuated SMA wires. When the protagonist SMA bundles are powered, after an initial rotation around the z axis (see Figure 3.3), an additional rotation around the z-x axes is induced to the top phalanx. This is due to the high stress state generated by the actuated bundles, which makes the wires in the joint collapse into a new preferred configuration.
Repeating this test several times, the superelastic wires undergo a permanent deformation (slightly visible in Figure 3.4 (a)), which makes the wire tilt on one side.
In order to compensate these undesired phenomena, following the literature trend for soft joint design, Ultimaker TPU 95A®, 3D printed material (hardness of 95, 580 % elongation at break) is selected to be used as soft finger joint (Figure 3.4 (b, c, d)). This material is quite elastic, lightweight and reasonably cheap. Several 3D printed trusses, having different width and thickness are designed and tested. The experiments involving this material, however, are not satisfactory since the TPU joint is still not able to compensate all undesired moments induced in the structure by the actuated SMA wires. Aside from that, the TPU joints are very difficult to be miniaturized, due the properties of the material. To note that, the finger middle part, containing the finger joints, is 2.5 mm thick.
Moving away from using plastic based joint, superelastic SMA wired in an inclined arrangement is considered as a new possible design solution (Figure 3.4 (e)). Several

experiments demonstrated that this configuration is able to effectively compensate lateral moments. On the other hand, if high stresses are induced by the protagonist SMA wires during the phalanx bending motion, new configurations are favored in which the wires collapse on themselves. This results into a reduction of the distance between the two central parts, thus preventing a complete phalanx bending motion. In order to avoid this phenomenon, a X-shaped topology is finally considered (Figure 3.4 (f)). Several tests demonstrate that this design is able to compensate every major undesired moment, while still allowing a slight lateral tilt if a force is acting on the phalanx side. When the protagonist SMA bundles are activated, a rotation around the middle point of every beam is induced. In order to find the perfect number and size of superelastic SMA wires to insert into the joint, several prototypes are designed and tested.

The use of thick wires increases the joint stiffness and, therefore, the achievable bending angle becomes smaller.

Moreover, the mounting process becomes harder since a high rigidity of the wires contrasts the overlapping procedure while building the X-shape joint. On the other hand, the use of thin SMA wires prevents the compensation of the stress induced by the protagonist bundles when activated, leading to a reduced lifetime and to several damages at the wires overlapping points. By accounting for all these factors, and after comparing different wire diameters among the ones available on the market (25 μm to 500 μm) [95], superelastic SMAs having a 200 μm diameter are chosen for the final design.

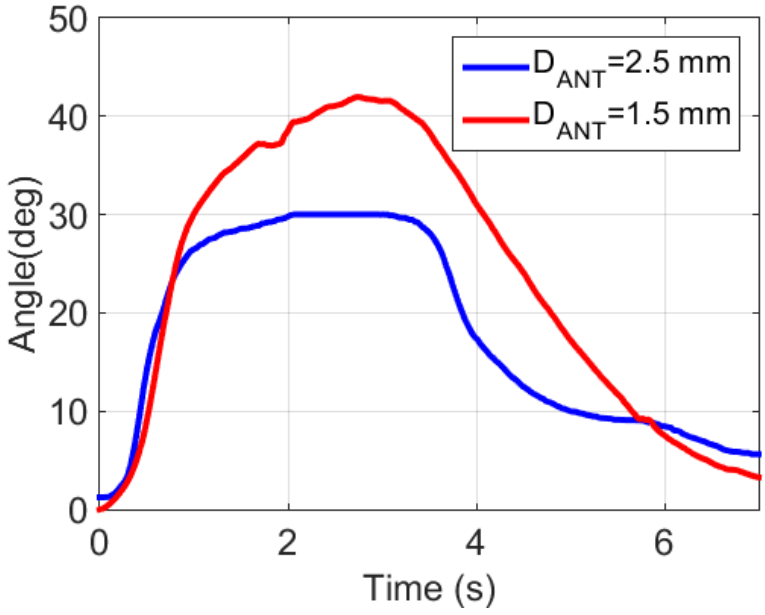

Figure 3.5: Two phalanxes finger behavior, varying D_{ANT}.

3.1.2 SMA bundle positioning

As already described in the previous Chapter, the arrangement of the SMA bundles inside the finger structure is a quite challenging problem. When the SMA wires are positioned very close to the phalanxes center of rotation (in this case, the middle point of the superelastic joint), a small wire strain can induce a big rotation angle, at the expense of the maximum achievable force at the fingertip. Increasing the distance, the force increases, but a bigger strain, and thus longer wire, will be requested to achieve a complete rotation of the finger phalanxes. In the previous Chapter, the kinematic model and the experiments have demonstrated that a distance D_{PROT} in the range of 1.5~ 2.0 mm between the rotation center and the protagonist bundles is enough to guarantee adequate motion performances. We have to point out, that a distance smaller than 1.3mm is not possible for design constrains. On the other hand, no systematic experiments or simulations regarding the arrangement of the antagonist SMA bundle have been so far collected. Since, one of the main design goals is to obtain a very compact SMA finger structure, a D_{PROT} = 1.5 mm is chosen for the protagonist SMA wires. To increase the finger prototype force, the number of protagonist bundle is maximized. In order to decrease the system input power needed to activate the prototype, the number of passive superelastic SMA wires mounted in the joint is maximized, according to the space available in each phalanx (14 wires having 0.2 mm diameter each). The number and distance of the antagonist SMA wires from the rotation center remain, therefore, to be determined.

For this reason, several experiments are realized using the two phalanxes prototype showed in Figure 3.3 and varying, at first, the number of antagonist wires and then D_{ANT}.

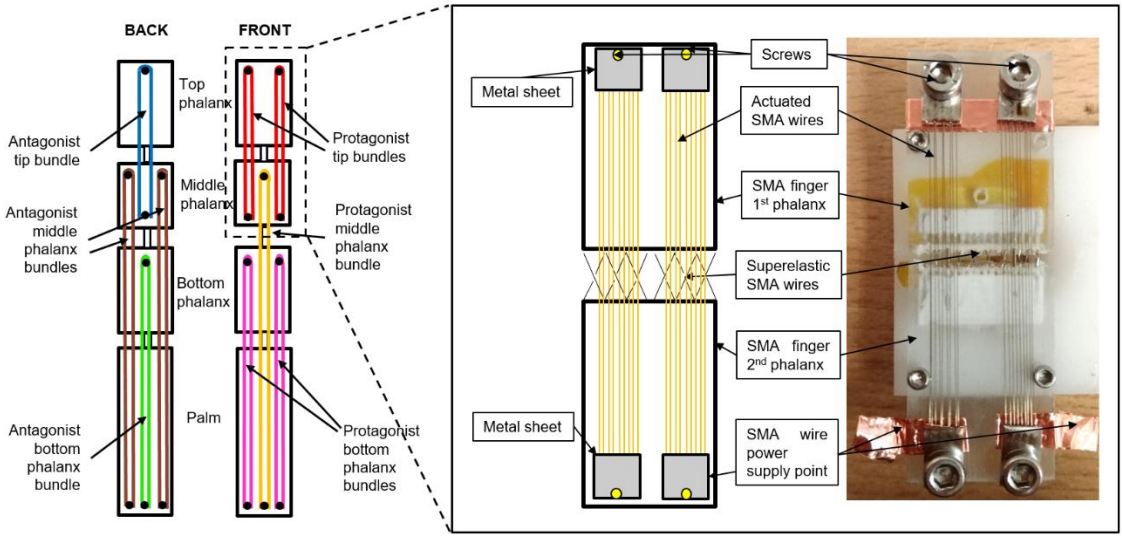

Figure 3.6: (Left-hand side) SMA wire arrangement inside the finger structure. (Right-hand side) Comparison between design and prototype. The electrical connections are also displayed.

The experiments are performed activating the SMA bundles using recommended value of input power [78] and recording, through a web camera, the motion of the movable phalanx. To generate motion, while the protagonist wires are activated, the antagonist ones are not powered, and vice versa. The experiments show that, using 18 protagonist SMA wires (2 sandwich bundles as in Figure 3.2, upper part), 9 antagonist SMA wires (1 sandwich bundle) are sufficient to restore the finger stretched position. In Figure 3.5, the system behavior varying D_{ANT} is shown. As for the protagonist bundles, a distance smaller than 1.3mm is not possible for design constrains. For high values of D_{ANT}, the system has a good transient behavior (1 s rising time and 2 s falling time), but only 30° rotation are performed, since the moment exerted by the antagonist wires has a big influence in the system behavior. Decreasing the distance D_{ANT}, instead, a rotation of 40° is achieved, since also the corresponding moment decreases. Using this last configuration, the transient behavior is slightly worsened, but, on the other hand, a better recovery of the prototype straight position is enabled. This performance is achieved since, in this configuration, less strain is required to the SMA wires to accomplish the desired phalanx motion. Therefore, a D_{ANT} = 1.5 mm is also chosen for the antagonist bundles.

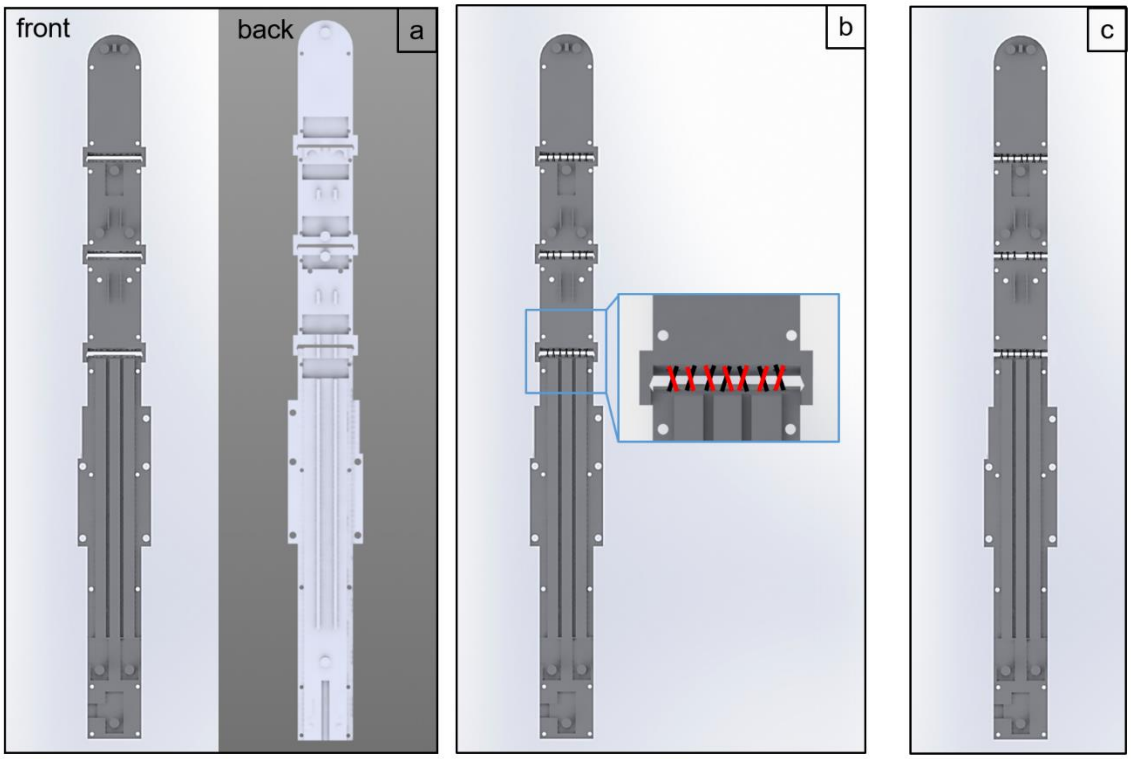

Figure 3.7: Finger structure design and superelastic SMA wire mounting.

Due to the encouraging results, the structure and wire arrangement adopted for the 2 phalanxes prototype in Figure 3.3 are scaled and used for the entire finger prototype. Its wire arrangement is shown in Figure 3.6, left-hand side. In this picture, we can notice that

first and third phalanx have the same SMA bundles and soft joint assembly of the 2 phalanxes prototype, while, in the second phalanx, the wire topology is slightly different. This mismatching is mostly due to the lack of space inside the finger structure. In order to limit the prototype overall dimensions and place all SMA bundles at the right distance to the rotation center, one protagonist and two antagonist bundles are connected at the second phalanx (respectively in orange and brown in Figure 3.6, left-hand side). To allow a correct motion of this phalanx, the number of superelastic SMA wire in the joint is decreased from 14 to 12 elements. The SMA wires dimensions of each bundle are obtained by means of kinematic and dynamic models formulated in [94], [97] and reported in Table 3.1.

3.2 Fabrication

The fabrication of the SMA actuated finger consists in several steps, listed in the following:

- *Step1* – the finger structure is first designed in Solidworks, and then 3D printed with an Object Connex 500. In Figure 3.7 (a), the back and front side of the structure central parts are shown. The back side has several rectangular cavities, designed to simplify the superelastic SMA wire mounting process;
- *Step 2* – the printed structure is cleaned with isopropanol. Superelastic SMA wires having a 200 μm diameter are inserted in the central part, along small holes designed at both end of each phalanx, following the pattern displayed in Figure 3.7 (b). In this picture, a zoom of the wires arrangement is shown. In order to avoid any possible induced local moment, the wires in red have to be mounted first, according to the depicted schema. Once arranged all the wires in the structure, high temperature white epoxy glue is then used to fix them, filling completely the rectangular cavity. After a day of curing time, in order to enable the motion of each phalanx, the 3D printed brackets, holding the joint at each side, have to be erased using a file, as shown in Figure 3.7 (c);
- *Step 3*– two bundles are manufactured according to the welding process described in [96], having 5 and 4, 100 μm diameter SMA wires, respectively. The bundles are then overlapped as shown in Figure 3.2, in order to have the wires laying on the same plane. A copper tape, having conducting glue on one side, is then used to hold the two bundles in the desired position. The procedure is repeated for all nine bundles (Figure 3.6, left-hand side). The length of each bundle is reported in Table 3.1;
- *Step 4* – electrical connections are realized along the structure. In order to save space and ensure a lightweight structure, copper tape, having conducting glue on one side, and coil wires are mainly used. At first, the copper tape is fixed to the finger structure according to Figure 3.7 (d-e-f). The copper is arranged in order to ensure that, once mounted the SMA bundles in the structure, each couple of bundle plates

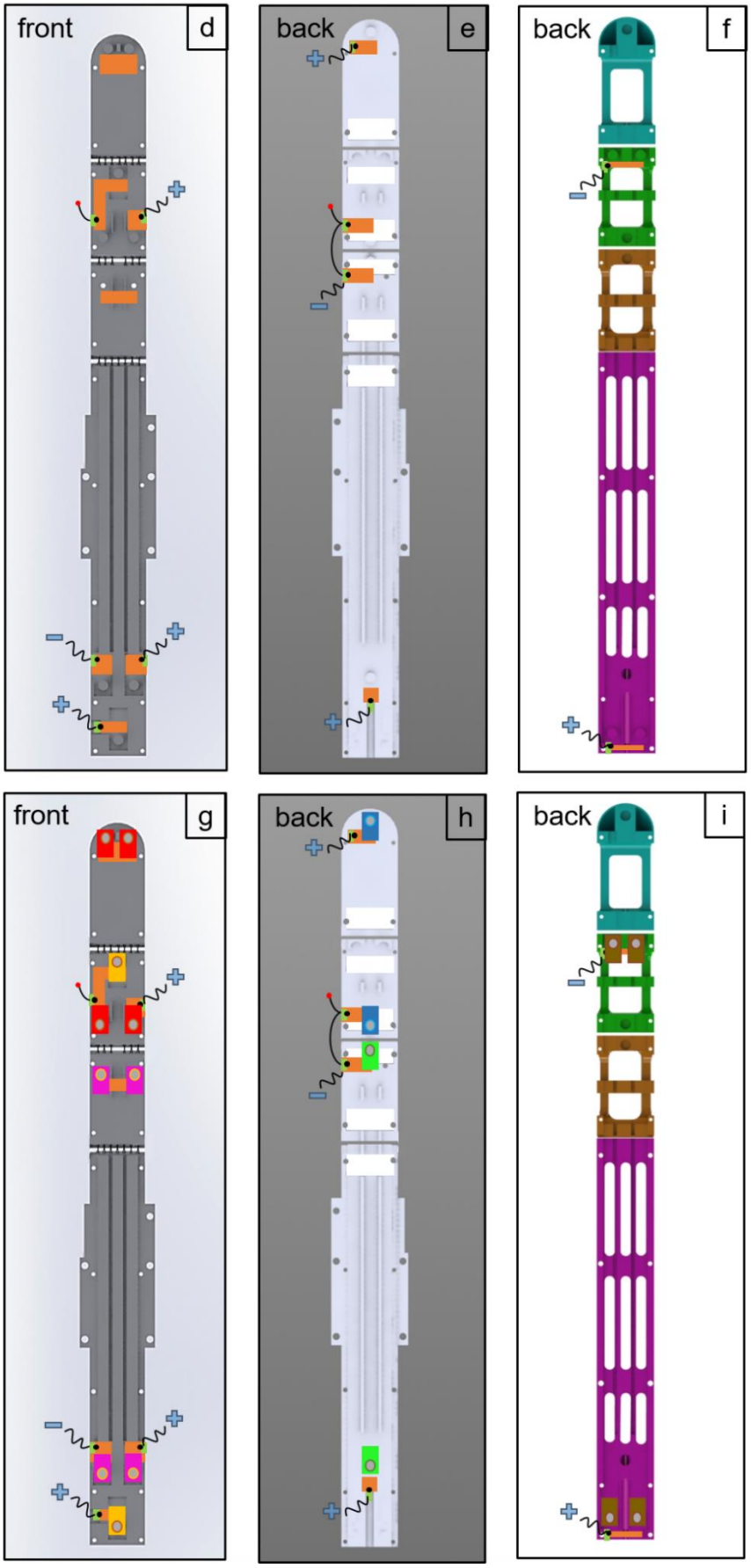

Figure 3.8 : SMA finger fabrication procedure.

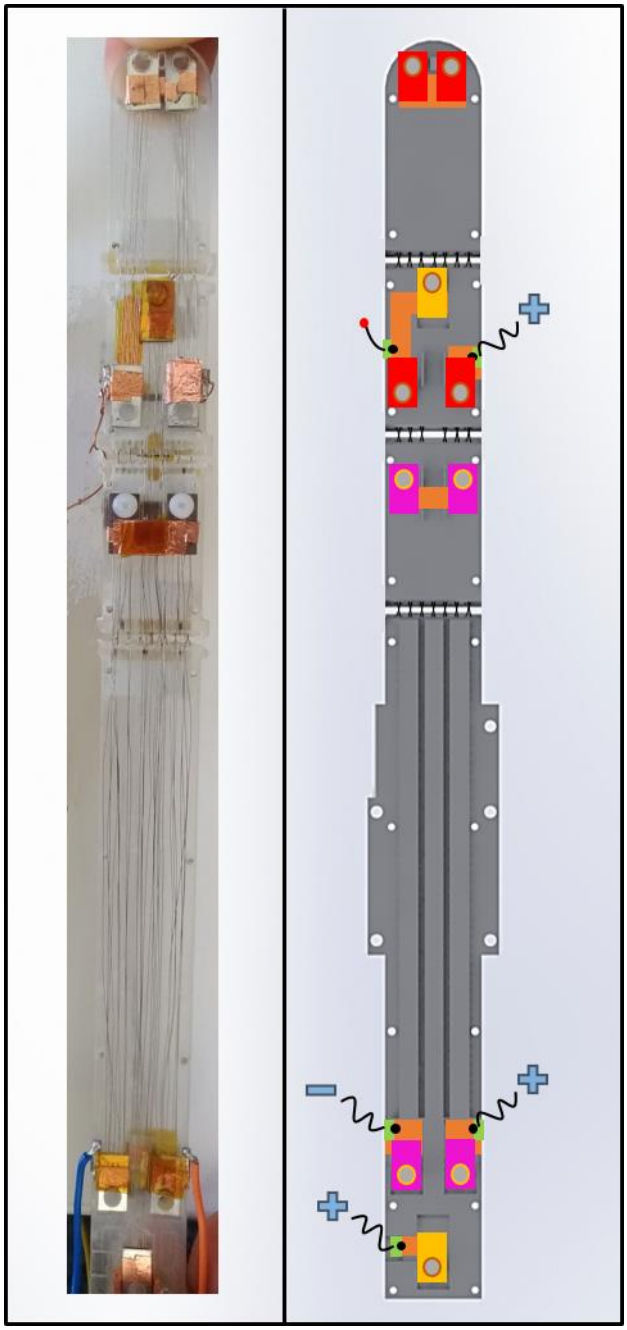

Figure 3.9: Comparison between the finger central part schema and the real prototype. (Right- hand side) Prototype design. (Left-hand side) Real prototype.

make good contact with it, as shown in Figure 3.6, right-hand side. Then, small 0.5 mm thick conductive boards are glued to the finger surface (in green in Figure 3.7 (d-e-f)). To ensure a reliable electrical connection, one small end of the copper tape is soldered to the board. At the end, the coil wires are soldered to the boards. The conductive boards are used as bridge between the copper tapes and the coil wires, to increase the bounding lifetime. During the finger actuation, indeed, the coil wires are subjected to several stresses and a direct bound with the copper tape would result not durable. The coil wires are arranged according to Figure 3.7 (d-e-

f), in order to minimize the electrical connections. The complete finger prototype has seven electrical wires, 6 to power the finger bundles (one for each bundle) and one common ground;

- *Step 5* – antagonist and protagonist bundles are mounted in the finger structure. It is worthwhile noting that the tip bundle is not connected to the palm. This arrangement permits to save space in the structure, thus making it available for the bottom SMA bundle. During the bundles montage, a complete isolation between different bundles set is ensured using Polyimide film insulating tape (i.e. Kapton tape) over the bundles plates. A comparison between the finger middle part schema and the real prototype is visible in Figure 3.9.

The presented bundle arrangement provides full control of each phalanx, since the activation of each single bundle leads to the motion (stretching or bending) of one different phalanx.
At the same time, this solution ensures shorter wires in each bundle. For a comparison, a single 300 mm long protagonist SMA wire and a single 500 mm long antagonist one would be required to allow full bending and stretching of the structure, respectively. With this design, the prototype size would have been unsuitable for applications. The external structural pieces are mounted around the finger central parts, in order to protect the wires and the connections.
In general, hand prostheses presented in literature have a quite complex structure, and their manual assembly often requires a significant effort [9]. On the other hand, the procedure to assemble the SMA Soft Hand, described above, involves simple and systematic steps that do not require any complex manual work. Indeed, the realization of the SMA bundle has been already full automatized [96], and the assembly of the entire structure is quite straightforward. For this reason, the fabrication of the entire hand prototype could be easily integrated in an automatic production chain, avoiding any efforts from a human worker.

3.3 Finger performance evaluation

Evaluation of actuation performance of a single finger is first presented in this Section, in terms of force, bending angle, and actuation speed. Subsequently, the grasping capabilities of the complete hand actuators are showcased.

3.3.1 Finger force

In this Section, force measurements are realized in order to evaluate the prototype capabilities. Since all of the hand fingers have the same structure and wire arrangement, only the force of a single finger is evaluated.
The experimental test bench is shown in Figure 3.10 and consists of the SMA finger, a vice screw, a Futek LSB 200 load cell, and ThorLABS adapters. The vice screw is anchored to a black breadboard through screws, and holds the finger prototype in correspondence of the palm part (Figure 3.6, left-hand side). The load cell is connected to the ThorLABS adapters, in order to easily adjust its position in relation to the desired force evaluation point. Both load cell and finger prototype are connected to a FPGA National Instruments cRIO-9074 real-time data acquisition system, interfaced with LabVIEW 2012. The FPGA is connected with a NI 9472, a switch module able to supply up to 30V DC, and a NI 9237, which represent the hardware interface between any load cell and LABVIEW. A custom electronic board is developed in order to drive each bundle independently, by activating its correspondent MOSFET in the board. By connecting each MOSFET with an output of the NI 9472 module, it is possible to drive the corresponding SMA bundle independently of the others with a desired input signal. In all the experiments, the electric power is chosen as control input for the SMA wires. In fact, differently from voltage and current, the electric power affects the SMA temperature in a proportional way [65]. As mentioned in Chapter 1, when a SMA wire temperature increases, it undergoes a phase transformation which leads to a change in both length and electrical resistance. This fact also implies that a constant power cannot be obtained by simply keeping the voltage or the current constant. Therefore, to drive the SMA fingers, a power control strategy is properly implemented in the experimental setup. Since many nonlinear phenomena occur in the structure (e.g., contact friction between the SMA wires and the structure, influence of superelastic SMA), we decided to evaluate the force with a direct measurement of the load cell at the fingertip middle point. The choice of the force application point is motivated by the fact that, during daily grasping operations, objects are mostly handled by using the hand fingertips. It is pointed out that the measured force is not constant along each finger phalanx, but it increases as the load cell is moved closer to the phalanx center of rotation. In order to measure an average representative value, the fingertip middle point is chosen for force evaluation, represented by the second circle starting from the top designed at the fingertip front part (see Figure 3.1 (a)). The load cell is positioned in front of the fingertip, with a small gap between the two, in order to measure the prototype force as soon as the desired SMA bundles are activated. These experiments permit to measure the true finger force, avoiding any influence of additional contact forces such as the friction between the finger prototype and the item to handle.

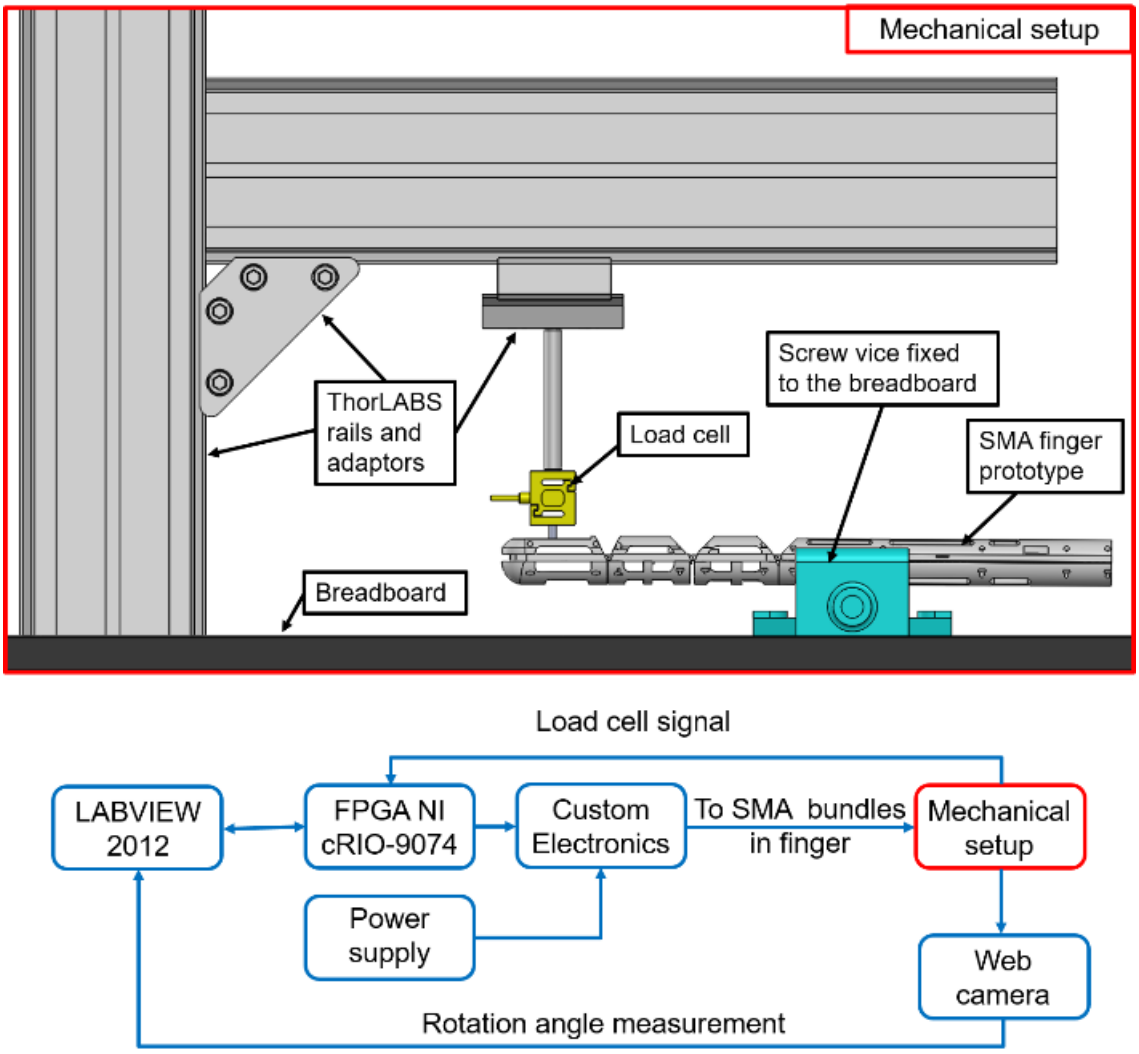

Figure 3.10: (Lower part) Force measurement diagram. (Upper part) Detail on the mechanical setup.

The tests results are depicted in Figure 3.11. Moving from the left- to the right-hand side, the force of the protagonist bundle actuating the tip, middle, and bottom phalanx are shown, respectively. On the right-hand site of Figure 3.11, the finger overall force, obtained by activating all the protagonist bundles, is depicted. It is interesting to notice how the measured force of the top phalanx bundle is higher than the force of the bottom one, even if they have the same number of wires and the same SMA diameter. This phenomenon occurs because we are measuring the force far from the bottom phalanx center of rotation, and thus the force induced in the load cell has a large lever arm. On the other hand, the soft structure deforms itself under the load cell induced moment according to other preferred configurations, limiting the force component acting against the load cell.
Figure 3.11 shows how the maximum achievable force for the SMA actuated finger, in the analyzed configuration, is almost 9 N. This value is comparable with the human finger one [75]. From this force value, we can estimate a force of 45 N for the overall hand.

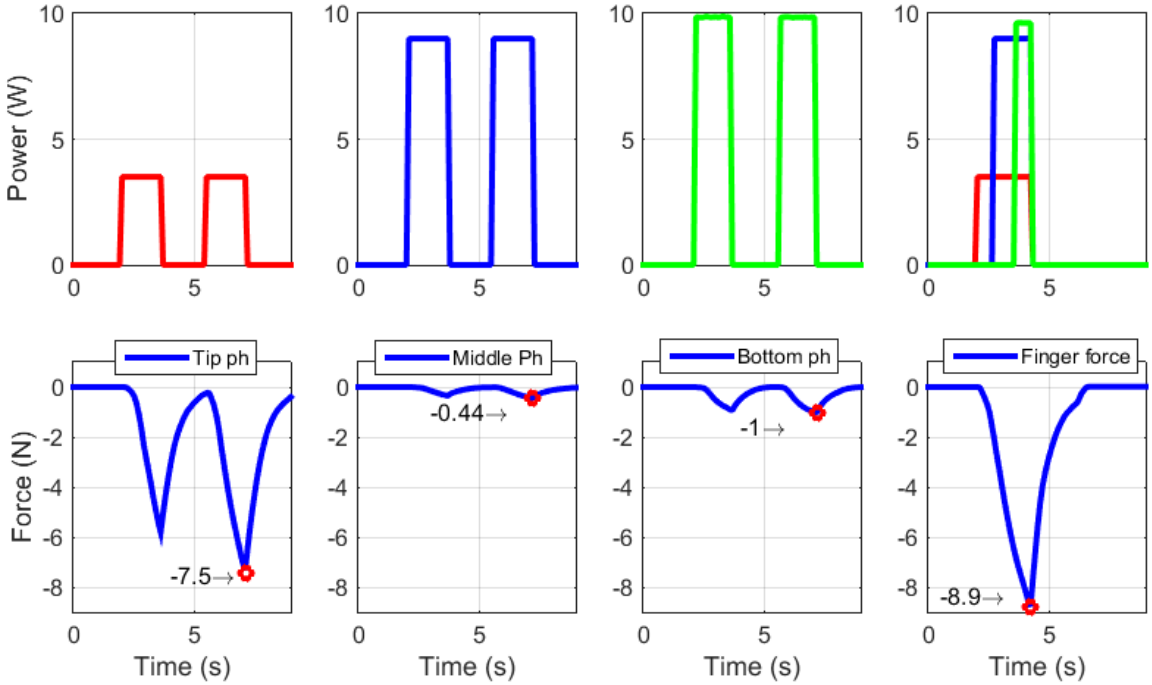

Figure 3.11: Forces evaluated at the fingertip actuating different protagonist SMA bundles at time, i.e. activating the bundle connected at the finger (left-hand side) top phalanx, (center-left-hand side) middle phalanx,(center-right-hand side) bottom phalanx. (right-hand side) Forces evaluated at the fingertip actuating all the three protagonist SMA bundles in the same time.

3.3.2 Finger motion

In this Section, the maximum achievable displacement of each phalanx of the finger prototype is experimentally evaluated. The experimental bench is very similar to the one showed in Figure 3.10, and it is composed by a FPGA National Instruments cRIO-9074 real-time data acquisition interfaced with LabVIEW 2012. The FPGA is connected with a NI 9472 module. A custom electronic board is realized able to drive each bundle independently from the others. During each test, one channel of the NI 9472 is enabled at LabVIEW control logic, allowing to supply a desired power profile to the MOSFET which, in turn, is connected to one bundle of the finger phalanx. In this way, each finger phalanx can be controlled indipendently of the other ones. In order to measure the finger motion, a Logitech webcamera is interfaced with LabVIEW and syncronized with the other NI module. At each sampling time, a video frame is recorded. The acquired video is then postprocessed with a MATLAB routine, and the signal desccribing the rotation angle over time is reconstructed. The antagonist SMA wires are activated at the beginning of each experiment, in such a way to ensure a fully straight initial configuration for each phalanx.

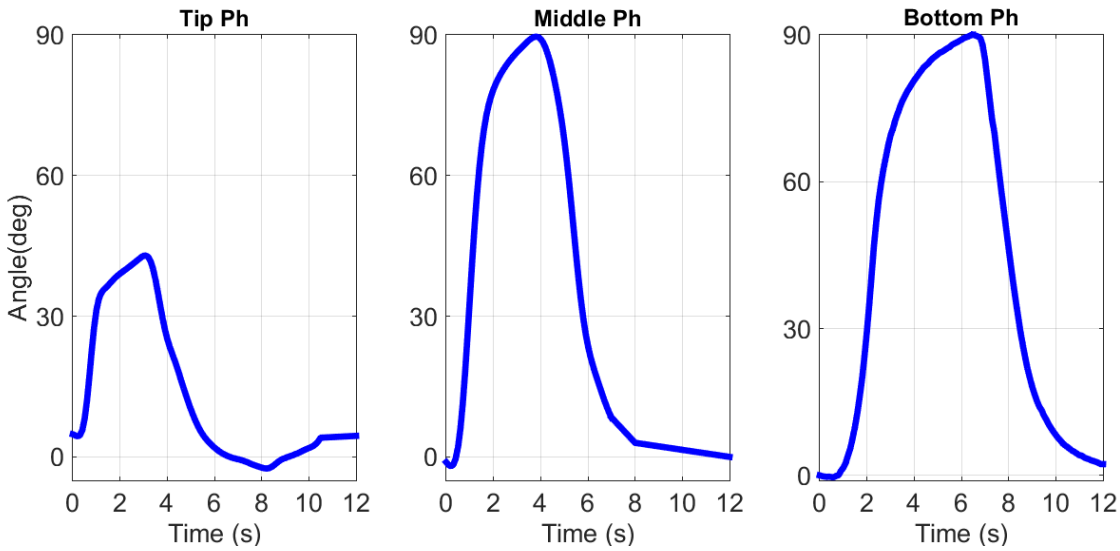

Figure 3.12: Finger phalanxes angular displacement. (Left-hand side) Top, (center part) middle, and (right-hand side) bottom phalanx displacement.

Then, according to the desired input power signal designed in LabVIEW, the antagonist wires are deactivated while the protagonist SMA bundles are powered. The measured angles are displayed in Figure 3.12. From this picture, it can be verified that the prototype displacement performances are comparable with the human finger ones, and permits a wide range of motion [75]. We have to highlight that the displacement of the human hand tip phalanxes varies from 45 ° up to 90 °, moving from the ring to the little finger [75]. On the other hand, during any grasping motion, the tip phalanx of each finger rarely reaches 90 ° of displacement. For these reasons, in all the commercial active prostheses, the tip finger phalanx joint is always designed to be fix with an orientation of 20 ° with the respect of the middle phalanx [9]. Since the tip phalanx favors the grasping stability, in this work it has been designed to be movable. As shown in Figure 3.6, reducing the length of the top bundles, and thus their actuation strain, makes it possible to increase available space to setup the bottom bundle. Therefore, 45 ° is chosen as top phalanx maximum motion. Figure 3.12, left hand side, shows as the theoretical value is reflected in the measurements.

3.3.3 High-speed activation

In the previous Section, the maximum displacemet of each finger phalanx is investigated. During each experiment, conservative values of current and voltage are used to power each SMA bundle [95]. In general, the SMA wire producers recomend “safe” current values to be supplied to the wires in order to prevent any damage in the crystal structure also if the wires are continuosly powered for long times. Aside from this approach, it has been demonstrated that SMA wires can be activated much faster if powered via short pulses of

high amplitude current [80], [81]. This type of activation leads to no damage in the wire structure, if the pulses are properly designed.

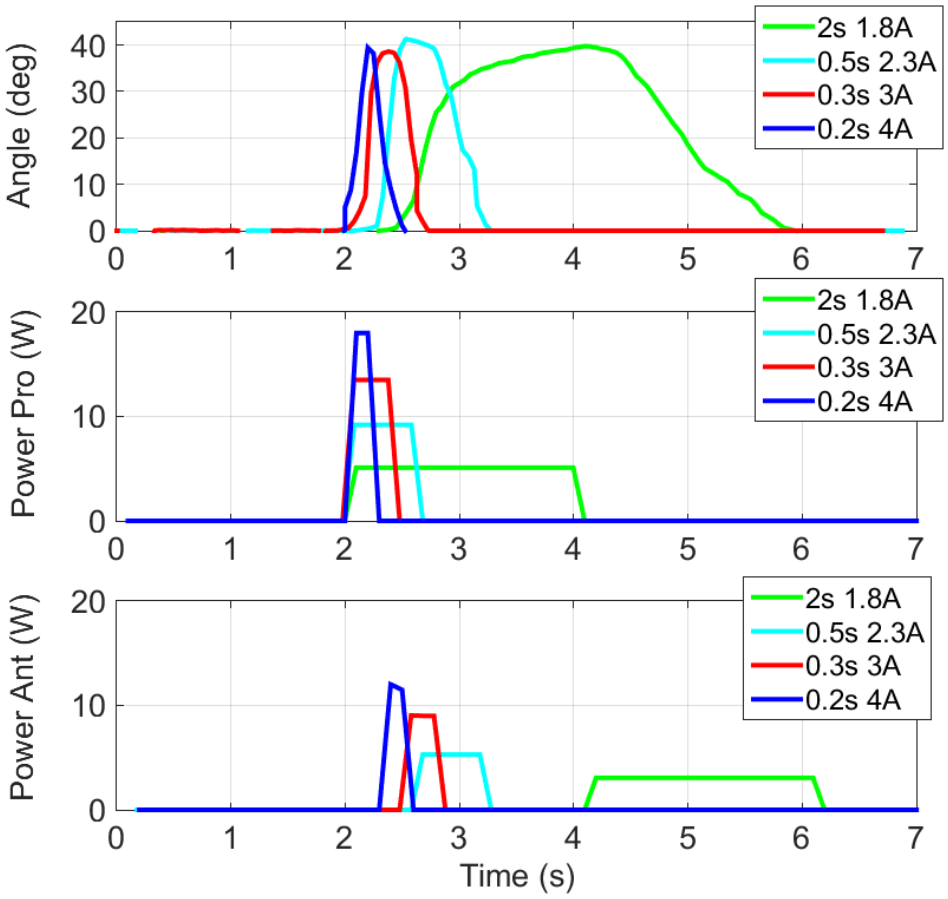

Figure 3.13: High speed activation of the protagonist and antagonist bundles in the fingertip. (Upper part) top phalanx angular displacement, (center part) input power protagonist bundle, (lower part) input power antagonist bundle.

The energy that has to be provided to the system with the short pulses needs to be sufficiently high to induce a fast phase transformation in the material. At the same time, the pulse should be long enough to let the wire temperature not increase above its austenite finish temperature, which is around 90 °C for Ni-Ti alloys. This method enables high activation speed of the SMA bundles using reasonable values of input energy. In order to reach activation speeds closer to the ones of human hand, the pulse activation method is tested on the SMA fingertip phalanx. For the experimental campaign, the test bench described in the previous Section is employed, using several input current values having different amplitude and duration. At the beginning of each experiment, all finger bundles are not activated. The results of the experimental campaign are shown in Figure 3.13, where several measured angles and their correspondent input power signals are depicted. In this figure, the green line represents the phalanx angular displacement achieved using “safe” values of input power. In this case, the settling times for the rising and falling rotation steps

are about 1.6 s and 2 s, respectively. This difference in time depends on the number of bundles involved in the motion, i.e., two protagonist and one antagonist SMA bundles. Decreasing the duration and increasing the magnitude of the input power pulses leads to an increase of the prototype reactiveness. The blue line represents the fastest achieved motion, characterized by settling times for the rising and falling rotation steps of about 0.2 s and 0.3 s, respectively. It is not possible to record more performant results with the available setup, due to hardware limitation of the used web camera. Nevertheless, the achieved performance appears comparable with the human hand during daily based operations [75]. This approach can be used both in case of an impulsive action (e.g., playing a piano) as well as for long time grasping tasks (e.g., holding a bag). In the first case, power profiles described by the blue line in Figure 3.13, (center and lower parts) can be used to supply the fingers bundles. In the other case, the pulse activation method must be followed by a constant power having a more conservative value (Figure 3.11, upper part), which need to be applied continuously to keep the finger at a fixed position. The value of such a constant power is defined by length, diameter, and number of wires welded in each bundle [95]. In particular, the value of the input current is related to the wire diameter (the bigger the diameter, the smaller the current required to heat the wire to a given temperature). Instead, the wire length influences the input voltage value (the longer the wire, the higher the voltage required to heat the wire to a given temperature).

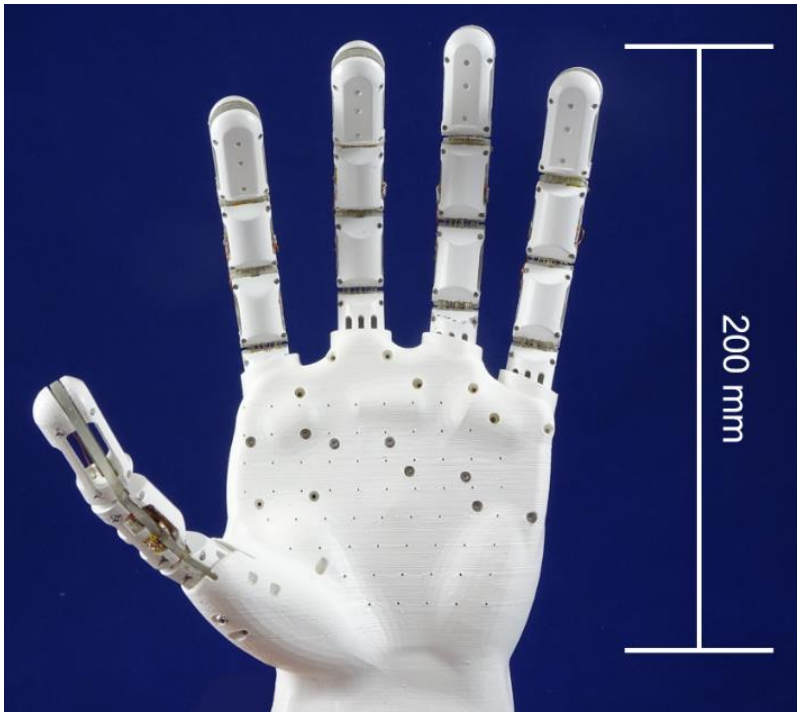

Figure 3.14: Five-fingered SMA Soft Hand front view.

In the finger prototype, the bundles are composed by several SMA wires having the same diameter, therefore each wire receives the same amount of input current. On the other hand,

each group of bundles (shown in different colors in Figure 3.6) has a different length, and therefore the input voltage amplitude differs in each bundle group [95].

3.4 SMA Soft Hand structure

The hand is the most complex and articulated part of the human body. It is composed by 27 bones and 17 articulations, resulting in an overall number of 23 degrees of freedom (DOF) [75]. In order to design a bio-inspired prosthesis which is also functional and simple, the DOFs not strictly related to a grasping motion are neglected in this work [75]. The result is a modular 14 DOF prototype, depicted in Figure 3.14. It consists of a palm and five fingers connected to the entire structure through screws. In order to simplify the design and ensure at the same time an effective grasping motion, the thumb is designed with an angle of 90 ° with respect to the hand palm surface. The system CAD (shown in Figure 3.15) is first realized in Solidworks, and then 3D printed. In particular, the fingers are 3D printed with an Object Connex, using Object Vero White Plus Full Cure 835 as printing material, while the palm is 3D printed with an Ultimaker 3 Extended using white PLA as printing material. The structure design is dimensioned with respect to the average size of an adult man hand, as reported in Table 3.1, and shaped according to the human hand morphology. To ensure a lightweight structure, the hand and the fingers are left internally hollow. The middle, ring, index and little fingers are designed according to the finger prototype described in Section 3.1. The thumb is also designed according to the human biology, and thus, composed by only 2 movable phalanxes, corresponding to the tip and middle ones of Figure 3.6 (left-hand side).

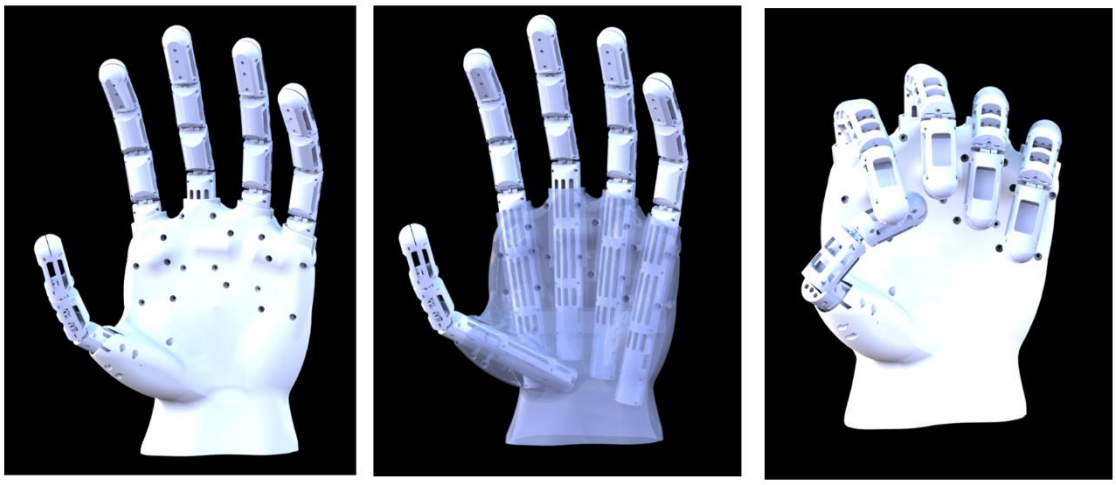

Figure 3.15: Hand structure. (Left-hand side) External view. (Center) Palm internal view. (Right-hand side) Hand closed configuration.

To embody the fingers inside the hand palm, some guides are created, as visible in Figure 3.15 (center part). Since, during any grasping action, the human fingers never remain

parallel to each other, but they arrange themselves according sunburst directions, the guides for the fingers are designed slightly tilted. In this way, it is possible to grasp both relatively big and small objects, since, when the fingers are rotated, their tips converge toward the same point, as shown in Figure 3.15 (right-hand side). Once inserted in the hand palm, each finger is secured to the structure thought several metal screws (the screws guides are visible in Figure 3.15, left-hand side). This modular structure ensures an easy assembly of the full prototype and, on the same time, a fast replacing of the fingers in case of damages. As described in Section 3.2, each finger has 7 power cables, one for each group of bundles and one ground. Therefore, the entire hand prototype has 35 power cables. In order to simplify the mounting process and, eventually, enable a connection with a robotic arm, circular electrical connectors are used. Each connector has 8 pins able to handle up to 32 A (4 A pro pin). Before mounting the fingers inside the hand palm, each pin is soldered to a power cable (linked to a group of SMA bundles), while one is left unconnected.To secure the contact while actuation, an external screw can be used to lock the female and male connectors as shown in Figure 3.16. The SMA hand is interfaced to a microcontroller in order to perform desired grasping movements. Since each group of bundles in the finger prototype has a different length and thus need to be supplied with a specific value of input power, a custom electronic board has been developed and interfaced with the microcontroller. This board gives also the possibility to interface and synchronize the SMA hand with an external robotic arm.

3.4.1 SMA Soft Hand grasping capabilities

As described in Section 3.1, the finger-environment interface consists of rigid and elastic parts. The rigid part is represented by the 3D printed finger phalanxes front parts (Figure 3.1 (b)). The elastic part is represented by the passive superelastic wires, which undergo large deformations when subjected to mechanical stresses. This design enables soft features in the hand structure. In order to demonstrate these features, the hand prototype is fixed to a breadboard laying on a table. In order to mimic a potential impact between the prototype and an obstacle, the prosthetic fingers are slightly hit by a human hand. In this case, the contact force results into an elastic force in the superelastic SMA. Therefore, the prototype finger joints deform, thus preventing any damage of both the prototype structure and the human hand. Once the obstacle (the human hand) is removed, the prototype fingers regain the original initial position. In Figure 3.17, the grasping capabilities of the complete SMA Soft Hand prototype are demonstrated. Four objects, having different size and shape, are chosen for the grasping experiments. In this way, several possible shapes (round/square, wide/thin) are investigated. During these experiments, the hand prototype is fixed to a commercially available breadboard using some screws and a custom basis. Each object is drawn near the prototype grasping area by the user.

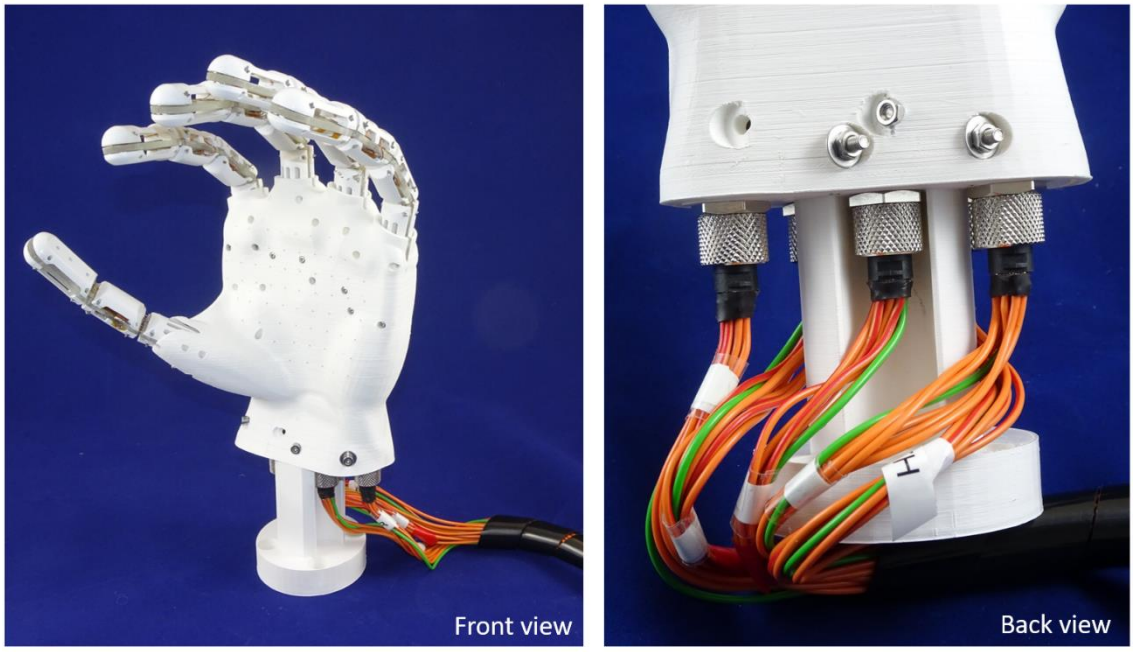

Figure 3.16: Prototype electrical connections. (Left-hand side) Front view. (Right-hand side)Back view.

In order to enable the independent motion of all the fingers, each phalanx is driven by a different output channel of an Arduino Mega®. Two different open-loop control strategies (one for the lateral and the other for the full hand grasping) are implemented in order drive each phalanx in a desired way. Prior to each experiment, the control strategy is manually tuned by the user.

Starting from Figure 3.17, left-hand side, the lateral grasping of the hand is depicted. Using only two fingers, the prototype is able to grasp both small and big objects, such as a screwdriver and a ball, respectively. This posture enables writing capabilities, e.g., if a pen is grasped. On the right-hand side of Figure 3.17, a grasping process based on more fingers is demonstrated. In this way, it is possible to better handle objects with different shapes such as a small ball and a rectangular plastic brick.

All of the performed experiments demonstrate the handling capability of the presented hand prosthesis. It is remarked how an unstable grasping of extremely smooth objects is also observed. This is mostly due to a lack of friction force provided by the 3D printed material used for the fingers structure. In order to improve the prototype grasping ability, in future works a soft silicone finger cover will be developed to mimic the human skin and, in turn, improve the grasping stability.

Figure 3.17: Complete SMA Soft Hand grasping capabilities. In the two pictures on the left-hand side, the grasping of a screwdriver (upper part) and of an orange ball (lower part) using two fingers (lateral grasping) is depicted. In the pictures on the right-hand side, the grasping of a blue ball (upper part) and of a rectangular small brick (lower part) using four fingers is demonstrated.

3.4.2 SMA Soft Hand on robot arm

To test the SMA Soft Hand in a robotic scenario, the hand is mounted at the end-effector flange of a UR5® collaborative robot arm. The robotic arm is programmed using the interface provided by the manufacturer, in order to reach the area where the object is positioned. At the same time, it is interfaced and synchronized with the microcontroller which drives the SMA Soft Hand.

In this way, once the robotic arm reaches the desired position, it enables the microcontroller to drive each hand finger according to a predetermined trajectory, and grasp the desired object. In order to ensure a successful performance, the SMA Soft Hand intelligence is deactivated until the robotic arm sends “an allowance signal” to the hand prototype. This means that, once the hand prototype is activated and the UR5 starts moving, the SMA hand will keep its activated status until the robotic arm does not send it the right signal.

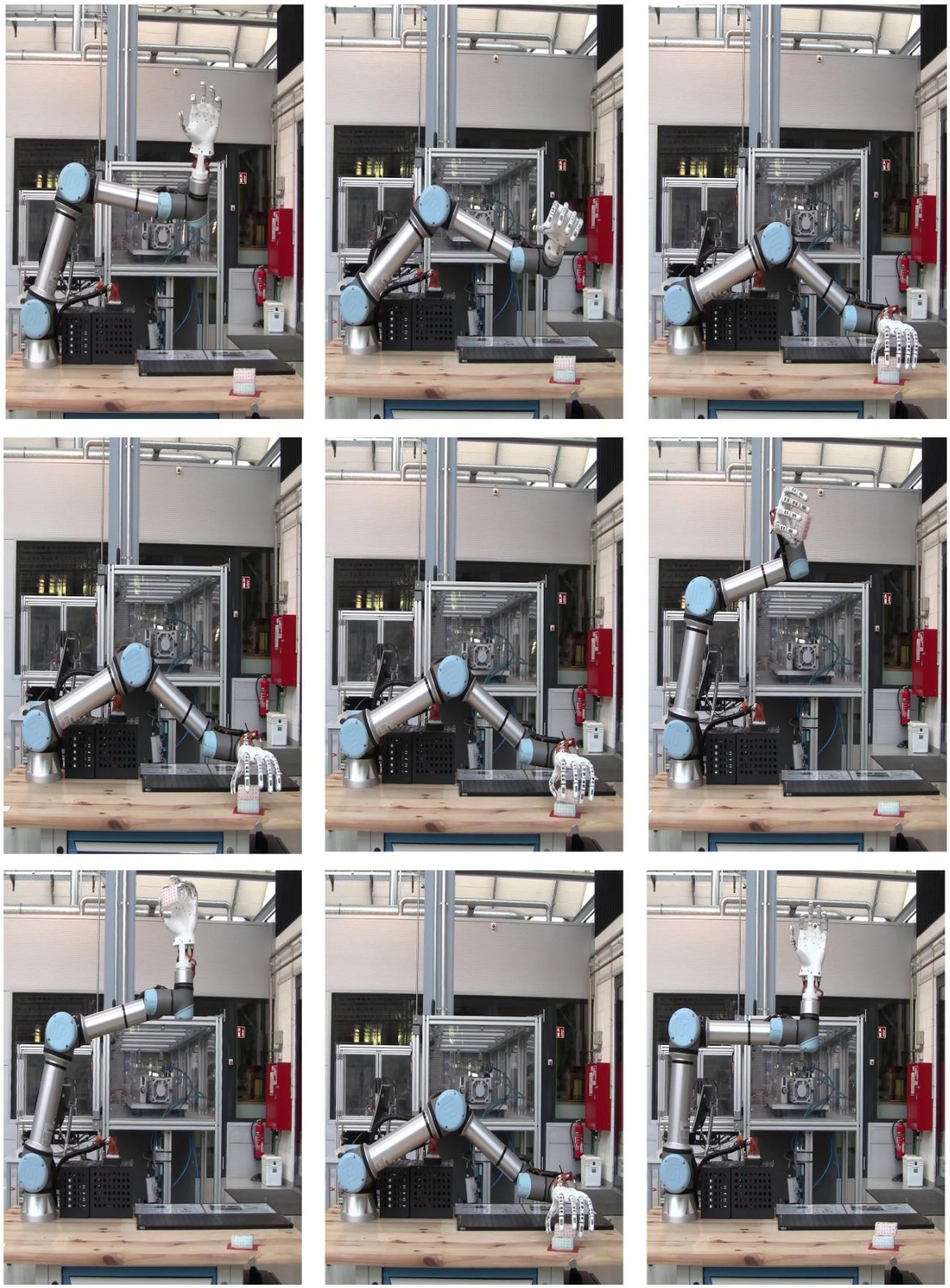

Figure 3.18: SMA Soft Hand grasping capabilities when used as end-effector of a robotic arm.

Hand Prosthesis Name	Weight [g]	Overall Size	DOF	Average Finger speed (°/s)	Average Grip Force (N)	Finger couplings	Structure
iLimb (2009)	600	180 mm long 80 mm wide 40 mm thick	6	~81.8	~68	Tendon linking MCP to PIP	Rigid
Bebionic (2011)	500	200 mm long 90 mm wide 50 mm thick	6	~ 96.4	~ 62	Linkage spanning MCP to PIP	Rigid
Michelangelo (2012)	420	Human hand size (no exact dimensions found)	6	~ 86.9	~70	Cam design with links to all fingers	Rigid
The smart Hand (2001)	530	Human hand size (no exact dimensions found)	16	~64	~40	Tendon/spring based	Rigid
UB Hand 3 (2005)	1000	Human hand size + 200 mm arm length	16	~250	~70	PIP and DIP coupled in ring, little, and thumb	Rigid
Pisa/IIT Soft Hand (2015)	500	230 mm long 235 mm wide 40 mm thick	19	~90	~15	Synergies: 1 DC motor for all DOF	Soft
SMA Soft Hand (2020)	300	200 mm long 116 mm wide 35 mm thick	14	~450 (high-speed activation)	~45 (estimated)	No couplings	Soft

Table 3.2: Performance benchmark composed by recently developed myoelectric robotic hands and the SMA Soft Hand

Once, then, the SMA Soft Hand is allowed to move, the UR5 will keep its position until the SMA hand will not communicate with the arm. Video sequences of the performed experiments can be seen in Figure 3.18. The experiment starts with the SMA Soft Hand deactivated and the UR5 enabled to move (Figure 3.18, first row). When the robotic arm reaches the predetermined grasping position (Figure 3.18, first row, right-hand side), it sends the "enable signal" to the SMA Soft Hand, in order to let the grasping process begin. In a first moment, all the fingers are stretched, to allow the handling of also big objects (Figure 3.18, second row, left-hand side). Then, the hand fingers move according to the control algorithm and grasp the dotted rectangular object (Figure 3.18, second row, central part). Once the desired object is grasped, the robotic arm is programmed to freely move in the air at different speed, demonstrating the effectiveness of the performed grasping. At the end, the robot arm regains the grasping position, allowing the SMA Soft Hand releasing the rectangular object (Figure 3.18, third row, central part).

3.4.3 SMA Soft Hand performances discussion

In the previous Sections, the SMA Soft Hand performances have been described in terms of force, displacement, and reactiveness. In order to better clarify the advantages of the developed prototype, a performance benchmark with a number of recently developed myoelectric robotic hands is presented in this Section. Pneumatic actuated prostheses are neglected from this comparative study, due to the structural disadvantage introduced by the technology (as discussed in the introduction Section). In Table 3.2, all the chosen hand prototypes are listed and compared in term of weight, size, DOFs, reactiveness, force, and structural complexity. In this table, the iLimb, the Bebionic, and the Michelangelo hands are chosen among all the commercially available prostheses. Among all the myoelectric prototypes designed by research groups in recent years, the SmartHand and the UB Hand 3 (having stiff joints), as well as the Pisa/IIT Soft Hand (with soft joints), represent the most performing ones.

In literature, the maximum weight of a human hand is quantified around 400 g [9]. In Table 3.2, only the Michelangelo and the SMA Soft Hand do not overcome this value.

In terms of dimensions, almost all of the prostheses are sufficiently similar to a real human hand. The UB hand 3 and the Smart hand represent the only exceptions, since they require a 200 mm long arm to hold the strings and electric motors which drive the fingers. Therefore, their use as prostheses for hand amputee presents some structural limitations. The DOFs of the commercially available hands are limited, since they combine the motion of the middle and of the bottom phalanx, keeping the tip phalanx fixed. The other prototypes, instead, offer up to 19 DOFs. The commercially available prostheses show similar performances in term of responsiveness and gripping force, with typical values of about 85-90 °/s and 65 N, respectively. These performances ensure good grasping and handling capabilities. The Smart Hand demonstrates sufficient fingers responsiveness (64

°/s), while, despite exhibiting smaller forces than the commercial prostheses (40 N), its grasping capabilities are sufficient to perform daily life operations. The UB Hand 3, on the other hand, shows even better than many commercial prototypes (70 N and 250°/s). Despite this fact, its large weight (1000 g) and dimension still represent its most critical downsides. Note also that all of the described prostheses have a stiff structure, which ensures robustness but also exposes the user also to possible involuntary damages. The use of soft prostheses helps the interaction between the user and the device, preventing potential injuries [99]. For this reason, soft prostheses are preferable to stiff devices. Among the many prototypes described in literature, the Pisa/IIT Soft Hand denotes good grasping capabilities, a compact structure, and good finger responsiveness. As for many soft robots [12], this prototype lacks in grasping force (15 N), thus preventing the possibility to handle several useful objects in daily life. The SMA Soft Hand ensures dimensions and number of DOFs comparable to the other prototypes in Table 3.2. It is able to achieve a high finger responsiveness using the high-speed activation method. The obtained grasping force is 3 times larger than the Pisa/IIT Soft Hand and, even if it is large enough to fulfil daily life operations, it is still far from the grasping force demonstrated by the commercial prostheses. Big advantages over the other hand prototypes are represented by its completely silent activation, its low weight (300 g), and its simple structure without transmission mechanisms which favors a lower price and a systematic assembling procedure.

3.5 Summary and Chapter conclusion

In this Chapter, a new design for a bioinspired SMA actuated hand prototype with soft features (SMA Soft Hand) has been presented. The described prototype can be used in biomedicine as a human prosthesis well suited for human-robot collaboration tasks. The modular finger structure uses superelastic SMA wires in the joint in order to enable soft features. These wires have been arranged according to a X-shaped pattern in order to avoid undesired joint configurations under induced lateral moments. Bundles of actuated SMA wires have been systematically manufactured using a welding method, in order to ensure an identical behavior of each wire in the same bundle. The use of SMA wires as actuators permits the design of a compact, lightweight, and silent hand device. A protagonist-antagonist configuration has been chosen for the SMA bundles, in order to enable higher prototype reactiveness. In addition, the modular structure permits a simple and fast replacement of possible damaged SMA actuator bundles, avoiding to replace the entire finger assembly.

Several tests have been performed in order to demonstrate the prototype capabilities. Force measurements have been realized at the finger top phalanx, while activating all the protagonist bundles in the finger. A force of about 9 N per finger has been evaluated, which leads to an overall hand prototype force of about 45 N. Such a value is within the range of human hand force. The complete motion of each finger phalanx has also been recorded,

showing also in this case values comparable with human fingers (45° for the tip phalanx, 90 ° for the middle and bottom phalanxes). Using a short pulse power excitation, a settling time between 0.2 s and 0.3 s has been observed for both rising and falling rotation phases. The described method can enable better performances if an adequate hardware is used. Objects with different sizes and shapes have been grasped by the SMA hand prototype, demonstrating its high gripping versatility.
In future works, the thumb mechanism will be improved by adding also adduction/abduction and opposition movements in order to increase the hand dexterity. Additional experiments will then be performed to evaluate the handling capabilities when dealing with various types of daily life objects and hand payloads.

Comparing the SMA Soft Hand with the concept developed in Chapter 2, it can be seen how the new prototype enables higher forces and responsiveness. A good dexterity has also been demonstrated thanks to the use of five independently actuated fingers, each one characterized by three active phalanxes. Moreover, it is possible to manufacture the SMA Soft Hand via an inexpensive and systematic procedure. All these aspects make, in principle, the SMA Soft Hand a device more suitable for the market than the first prototype developed in Chapter 2.
On the other hand, despite its many advantages, the SMA Soft Hand still has few drawbacks. First of all, the use of a high number of SMA bundles induces an increasing of the temperature of the overall prototype structure far above the human body temperature. This phenomenon still occurs even if the high speed activation method is adopted. This effect produces a deterioration of the SMA Soft Hand performances over the time, mostly in term of reactiveness. A further critical aspect, related to the placement of the SMA wires inside the prototype structure, is related to friction phenomena. When a SMA bundle is activated, it makes contact with the finger structure, generating undesired friction force. This effect has a negative impact on the prototype finger motion, reducing the reactiveness. Another important aspect is related to the possibility of scaling the prototype dimensions, in order to realize a device suitable for children as well. While the fist SMA Hand concept can be easily scaled down, mostly due to the small number of wires inside the structure and to its underactuated structure, the design of a smaller size SMA Soft Hand is in general more complex to achieve. This is mostly due to the high number of SMA bundles inside the structure, which are necessary in order to achieve the desired level of force. Determining the ideal arrangement and number of SMA wires which lead to the optimal trade-off between force, speed, and thermal effects requires, in general, more advanced design methods. Therefore, despite the obtained performance improvements, the SMA Soft Hand structure still needs further design optimization, by also including possible reconsiderations on some design solutions adopted in the first concept.
In order optimize the structure design and performances, it is important to better understand the physical interactions between the SMA wires and the hand structure with the support

of mathematical approaches. As previously analyzed, both designs are based on SMA bundles actuating rotating structures. The determination of the ideal arrangement and number of SMA wires represents a crucial aspect for the development of SMA actuated hands. Since the first hand concept has a simpler (yet very similar) structure than the SMA Soft Hand, mathematical models will be developed starting from the first generation of the SMA Hand discussed in Chapter 2.
Therefore, in Chapter 4, a model of this prototype will be implemented using finite element simulation tools. The model will be used to simulate the behavior of one hand finger varying geometrical quantities, (e.g., the distance of the wires to the rotation center), in order to allow not only future structural optimization, but also to solve the trade-off between force, responsiveness, and compactness.

Since to secure optimal performances, it is essential to develop adequate control strategies, beside the FE model, a lumped MATLAB model of the SMA finger will be formulated and described in Chapter 5.

4 Modeling for SMA Finger: FEM Framework

In this Chapter, we focus on finite element (FE) simulations of the robotic finger described in Chapter 2. As mentioned previously, several prototypes of prosthetic finger/hands actuated by SMA wires have been presented in recent years. Although SMA technology has shown good potential for prosthetic devices, none of the SMA hand prototypes presented in literature so far can be considered advanced enough to help amputees in real life situations. To effectively exploit SMA technology in prosthetic applications, the major challenges are represented by maximization of the motion range, achievement of large force in the prosthetic finger, and development of smart control algorithms to compensate the SMA nonlinearities. It is remarked how the development of accurate mathematical models, represents one of the fundamental steps towards the achievement of those goals. The models must be capable of describing the complex behavior of the SMA wires, the nonlinearities of the structure, as well as the coupling between the two. In particular, it is important to study the interaction between the SMA wires and the structure in which they are mounted. Such interaction is highly influenced by the mechanical contact between the wires and the structure, the thermal exchange between the SMA wires and the device, as well as the thermal exchange among the different wires in the bundle. All of these phenomena strongly affect the overall thermo-mechanical activation of the device, in terms of resulting bending, force, and speed.

To accurately describe the complex behavior of SMA actuated robotic fingers, in this Chapter we pursue an approach based on finite element (FE) modeling tools. In literature, several works focused on FE modeling of SMA wire inside structures [100]–[104]. On the other hand, only few works investigated modeling of SMA-actuated robotic fingers via finite element (FE) tools. One example is the work by El-Sheikh [105], in which the structure of a 4-fingered hand is simulated in Matlab®. The SMA wire is modeled as a pure force acting at the end of a passive tendon connected to the finger phalanxes, neglecting its dynamic behavior. Due to the highly complex behavior of both SMA material and hand structure, simulation tools for SMA-actuated prosthetic hands require a high amount of computational complexity, making practical modeling of these systems a challenging task. In this Chapter, a FE framework for modeling and simulation of SMA actuated prosthetic finger is presented. Due to high nonlinearity of the SMA model and to its complex interaction with the structure (i.e. contact phenomena), it is necessary, as first step, to focus on modeling and simulation of a single phalanx SMA-actuated finger. The purpose is to develop a model for the finger structure, which can be used for optimizing both structure geometry and SMA wires placement. The approach accounts for a fully coupled system, in which each SMA wire reacts to different power stimuli inducing a motion in the finger prototype, according to the system input.

The Chapter is organized as follows. First, a description of the finger prototype structure and its implementation in FE is exposed. Then, the implementation of the single crystal MAS model using FE is presented. Afterwards, two different Comsol® model implementations of the overall system are described, i.e., a standard approach (generally adopted in literature) and a new version, which is more computationally efficient. Parametric optimization and experimental validation are then carried out on the fully coupled model (SMA wire and mechanical structure). Then, the approach is extended and improved using the polycrystalline MAS model.

4.1 Finger Prototype Model

As remarked in the introduction, the aim of this Chapter is to introduce the implementation of a FE framework, which allows to describe the behavior of bundles of SMA wires placed inside a finger-like structure. As first step, we focus on modeling of a structure in which only a protagonist SMA wires is considered, working against an extension spring. A CAD model of such system is shown in Figure 4.1.

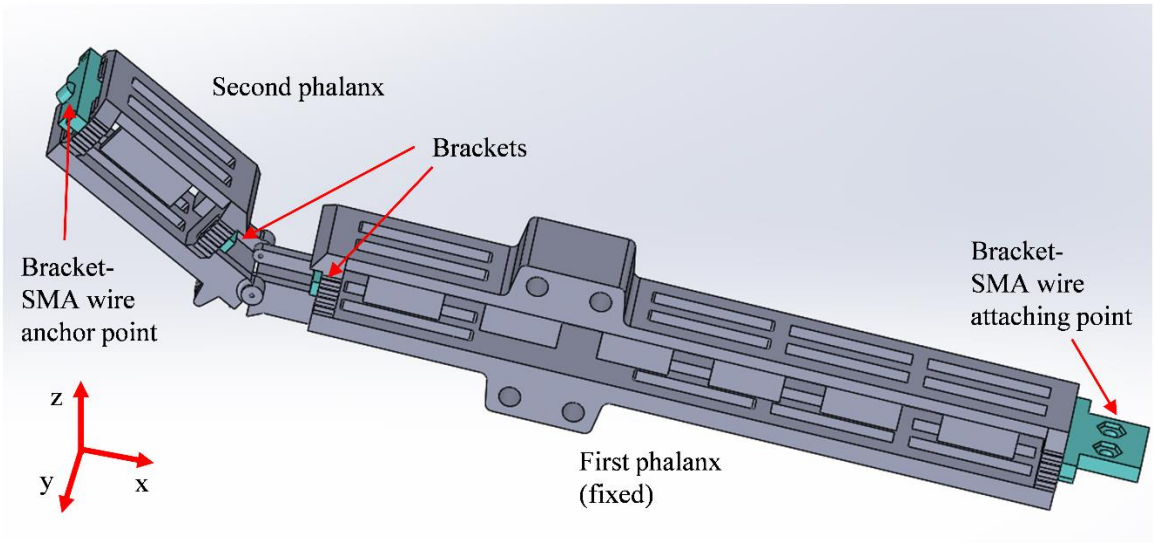

Figure 4.1: Finger CAD design

4.1.1 Finger Structure

The structure considered in this work is depicted in Figure 4.1 [83]. It consists of a two-components 3D printed finger. The first finger component represents the tip phalanx and is free to move, while the second one reproduces the other two phalanxes and the hand metacarpus and is fixed. Even if the prototype structure shape in Figure 4.1 differs from the

one of the SMA finger described in Chapter 2, their global dimensions are very close. The first phalanx length results from the sum of the middle, bottom and stand phalanxes lengths of the original SMA finger prototype.

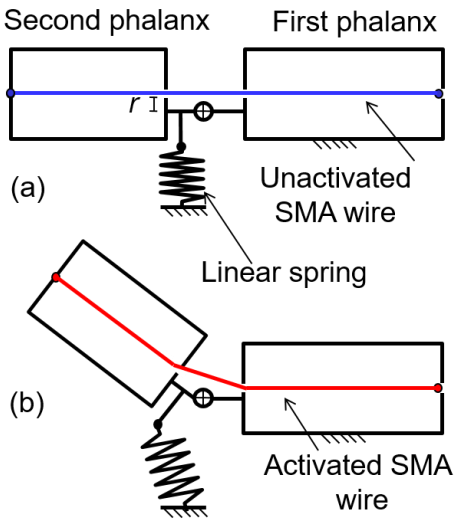

Figure 4.2: SMA finger actuator. (a) Unactuated configuration. (b) Actuated configuration.

These two elements are connected through a hinge joint [83]. To achieve actuation, a single 0.1 mm diameter SMA wire is placed inside the structure and its two ends fixed at the right site of the first phalanx [78]. In particular, the wire is inserted at the basis of the fist phalanx, guided all along the structure, routed around the second phalanx tip, and then guided back to the start point. In this way, a bundle of two wires mechanically in parallel is created. After inserting the wire in the structure, it is heated up with a 2 W DC power input (0.2 A and 10 V), in order to ensure a predominance of austenitic variants in its crystalline structure [95]. In this state, the wire is connected to a load cell, pulled until a small force is recorded, and then clamped [98]. This procedure ensures to achieve a reproducible SMA behavior, and to mount the wire under safe stress conditions in order to improve the lifetime [95]. Figure 4.2 (a) depicts the starting configuration, corresponding to unactuated SMA wire. When the SMA wire is activated, the second phalanx rotates, as shown in Figure 4.2 (b). If the current is removed from the wire, the spring restores the initial phalanx configuration in Figure 4.2 (a). To hold the wire inside the structure, some pierced brackets are realized and connected at the extreme points of each phalanx (depicted in green in Figure 4.1).

It is possible to move the pierced brackets along the phalanx short side, in order to vary the distance of the wire from the hinge joint center. This distance will be hereafter denoted as *r*. By varying *r*, the stroke/force conversion from wire contraction to finger rotation is modified. Therefore, it is of interest to investigate the effects of this parameter on the actuator performance. A saw tooth pattern is realized at the ends of each phalanx, in order

to ensure a precise positioning of the wire (see Figure 4.1). Each tooth has 1 mm of distance from its neighbor.

4.1.2 Finger Finite Element Model

The software COMSOL Multiphysics (COMSOL 5.2) is used to implement a model of the overall finger structure. To simulate coupled problem with large deformations, necessary to reproduce the finger behavior, the MultiBody Dynamics (MBD) module of COMSOL is used. Such a module permits to simulate displacement and rotations of rigid bodies, as well as systems of rigid bodies connected by joints. At the same time, user-defined differential equations can be implemented as constitutive relationships for specific elements. In order to achieve an accurate model of the structure, its 3D CAD file is directly imported in COMSOL through the use of the Cad Import Module. Since all of the prototype components are made of hard plastic, they are modelled as rigid bodies. A hinge joint connection is defined to allow rotation of the second phalanx, thus constraining its motion to a rotation around the y-axis (see Figure 4.1). A spring-damper connection is used to model the spring (see Figure 4.2), using a stiffness of 50 N/m and a pre-strain of 1 mm. As boundary conditions, a zero motion constrain is imposed to the first phalanx such as $u_x = u_y = u_z = 0$, where (ux, uy, uz) represent the finger displacement variables.

4.2 Single-crystal SMA wire model

To model the SMA material, the MAS model is chosen in this work [63]. This model is already described in detail in Chapter 1. In order to favor the text clarity, it is summarized in the following.

We recall that, the MAS model considers a mesoscopic lattice layer as basic SMA element. It is assumed that only two variants exist in the material crystal lattice, i.e., austenite A and one martensitic variants M_+, since the wire cannot sustain compressive stresses. To each variant, a phase fraction is associated. The following relationship holds among phase fractions

$$x_A + x_+ = 1, \tag{4.1}$$

where x_A, x_+ are the phase fraction associated to A and M_+ respectively. To describe the phase fraction kinetics, the following equations is used:

$$\frac{\partial x_+}{\partial t} = -p^{+A} x_+ + p^{A+} x_A, \tag{4.2}$$

where $p^{\alpha\beta}$ is the transition probability from phase α to phase β. Transition probabilities are derived via statistical thermodynamic considerations, and depend on both material stress σ and temperature T. They describe the probability for an ideal layer to overcome an energy

barrier in the non-convex free-energy landscape. The evolution of the temperature T in the SMA material is defined through the balance law of the internal energy, i.e.,

$$\rho c \frac{\partial T}{\partial t} = h \frac{\partial x_+}{\partial t} - \alpha_c S_v (T - T_0) + j(t), \tag{4.3}$$

where ρ is the material density, c is the specific heat, h is the latent heat of transformations, α_c is the heat transfer coefficient, S_v is the ratio between external surface and volume of the wire, and $j(t)$ is the volumetric density of Joule heating [64]. On the right-hand side of equation (4.3), the first term accounts for the rate-dependent heat generation and absorption due to the phase transformation, the second contribution represents the heat exchange between SMA and environment, and the last term represent the electric power density used as control input. Since in this work we are interested in the overall prototype behavior, we can neglect the local phenomena in the SMA material and assume that the temperature is homogeneous along the wire. For this reason, the equations (4.2) and (4.3) can be expressed as distributed ODEs in the COMSOL model. On the one hand, this simplification permits to describe the SMA wire behavior in terms of an average temperature only, rather than via a distribution of temperature. This permits to significantly reduce computation time of our FE simulations. Transition probabilities also depend on transformation stresses of austenitic and martensitic phases, given as follows

$$\sigma_A = \sigma_L + \frac{d\sigma}{dT}\left(T - T_L\right), \tag{4.4}$$

$$\sigma_M = \sigma_A - \Delta\sigma, \tag{4.5}$$

where σ_L is the transformation stress from martensite to austenite at reference temperature T_L, $d\sigma/dT$ is the gradient transformation stress with respect to the temperature, $\Delta\sigma$ is expressed as σ_A-σ_M and represents the hysteresis width.

To implement the SMA mechanical dynamics in COMSOL, the momentum balance formulation is typically adopted [102]. However, for implementing the mechanical coupling between SMA wire and finger structure, this formulation appears as unsuitable. To address this issue, in this work the constitutive SMA equations are implemented via a truss element. The truss is an element which can sustain only axial load, and therefore can effectively represent the behavior of the one-dimensional SMA model. In addition, implementation via the truss element makes the coupling between SMA and external systems simpler to achieve. The constitutive equation for the truss stress is defined in COMSOL as

$$\sigma_t = \sigma_{ti} + E\left(\frac{du}{dx} - \varepsilon_{inel}\right), \tag{4.6}$$

where σ_{ti} is the initial truss stress, E is the truss Young's modulus, du/dx is the truss strain, and ε_{inel} the truss inelastic strain. For the MAS model, the SMA stress is defined as follows [63]

$$\sigma = \frac{\varepsilon - \varepsilon_T x_+}{\frac{x_+}{E_M} + \frac{(1-x_+)}{E_A}}, \tag{4.7}$$

where ε is the SMA strain, ε_T is the transformation strain, and E_A and E_M are the austenite and martensite Young's moduli, respectively. In order to relate the truss element to the SMA model, we have to impose that the truss stress σ_t equals the SMA stress σ. This can be done by defining the following quantities

$$\sigma_{ti} = 0, \tag{4.8}$$

$$E = \frac{1}{\frac{x_+}{E_M} + \frac{(1-x_+)}{E_A}}, \tag{4.9}$$

$$\frac{du}{dx} = \varepsilon, \tag{4.10}$$

$$\varepsilon_{inel} = \varepsilon_T x_+ . \tag{4.11}$$

Moreover, in order to couple the SMA mechanical behavior with the phase fraction dynamics and the temperature evolution, it is possible to define ODEs (4.2) and (4.3) along the truss node.

4.3 Complete Model Implementation

During the finger assembly, the SMA wire is first inserted in the structure, by driving it inside the phalanxes using the bracket holes, and then clamped. During the actuation, the wire contracts and slides inside the brackets holes, making the second phalanx bend. In previous works dealing with SMA modeling, the material and the structure are usually described as a unique rigid element, thus neglecting any relative motion between the two [106], [107]. By using this approach, the coupling between wire and structure is easily established through integration methods [107]. In this work, on the other hand, in order to accurately describe the finger actuation the sliding motion of the wire inside the structure has to be modeled. To the authors' best knowledge, no standard method exists in the COMSOL interface to efficiently couple a truss to a 3D solid body, and, at the same time, to allow any relative motion between the two [108]. Possible implementation solutions are discussed in the following.

4.3.1 Standard approach

By considering the SMA wire as an 'active cable', it is possible to model it as a combination between a 3D solid cable (representing the solid nature of the wire) and a truss (representing

the SMA constitutive behavior). This modeling solution enables the use of embedded features of the MBD module to constrain the motion of the cable inside the phalanxes. In order to implement such a hybrid element, a 3D solid cylinder having same length and diameter of the SMA wire is considered. This element is finely meshed using tetrahedral elements, according to a standard meshing procedure embedded in COMSOL. All the nodes of the cylinder mesh lying on a line are then assigned to be the SMA truss, on which the modeling approach discussed in Section 4.2 is implemented. In this way, the truss element is linked with the 3D elastic solid element such that $(u_t,v_t,w_t) = (u_c,v_c,w_c)$, where (u_t,v_t,w_t) are the degrees of freedom (DOF) of the truss element, while (u_c,v_c,w_c) are the DOF of the solid element.

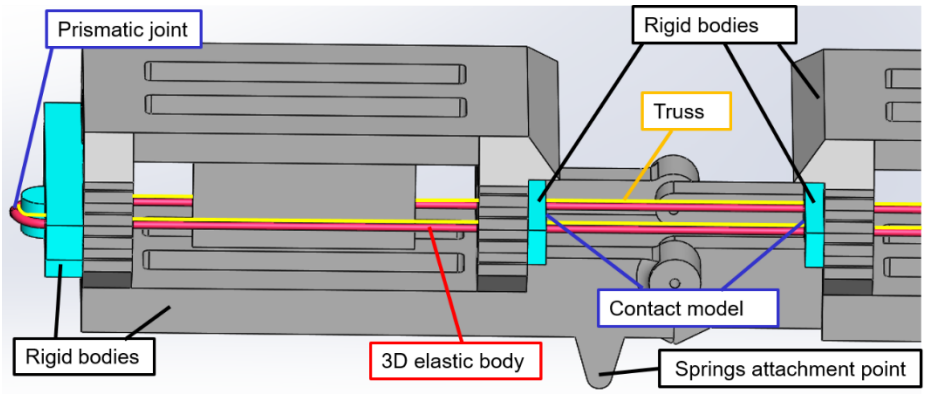

Figure 4.3: Finger prototype drawing. The SMA wire truss is depicted in yellow, while the 3D solid element in red

This is shown in Figure 4.3, in which the SMA wire truss is depicted in yellow, while the 3D solid element is depicted in red. In this way, the cylinder is rigidly connected to the truss, absolving a mere passive function. In order to constrain the hybrid element inside the two phalanxes, a zero displacement boundary condition is imposed at the two endpoints. In this way, the wire clamping mechanism can be modeled. To let the wire follow the phalanx motion while contracting, a prismatic joint connection is imposed at its routing point, situated at the second phalanx tip (Figure 4.3).This embedded feature of the COMSOL MBD module also enables to rigidly connect the two elements with respect to any user-defined motion frame. As initial condition for the SMA model, the wire is assumed in a fully martensitic state, such as $x_+ = 1$ and $x_A = 0$, while the starting temperature is set equal to the environmental temperature, such as $T_0 = T_E = 295$ K. To demonstrate the efficiency of the proposed modeling approach, a joule heating input signal having a trapezoidal profile is imposed to the SMA wire. The resulting simulation (Figure 4.4) shows that the boundary conditions of the hybrid element hold on both wire endpoints and on its routing point. On the other hand, the wire body penetrates the phalanxes structure without sliding along the finger brackets. In order to avoid this effect and properly model the real system behavior, considerations based on the system behavior are performed. In particular, by observing the experimental response of the device, it can be noted that as soon as the SMA is actuated it

interacts with the finger structure only at the boundaries. After a slight rotation of the second phalanx, both wires make contact with the brackets closer to the hinge joint. Therefore, during contraction, the wires start sliding along the prototype structure. According to the literature [109], [110], to implement contact issues among 3D wires and structures, embedded features in FE software based on Augmented Lagrangian or Penalty methods are commonly used. Following the same strategy, contact features are imposed among the hybrid element and the two brackets, and the results are shown in Figure 4.4 (lower part). As it can be observed, by imposing these conditions the model behaves as expected.

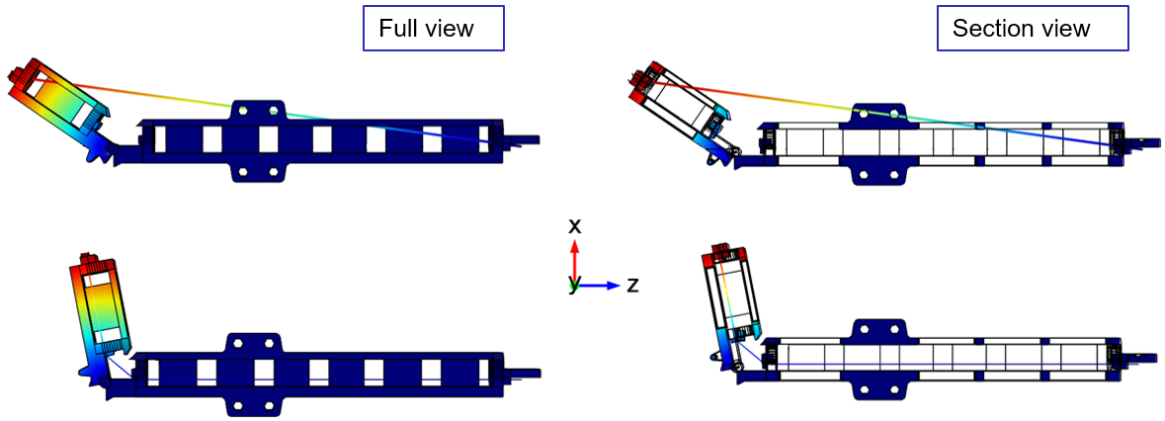

Figure 4.4: Complete model simulation (upper part) without part) with the implementation of the contact between the wire and the structure. (Left-hand side) Full view. (Right-hand side) Section views, which highlights the wire behavior.

On the other hand, this choice makes the computation time significantly higher. By performing the simulation on a PC with an Intel® Core i7 4790 processor having clock frequency of 3.60 GHz and RAM of 32 GB, and using the poorest mesh solved by COMSOL (a 'coarse' mesh for the rigid bodies and a 'finer' one for the hybrid element), the average computation time is 5 hours for a full 90° phalanx rotation. Since the structure investigated in this work represents a simplified version of the real system, which involves many phalanxes and fingers at the same time, this modelling approach appears as unsuitable for engineering simulations of the complete device. In order to reduce the simulation time while achieving accurate results, a new modelling approach is proposed in the following Section.

4.3.2 Novel approach

Due to the high computational demand of state-of-the-art methods for implementing the contact between SMA and structure, a new strategy is proposed in this Section. The novel approach is based on the following observation. The truss element represents a very efficient method to describe a general wire and, at the same time, ensures an easy coupling

with the one-dimensional SMA model equations (ODEs). In order to use this representation, despite the modeling limitation of COMSOL Multiphysics, hybrid elements obtained from the combination of a truss element (related to the SMA model equation) and a 3D solid element can be considered. On the other hand, it is possible to note that the truss element does not need to interact with the rigid structure in every point, but only at the wire routing point and along the contact areas. For this reason, the truss element representing the SMA wire is linked with small 3D solid elements having a cylindrical shape only in the areas where it needs to interact with the structure. We obtain that $(u_t,v_t,w_t) = (u_c,v_c,w_c)$, where (u_t,v_t,w_t) are the degrees of freedom (DOF) of the truss element, while (u_c,v_c,w_c) are the DOF of the solid element.

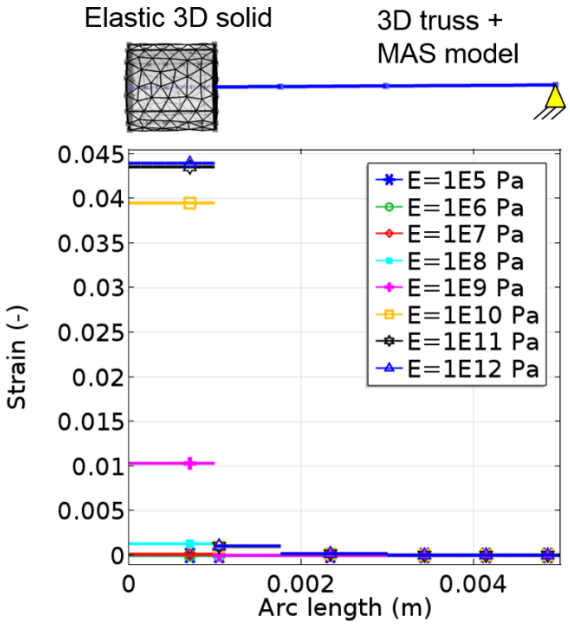

Figure 4.5: Analysis of the effect of the Young's modulus *E* on the 3D element deformation, used to couple the SMA wire with the 3D structure

A problem of the above method concerns with the value of the Young's modulus which has to be assigned to the 3D element and the 3D element length. In order to assign the best value of Young's modulus *E*, a simple simulation involving only one SMA truss and a 3D element is performed by varying the stiffness of the 3D element. In this simulation, the truss is designed in such a way it coincides with the cylinder longitudinal axis. A ramp-shaped joule heating input signal is used to activate the wire, initially in fully martensitic phase. Subsequently, the amount of wire contraction during the simulation is acquired, and the result is shown in Figure 4.5. It can be noted that for high values of *E* the truss portion inside the 3D solid does not contract. If *E* is gradually decreased, the solid stiffness has a smaller impact on the wire dynamic. For values of $E < 10^8$ Pa, the influence of the solid element on the truss behavior is minimized and thus the SMA truss is able to contract along its entire length. In order to have a better idea of this behavior, let us observe Figure 4.6. In this picture, the simulation of a SMA truss connected to a 3D cylinder is depicted, in

analogy with Figure 4.5. At the left-hand side, the inactivated system, having the SMA wire in detwinned martensitic phase, is shown. On the other side, the actuated system is depicted, showing, in the center part, the system deformation and, in the right-hand side, the Von Mises stresses. In this picture, the displacement and deformation induced by the SMA wire along the cylinder horizontal axis, which represents the region of points of the cylinder mesh nodes united with the SMA truss mesh nodes, are depicted. The SMA wire portion outside the cylinder, while contracting, produces a motion along the y-axis (Figure 4.6, center part), which is directly induced on every point of the cylinder mesh. This is transduced in a cylinder horizontal motion according to the SMA dynamics. On the other hand, also the portion inside the cylinder contracts. This effect influences only the cylinder mesh points united with the truss. Therefore, the deformation magnified in Figure 4.6, center part, is induced.

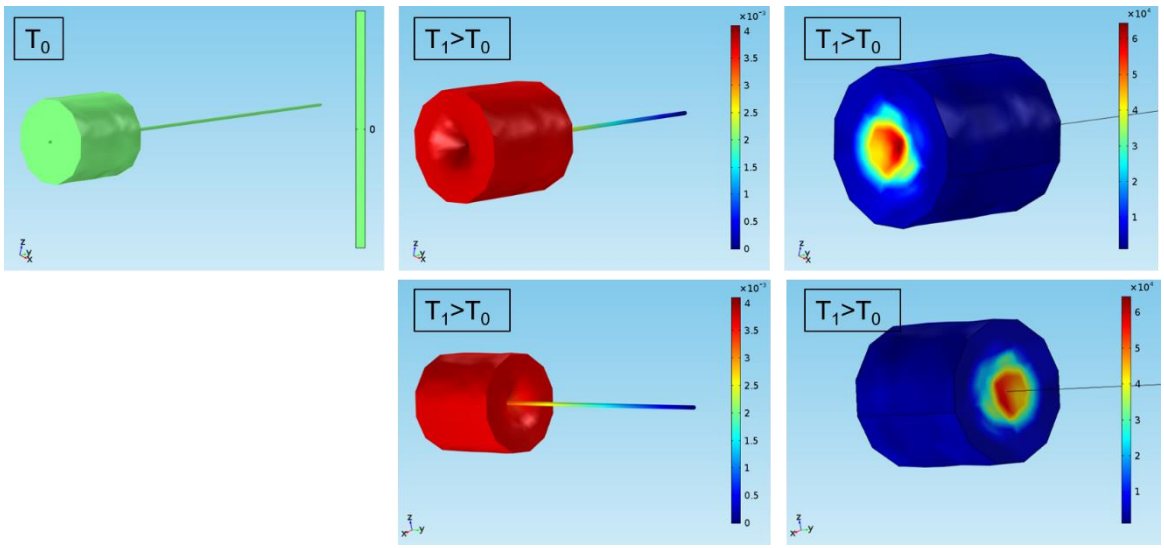

Figure 4.6: Deformation and stresses induced by the SMA wire truss on the 3D cylinder in case of $E < 10^8$. (Left hand side) Unactuated system. (Center part) Displacement and (right hand side) Von Mises stresses for the fully actuated system.

According to the obtained results, two different descriptions can be used to model the 3D cylinder. The first possibility is to model it as very short stiff elastic element ($E > 10^{10}$ Pa), in order to minimize the truss portion inside the cylinder which does not contract. The second solution is to describe the 3D cylinder as longer soft elastic element ($E < 10^8$ Pa), which allows the truss portion inside to fully contract.

For this model, both approaches have been considered. For the wire parts which interact with the finger structure without any contact, the first approach has been adopted since the use of stiff elements usually leads to smooth solution convergence. For the other case, the second approach has been implemented since it ensures a more physical representation. The wire parts belonging to the first category are the ones fixed to the second phalanx tip. To simplify the implementation of this last part, the wire part routed around the anchor point is omitted from the model since, due to the high friction in that point and to its limited length, it provides a negligible contribution to the overall material strain. For this reason,

one stiff 3D cylinder element, having the same diameter of the SMA wires used in the real prototype and a small length, is coupled with the truss at the second phalanx tip and fixed. This is shown in Figure 4.7, in which the SMA wire is depicted in red, while the 3D solid element is depicted in yellow. In this way, the cylinder is rigidly connected to the truss, playing a merely passive role. To couple the 3D cylinder with the second phalanx, a prismatic joint connection is established (feature of the MBD module), defining a zero relative displacement between the two. To model the SMA bundle, a truss element (linked to the relative passive solid elements) is defined for each branch of the bundle itself. In this case, two trusses and two stiff cylindrical solid elements, one for each truss, are defined. Both trusses are then fixed at the right endpoint of the first phalanx, with a zero displacement condition at the correspondent trusses nodes ($u^i_t=0$).The wire parts belonging to the second category are the ones close to the hinge joint, which make contact with the finger brackets as shown in Figure 4.7.

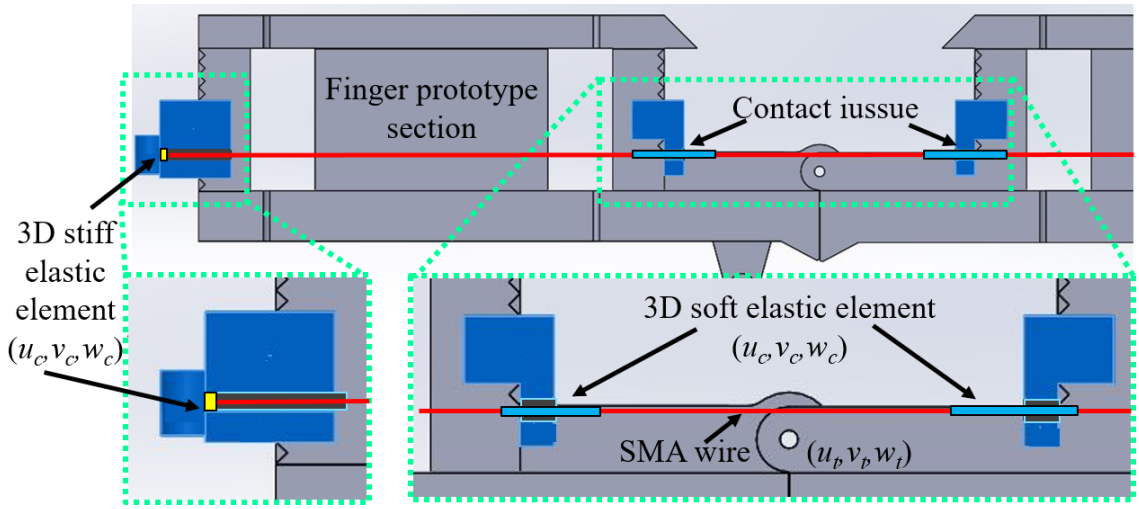

Figure 4.7: Finger prototype Section drawing. The SMA wire is depicted in red, the 3D stiff elastic element used to build the prismatic joint is represented in yellow, while the 3D soft elastic elements used to address the contact issues is depicted in cyan.

In theory, the first approach (use of thin 3D stiff solid element coupled with a truss) could have been considered, arranged as shown in Figure 4.8(left-hand side), and used to establish contact with the brackets. However, when contact occurs, this topology leads to a bad convergence of the solver, mainly due to discontinuities which appear when the contact surface meets the edges of the element. In order to improve the convergence, a single soft 3D elastic element is considered, having enough length to ensure contact during the entire bending process (Figure 4.8, right-end side). By choosing a small enough Young's modulus for this element, it is possible to have a full contraction of the SMA truss even inside the 3D element, as shown in Figure 4.5. To implement the contact issue between the 3D solid and both finger brackets, a COMSOL embedded feature to implement contact is used.

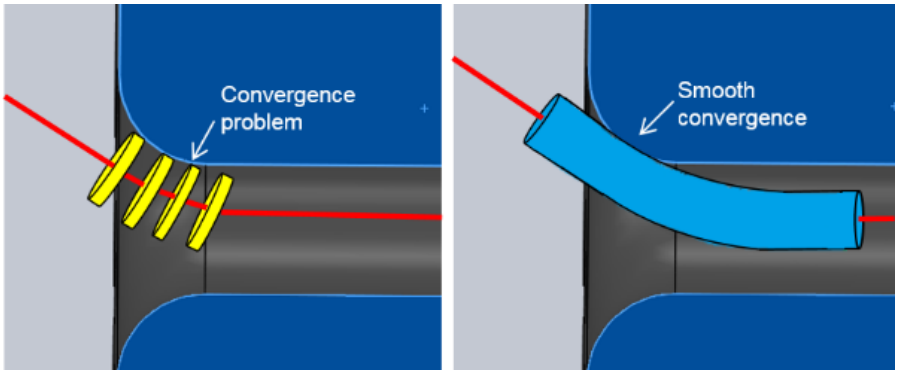

Figure 4.8: Contact models. (Left-hand side) The use of 3D small stiff elements leads to solver convergency problems. (Right-hand side) The use of a 3D soft elastic element helps the model to achieve a smooth convergence.

The penalty method is selected for the contact resolution, using as penalty factor the identified values of the martensitic Young modulus. Using these parameters, once the contact between the wire and the brackets is established, the wire starts sliding along the brackets profile (Figure 4.8, right-end side) until the SMA phase transformations is over. Simulations performed on a PC with an Intel® Core i7 4790 processor having clock frequency of 3.60 GHz and RAM of 32 GB, and using a 'coarse' mesh both for the rigid bodies and for the hybrid element, results in an average computation time of 90 minutes. This simulation time accounts for a full phalanx rotation, induced by an on/off activation of the SMA wires.

4.4 Experiments and parameter identification: single- crystal MAS model

4.4.1 Experiments

In this Section, some experiments are presented in order to perform identification of the SMA model. The experiments consist of applying input different power profiles for different wire attachment points, while measuring the resulting rotation angle as output. We remark that activation of SMAs produces an increase of temperature, a resulting phase transformation, and a change of geometry. All these effects result in an overall change of electrical resistance. Therefore, if the actuator is controlled by means of a current supply, the resulting input power j will change during actuation. Power is directly related to temperature, as it can be observed from equation (1.4), and therefore it represents a more suitable control input than the current. To address this issue and to allow controlling the SMA power directly, a power control is implemented. To generate the desired input power signal, a Pulse Width Modulation (PWM) method is implemented (see [94] for details). The power controller is programmed with LabVIEW 2012, and loaded on a National Instruments cRIO-9074 real-time data acquisition system. A NI-9472 constant DC voltage

source, i.e., a digital switch able to supply up to 30 volts with a switch time of 100 μs, is used to supply a 10 V peak PWM signal. In order to evaluate the true power absorbed by the SMA, current (NI-9227) and voltage (NI-9229) measurement modules are connected respectively in series and in parallel to the finger prototype. Before each experiment, current and voltage are acquired while the switch is activated for 500 μs, in order to evaluate the maximum power for each wire. At this stage, desired power profiles are generated by a host desktop computer running LabVIEW, and then sent to the FPGA. The host also stores the measured values of voltage, current, resistance, and power for each experiment. During the acquisitions, the FPGA uses the difference between desired ad maximum powers to compute the duty cycles. The calculated duty cycles are, then, used to generate the 100 Hz PWM signals, which control the NI-9472 switches.

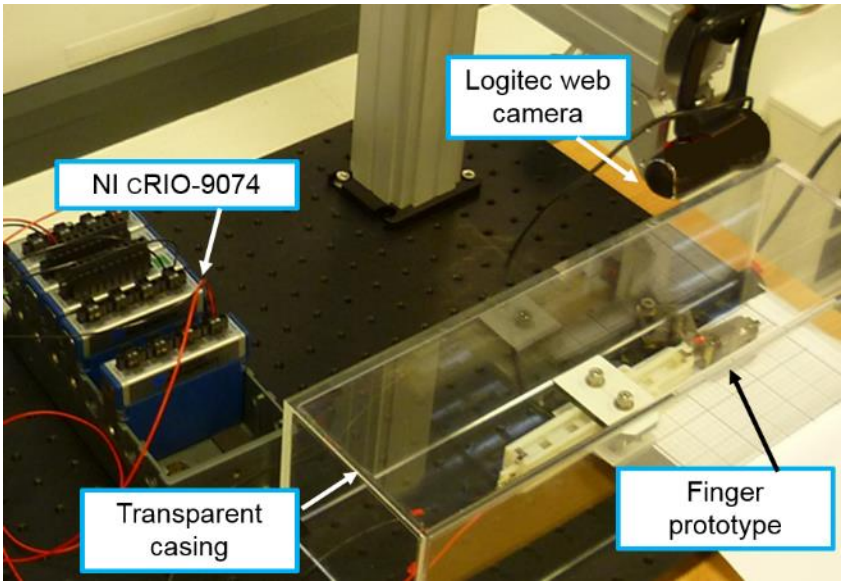

Figure 4.9: Setup used to measure the finger prototype angular displacement using different power stimuli.

At the same time, the host is interfaced with a Logitech web camera, positioned perpendicularly to the finger phalanxes, which collects the video frame at 30 frame per second.

Prior to start the measurements, a thermo-mechanical training is conducted to stabilize the wire behavior. This training is performed by applying the trapezoidal power profile several times, until a repeatable bending motion is achieved [111].

At the beginning of each experiment, the finger is in its fully straight configuration. The applied input power follows a trapezoidal profile. During the trapezoid rising front, the second phalanx starts to move. When the power starts to decrease again, the finger phalanx regains its initial configuration thanks to the restoring spring force. This experiment is repeated for different input powers and for all the possible wire distances from the second

phalanx center of rotation, according to the available bracket positions along the sawtooth profile.

Model Variables			
Model Variable Name	**Symbol**	**Value**	**Unit**
Modulus of austenite	E_A	40	GPa
Modulus of martensite	E_M	20	GPa
Transf. strain	ε_T	0.038	-
Width of stress-strain hysteresis	$\Delta\sigma$	52	MPa
Austenitic transf. stress at temperature T_L	σ_L	403	MPa
Gradient transf. stress respect to the temperature	$d\sigma/dT$	7	MPa/K
Reference temperature	T_L	383	K
Specific heat	c	500	J/kg
Heat convection coefficient	α	220	W/m^2K
Latent heat of phase transf.	h	25	kJ/kg

Table 4.1: Optimized Model Parameter

Increasing r leads to a reduction of the SMA wire level arm, with a resulting increase in moment and decrease in bending angle.
The video acquired during the experiments is post-processed using functions embedded in the Matlab *Image Processing Toolbox*, based on the gradient variation. The algorithm permits to track position of some points of interest, and therefore to reconstruct the bending angle.

4.4.2 Parameter Identification and Validation

As previously discussed, a single crystal model has been adopted to model the SMA wire behavior. In [65], it is highlighted how the use of this model represents a good but imperfect representation of the real SMA behavior. Moreover, due to the assumption of a homogeneous temperature field along the wire, an additional error is introduced in the simulations.
Together with these main aspects, we have also to consider that, when a SMA wire is embedded in a system, it undergoes a thermo-mechanical training that modifies its behavior, i.e., its hysteresis [112], [113]. This training effect also occurs when a pre-trained SMA wire is embedded in a new application. Therefore, every time a SMA wire is mounted in a novel system, we expect its hysteresis to change accordingly.
For these reasons, in order to maximize the model fidelity, a parametric identification must be performed on the complete system, i.e., finger and SMA wire coupled together. The identification aims at finding the parameters set which make simulated and measured bending angles as close as possible, for the specific application under consideration.

In the model previously described, there are 10 unknown material parameters, i.e., E_A, E_M, ε_T, σ_L, T_L, $\Delta\sigma$, $d\sigma/dT$, α, c, and h.

In principle, reference values for some of these parameters are known from literature or reported on the material supplier datasheet [78]. However, by accounting for the training effects discussed above, and by also considering that a single-crystal SMA model is being used to describe a real-life polycrystalline wire, a fine tuning of few parameters is still required in order to reproduce the experiments with a sufficient fidelity. We point out, however, that such a parametric optimization must be guided by physical insights as close as possible, in order not to affect consistency of the model.

Considering r = 1.5 mm and maximum power of 2 W (corresponding to the configuration which produces the larger phalanx rotation), a quasi-static test is used for the calibration procedure. In this experiment, the finger is actuated with a trapezoidal Joule heating profile having a period of 67 s. Due to the relatively slow actuation, it is possible to neglect the effects of some thermal parameters (i.e., c and h), thus reducing the number of parameters to be optimized from this calibration experiment. From (4.3), we deduce that under quasi-static conditions the temperature is proportional to the applied power by a factor which depends on α. The feasible range of variation for this parameter is then selected in such a way that, for a given maximum Joule heating, the wire temperature reaches a physically reasonable value, i.e., between 370-400 K according to the datasheet [95].

In addition, $d\sigma/dT$ assigned to a fixed value of 7 MPa/K, which is a commonly used value for NiTi SMA [114]. Once $d\sigma/dT$ is known and T is given, from (4.4), we see that there are infinite combinations of T_L and σ_L which produce the same σ_A for a given T. For this reason, T_L is arbitrarily fixed to 383 K, while only σ_L is optimized. In addition, despite austenite and martensite Young's moduli E_A and E_M are in principle known, we point out that in the MAS model such parameters truly represent the slopes of the leftmost/rightmost lines in the stress-strain hysteresis curve. Since the single-crystal MAS model is here used to reproduce a real-life SMA wire, for which it is hard to determine whether or not these lines correspond to a fully transformed material, these parameters are included in the parameter optimization as well. From simulation studies, it can be noted that variations of ε_T and E_M produce similar effects on the system displacement. Therefore, to further reduce the number of parameters to optimize, we can assign a fixed value to E_M = 20 GPa. As a result of the previous considerations, the set of free parameters to be optimized with the first experiment is reduced to E_A ,ε_T, σ_L, $\Delta\sigma$, α. In order to properly determine the range of variation of these parameters to use in the optimization algorithm, a parameter study has been realized varying manually each parameter within physically consistent limits [65]. The results obtained for a selected number of parameters, i.e., $\Delta\sigma$, α, and σ_L, are shown in Figure 4.10 to Figure 4.12. In those figures, the SMA stress-strain hysteresis and the corresponding angle-power hysteresis of the complete actuator (reported on the left-hand sand right-hand sides of the figures, respectively) are shown.

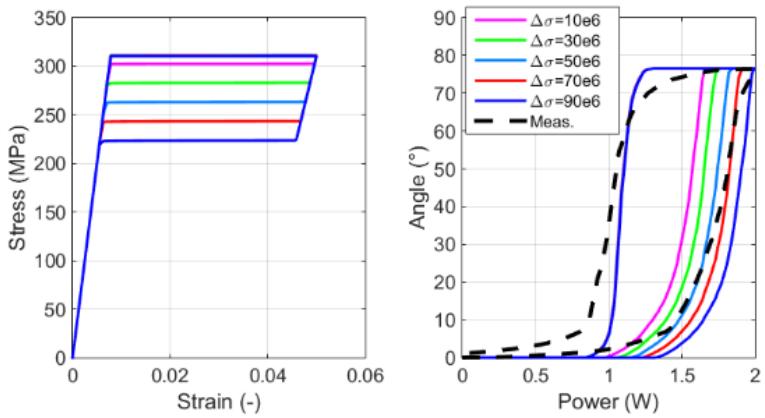

Figure 4.10: Parametric study for Δσ [Pa]. (Right-hand side) Angle-power diagrams. (Left-hand side) Stress-strain diagram.

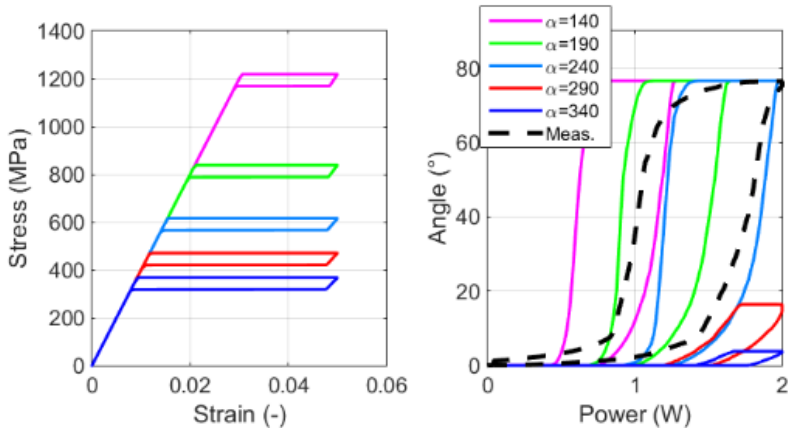

Figure 4.11: Parametric study for α [W/m^{2}K]. (Right-hand side) Angle-power diagrams. (Left-hand side) Stress-strain diagram.

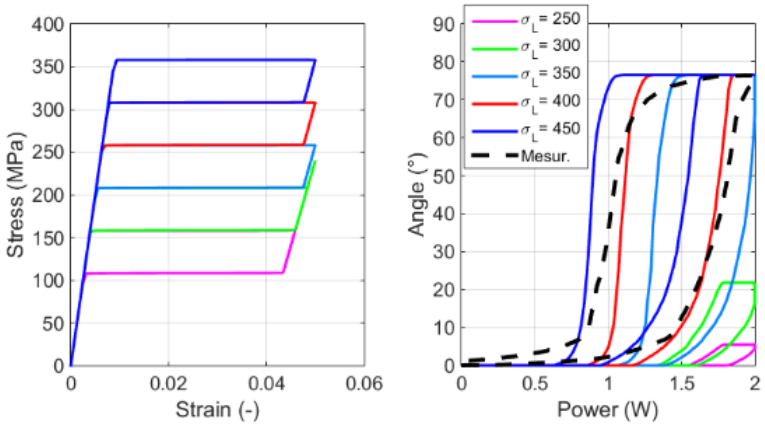

Figure 4.12: Parametric study for σ_L [Pa]. (Right-hand side) Angle-power diagrams. (Left-hand side) Stress-strain diagram.

The curves are obtained by varying each parameter at time while keeping the other ones constant. The diagrams related to the variation of E_A and ε_T are omitted, since their effects

on the input-output characteristics are negligible in our range of interest. Starting from the Figure 4.10, the effect of the parameter $\Delta\sigma$ is highlighted. On the right-hand side, it can be observed how the hysteresis width decreases for higher values of $\Delta\sigma$. This means that for small value of $\Delta\sigma$, less joule heating will be necessary to achieve a full rotation of the phalanx while, when increasing $\Delta\sigma$, more energy will be needed to achieve the full contraction of the SMA wire and thus a complete motion of the prototype. By decreasing the value of $\Delta\sigma$ the hysteresis lower plateau rises, while the value of the upper plateau remains constant, thus provoking a change in the hysteresis width. This effect can be also observed from its corresponding stress-strain diagram in the left-hand side.

In Figure 4.11, the effects of α are shown. While increasing this parameter, the angle-power hysteresis is shifted towards the right-hand side. This means that for lower values of α the transformation temperature is lower, therefore the phase transformation occurs at a smaller temperature. By increasing α, the transformation temperature increases and thus a higher input power will be needed to complete the phase transformation. Observing the stress-strain diagram, for large values of α the stress at 370 K is lower than the one for small values of this parameter, and thus also the transformation stress. In Figure 4.12, the effects of variations of σ_L are displayed.

By increasing σ_L, the angle-power hysteresis is shifted to the left, while decreasing the parameter value the curve is shifted to the opposite side. This means that for lower values of σ_L the transformation temperature increases and thus also the input power needed to fully transform the SMA wire. In the stress-strain diagram, increasing σ_L makes the hysteresis move upward, while degreasing it results into a downward shift. In practical terms, this means that for higher values of σ_L the transformation stress increases. Using the previous analysis, the variation ranges are selected for each parameter as follows: $E_A \in$ [40, 60] GPa, $\Delta\sigma \in$ [30, 90] MPa, $\sigma_L \in$[350, 450] MPa, $\alpha \in$[200 240] W/m^{2}K. The optimization procedure is implemented in COMSOL using the Optimization module, which finds acceptable values for the model variables by minimizing a user-defined objective function. In this case, a least-square objective function is chosen, which computes the mean squared error between the simulated angle (variable of the model) and the measured one. The solution method known as Coordinate Search is chosen, a gradient-free solver suited to explore the solution space without returning values related to local minima [108]. The initial values used at the beginning of the optimization process are reported in Table 4.1, and are based on experiments performed in previous works [65]. A number of 100 maximum iterations is imposed to the solver, while a satisfactory convergence is obtained in a smaller number of iterations. Each simulation is performed on a PC with an Intel® Core i7 4790 processor having clock frequency of 3.60 GHz and RAM of 32 GB. At the beginning of each experiment, the finger is in its fully stretched position at room temperature (295 K), and the SMA is not activated. In this configuration, the angle is zero.

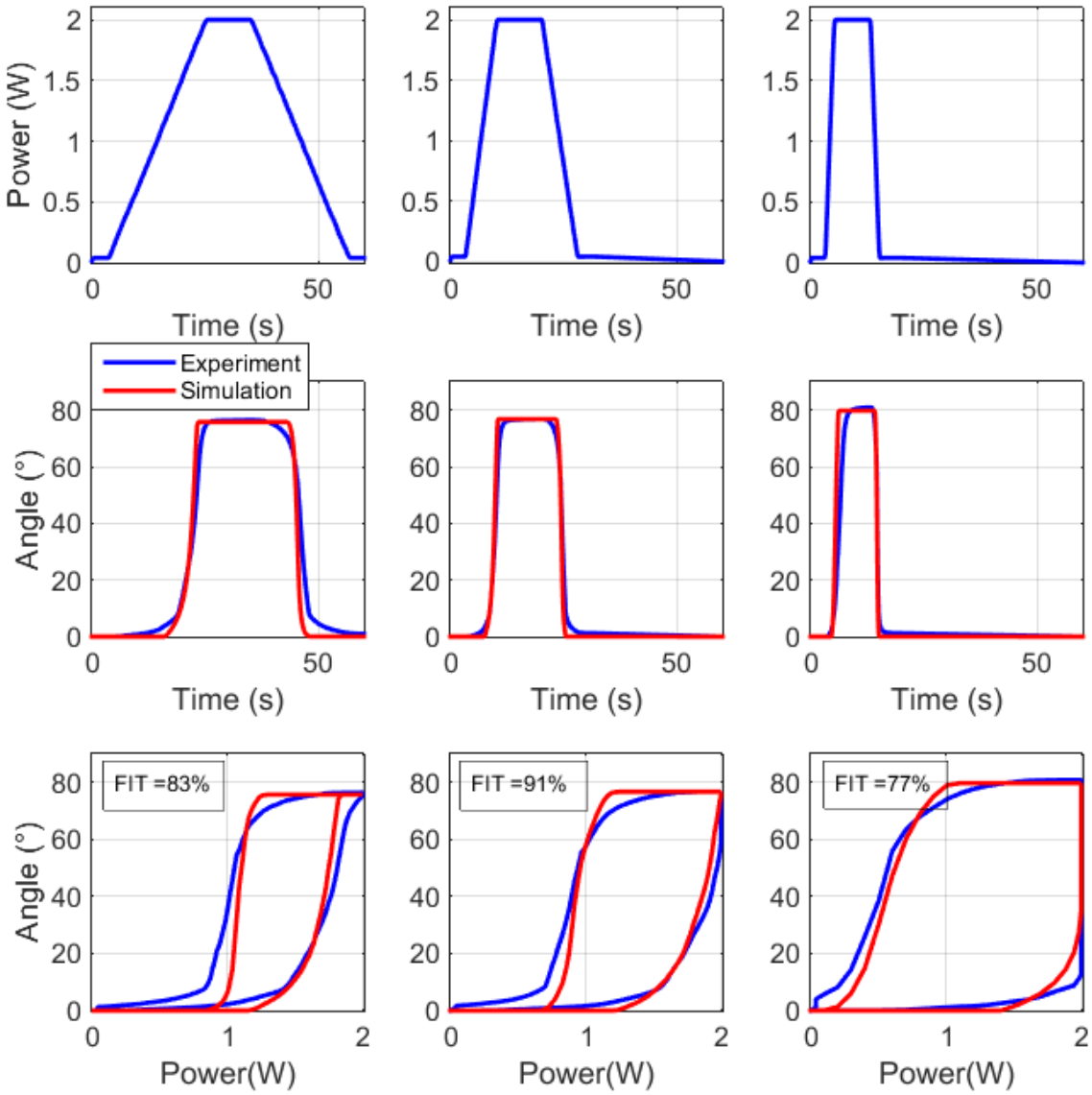

Figure 4.13: Model calibration experiment, r = 1.5 mm, step power signal at different frequencies Experiment (blue line), simulation (red line).

At t = 3 s, the PWM controller starts to supply an increasing power profile to the wire, which generates a rotation of the phalanx. The resulting power stays then constant until t = 35 s. Then, the power starts to decrease in order to let the finger restore its original position. The duration of the increasing/decreasing ramps of each power signal equal 32 s. The system input power and the resulting angle-power hysteresis obtained for the optimal parameters are shown in Figure 4.13, first column. The optimized parameters are reported in Table 4.1. It can be noted that the fit between measured and the identified hysteresis is overall good. Nevertheless, the two curves deviate in many points, since the single crystal model adopted for the SMA material represents only an approximation of the real SMA behavior. To achieve a better model accuracy, a polycrystalline extension of this model could be used [115], at the expense of a higher computational complexity. Nevertheless,

the level of accuracy observed in Figure 4.13 is still satisfactory. Finally, to tune and validate the value of *c* and *h*, the device has been activated using a faster input power signal. The considered signals have a total duration of 30 s and 15 s, and are shown in Figure 4.13, upper part, second and third columns, respectively. In the same figure, lower part, a good agreement between the measured and simulated SMA finger motion behavior can be observed.

In order to quantify the accuracy of the simulation results, a FIT has been calculated according to the following expression

$$FIT = 100\left(1 - \frac{\left\|\theta - \hat{\theta}\right\|}{\left\|\theta - mean(\theta)\right\|}\right) \tag{4.12}$$

where θ is the measured rotation, $\hat{\theta}$ is the simulated rotation, and $\|\theta\|$ denotes the 2-norm of θ.

This value shows a good accuracy of the simulated model, which ranges from 77% (faster input) to 91% (intermediate input), as reported in Figure 4.13. After parametric identification, model validation is performed by considering experiments obtained for different values of input power and distance between the SMA wires to the joint center. In Figure 4.14, the comparison between simulation and experimental results is shown for several validation tests. In here, the experimental and simulated trends obtained by varying *r*, for 1.5 mm, 3.5 mm and 5.5 mm, are reported.

These experiments are realized for two different power levels (1.4W and 2W) in order to verify the bending angle dependence from the input power. By comparing all the obtained trends, it is possible to observe a satisfactory agreement in both the bending and the transient motion behavior. In Figure 4.14, dynamic responses of wire strain, phase fraction, and temperature are also shown. Note that in some cases (2 W input) the wire displacement follows the Joule heating in a quasi-static way, while for other cases (1.4 W input) we have a dynamic response which results into a slightly delayed activation. The model is capable of capturing this phenomenon with a satisfactory accuracy. In particular, it can be observed that the sharper behavior is obtained in correspondence of a full transformation into austenite, while the exponential convergence is more evident for a partial transformation. In addition, it can be observed how the use of the single-crystal SMA model introduces a sharper transient behavior for the angle, which is more evident in the first and last parts of the rising and falling fronts of the signals. The calculated FIT for r = 1.5 mm, 3.5 mm, and 5.5 mm are 86%, 89%, and 83%, respectively. In all the tests, the simulations show an error in predicting the maximum bending angle value, due to an intrinsic limitation of the adopted single-crystal model. Using this kind of model, it is not possible to accurately represent the prototype behavior for power level or for radii ranging between those considered. This effect, caused by the sharp single-crystal model, can be also observed by inspecting the hysteresis in Figure 4.13. The simulations results also highlight a relationship between the prototype maximum rotation angle and the wire distance from the rotation center. The

minimum considered value of *r* appears still too large to achieve a full 90° rotation of the prototype phalanx. To achieve a complete phalanx motion and, at the same time, sufficient actuation force, a higher number of windings in the SMA bundle have to be considered for future prototypes.

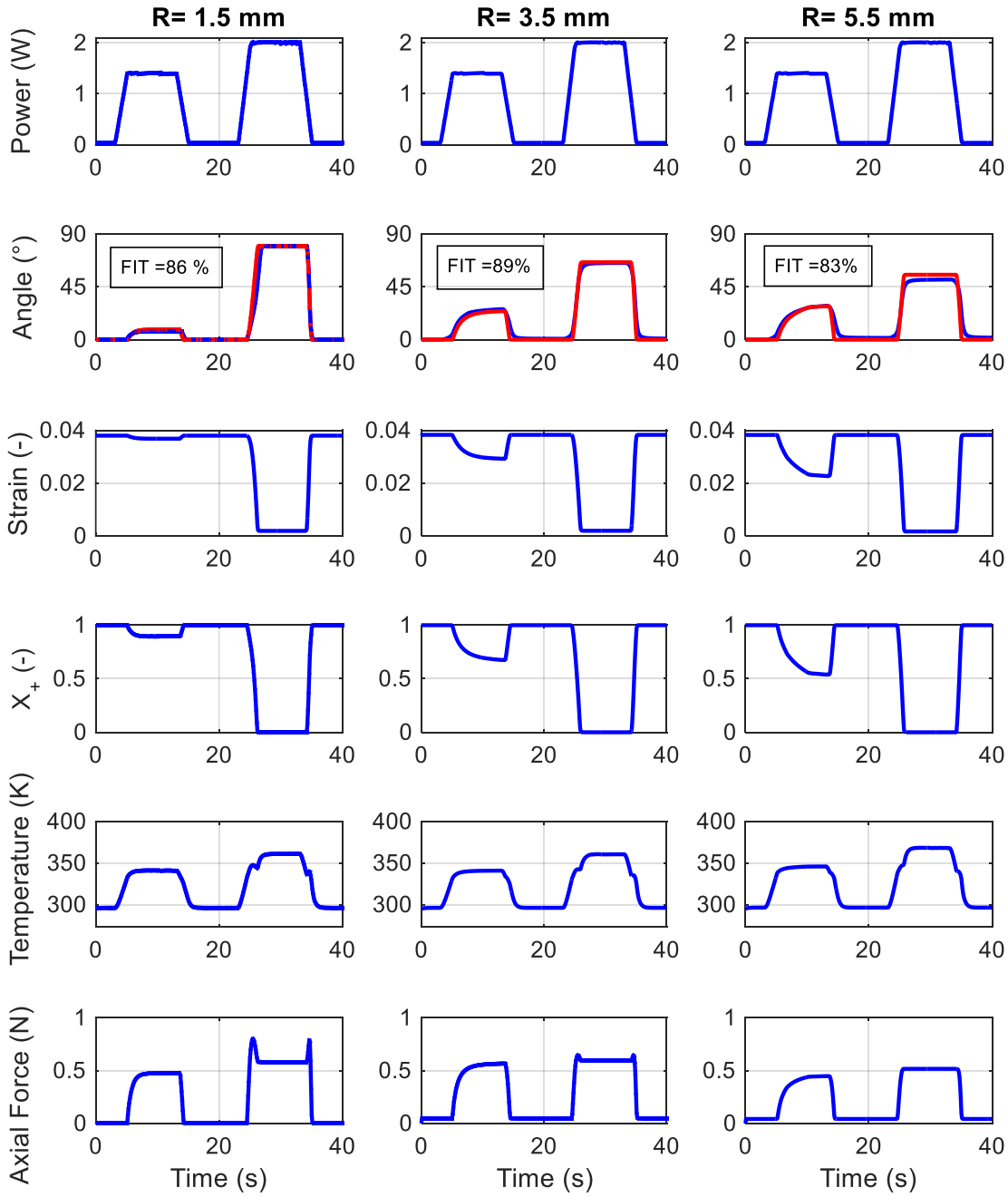

Figure 4.14: Model validation experiments, *r* = 1.5, 3.5, 5.5 mm, trapezoidal power signal at 1.4, 2 W. For each *r*, wire strain, phase fraction and temperature are displayed. Experiment (blue line), simulation (red line).

4.5 Poly-crystal SMA wire model

In the previous Section, the simulation results obtained using the single-crystal MAS model, have been presented. Due to intrinsic limitations introduced by using the single-crystal MAS model, the simulation results, obtained by using different values of *r*, show an insufficient agreement with the experimental behavior. Moreover, the prototype motion in response at intermediate values of input power is also not accurately predictable. In order to overcome these limitations, the polycrystalline extension of the MAS model is introduced in the overall prototype model [62]. This model extension has been previously described in Chapter 1, but, for more clarity, it is briefly summarized in the following.

In equations (1.2) and (1.3), we have defined the transition probabilities which mostly depends on the austenitic transformation stress σ_A and martensitic transformation stress σ_M. In the single-crystal model, these quantities are defined as linear functions of temperature in (4.4) and (4.5).

In [62], to parametrize SMA polycrystallinity, it is assumed that the transformation stresses not only depend on temperature, but also on the current material composition, i.e., the phase fractions. In addition, we point out that we are dealing with wire geometries, which cannot sustain compressive stresses, and thus results that $x_- = 0$. Under these assumptions, the transformation stresses of the polycrystalline SMA model are defined as follows:

$$\sigma_A(T, x_+) = \sigma_A(T_L, x_+) + \sigma_S(x_+)(T - T_L), \tag{4.13}$$

$$\sigma_M(T, x_+) = \sigma_M(T_L, x_+) + \sigma_S(x_+)(T - T_L). \tag{4.14}$$

Functions $\sigma_A(T_L,x_+)$ and $\sigma_M(T_L,x_+)$ describe the transformation stresses at reference temperature T_L, while the thermal scaling is accounted by the term proportional to $\sigma_S(x_+)$. This approach permits to represent a smooth, polycrystalline hysteresis in a computationally efficient way. By assuming $x_- = 0$ and $k = 0$, and also by considering (1.1) , (4.13) and (4.14), equations (1.2), (1.4) and (4.7) can be rewritten as follows:

$$\frac{\partial x_+}{\partial t} = -p^{+A}(\sigma, x_+, T)x_+ + p^{A+}(\sigma, x_+, T)(1 - x_+), \tag{4.15}$$

$$\rho c \frac{\partial T}{\partial t} = h \frac{\partial x_+}{\partial t} - \alpha_c S_v (T - T_0) + j(t), \tag{4.16}$$

$$\sigma = \frac{\varepsilon - \varepsilon_T x_+}{\frac{x_+}{E_M} + \frac{1 - x_+}{E_A}}, \tag{4.17}$$

Equations (4.15) - (4.17) completely describe the polycrystalline SMA model. We point out, however, that the presented approach permits to accurately describe the outer hysteresis loop only. In order to also predict internal hysteresis loops with great high accuracy, a bookkeeping algorithm has to be implemented [62]. Implementation of such a bookkeeping method makes the model significantly more demanding on the computational viewpoint, and therefore it is omitted from this work.

4.6 Parameter identification: polycrystalline MAS model

The identification process aims at finding the best parameters values, which make measured and simulated bending angle as close as possible, for a specific calibration experiment. The experiments considered are the ones collected during the campaign described in Section 4.4.1. To simplify the identification, a two-step procedure is adopted. As a first step, single-crystal model parameters are identified. Based on the single-crystal parameters, proper functions for σ_A, σ_M, σ_S as a function of x_+ are then characterized, allowing a polycrystalline extension of the model. This two-step procedure permits to simplify the overall process, since a smaller number of parameters has to be identified at each step.

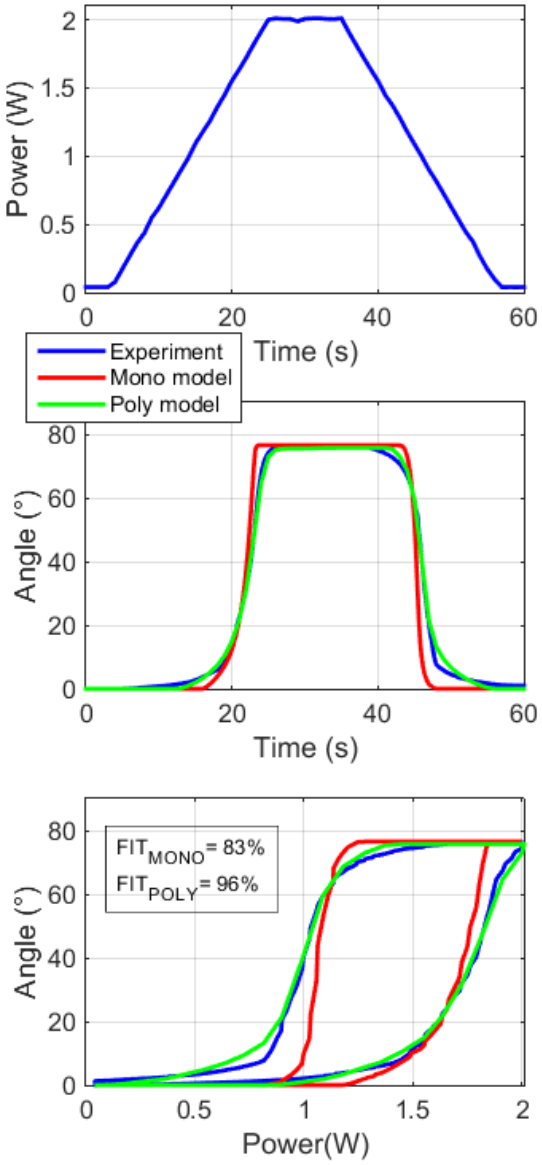

Figure 4.15: Comparison between the real and the simulated system behavior using the mono- and the polycrystalline model approximation.

The obtained single crystal parameters are used as a starting point for the calculation of the polycrystalline hysteresis as described in [115], [116]. This means that the same values of E_A, E_M, ε_T, T_L, α, c, and h obtained for the single-crystal model are used as initial parameters for the identification routine (Table 4.1). In addition, $\sigma_S(x_+)$ is chosen as constant, and equals to the corresponding single-crystal value. Therefore, the only parameters which have to be identified are the scaling curves at reference temperature $\sigma_A(x_+,T_L)$ and $\sigma_M(x_+,T_L)$. These curves are implemented via standard interpolation methods, based on sigmoid. The weights of every sigmoid are the solution of a least-square objective function, which computes the mean squared error between the simulated angle (variable of the model) and the measured one.The solution method known as Coordinate Search is chosen, a gradient-free solver suited to explore the solution space without returning values related to local minima [108]. For further information about the sigmoid mathematical expression and weights calculations, refer to [62]. As for the identification procedure used to obtain the single crystal parameter, quasi-static experiments are, at first, taken in consideration. By supplying the SMA wires according to a power profile having a long period, it is possible to induce a quite slow actuation of the finger prototype. This permits to neglect the effects of some thermal parameters (i.e., c and h), thus reducing the number of parameters to be optimized from this calibration experiment.

The system input power, the resulting angle-time characteristic and angle-power hysteresis obtained for the optimal parameters are shown in Figure 4.15. In this picture, a comparison between the simulated behavior obtained using the mono- and polycrystalline model version is shown. Even if both model versions guarantee a good approximation of the real system behavior, the polycrystalline model ensures higher adherence at both low and high power values. This enables higher accuracy in estimating small rotations of the finger phalanx. In Figure 4.16, the experiments used to calibrate α, c and h are presented. These parameters give a bigger contribution to the system behavior when the finger structure is activated at higher frequencies. In these situations, indeed, the thermal phenomena have more influence in the system behavior.

In Figure 4.17, the performances of the polycrystalline model using different power level as input for r=1.5 mm are displayed. Aside to the high adherence between real system and the simulations, it is possible to notice how the simulations show a smooth behavior, without sharp edges (in contrast to the monocrystalline simulations shown in Figure 4.14). This new model extension enables a successful prediction of the phalanx motion when the finger prototype is activated using different power input signals (Figure 4.17). We remind that, using the monocrystalline model version, an accurate prediction of the system behavior related to intermediate input power levels is not possible.

At the bottom of Figure 4.17, the SMA axial force evaluated at the middle of the wire is presented. The picture shows an increasing SMA force, as soon as the finger phalanx starts rotating from its stretched position (Figure 4.18, 1), and then, when a rotation angle of 45°

is reached, a decreasing force trend (Figure 4.18, 2-3). If a general SMA- liner spring system is considered (Figure 2.6), the SMA force increases as soon as the wire is actuated.

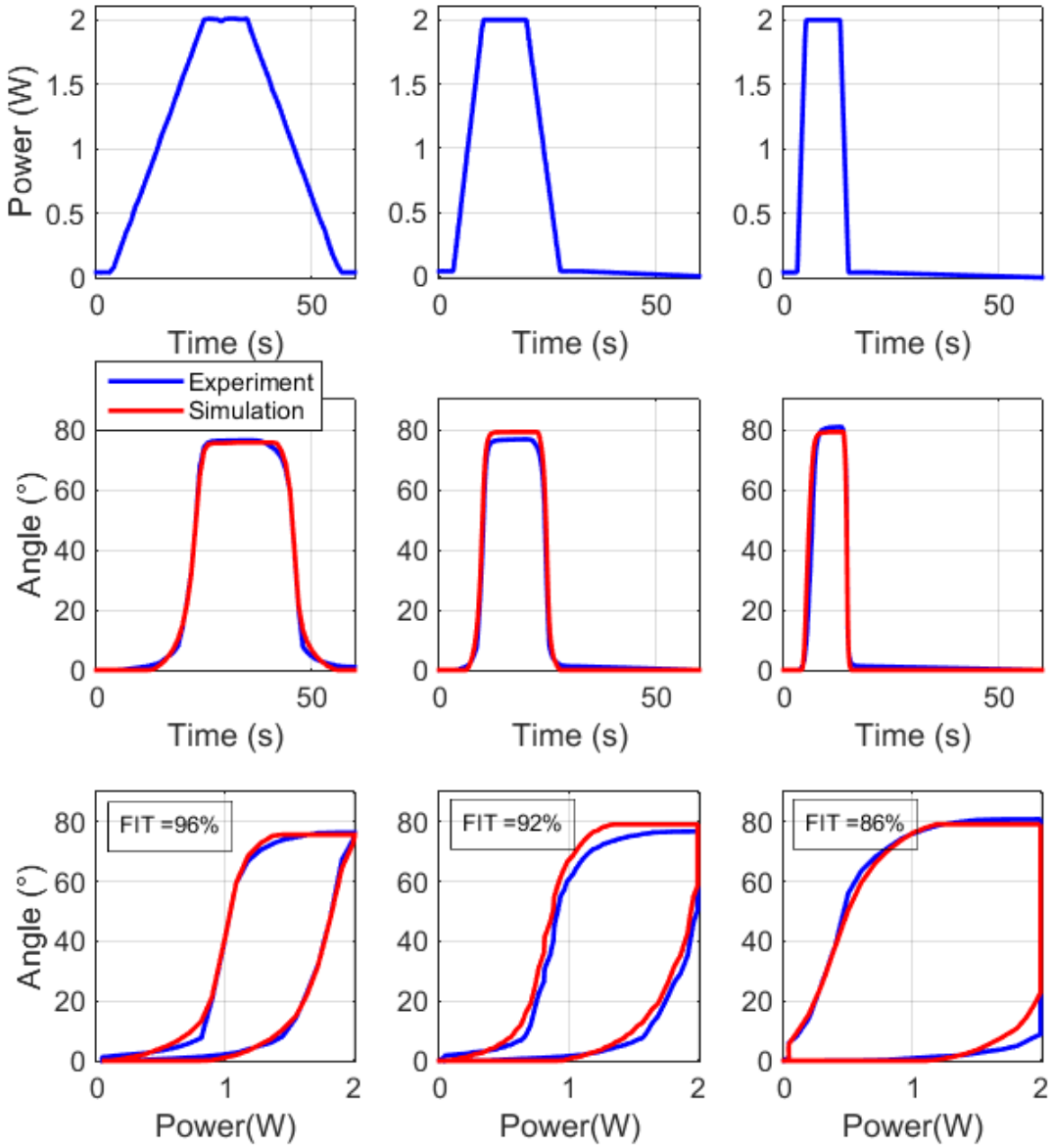

Figure 4.16: Model calibration experiments for the polycrystalline SMA model, r = 1.5 mm, step power signal at different frequencies. Experiment (blue line), simulation (red line).

In the finger structure, the linear spring has one end fixed and the other connected to the upper phalanx in the point P. Therefore, when the SMA wires are powered, this point rotates according to Figure 4.18, left- hand side. Let us consider the horizontal coordinate of P. When the SMA wires are not actuated, this point has the horizontal coordinate z_1 (Figure 4.18 (1)). As soon as the system is powered and the phalanx starts rotating, the horizontal coordinate of P changes in z_2 (Figure 4.18, (2)), where $z_2 < z_1$. This leads to a force increase and thus to $F_{z2} > F_{z1}$. When the phalanx rotation angle reaches a value bigger than 45°, the horizontal coordinate of P will start increasing (Figure 4.18, (3)), and thus, $z_3 > z_2$, which

leads to $F_{z3} < F_{z2}$. According to this effect, during the first half of the experiment, the horizontal component of the spring force shows a not monotonic behavior.

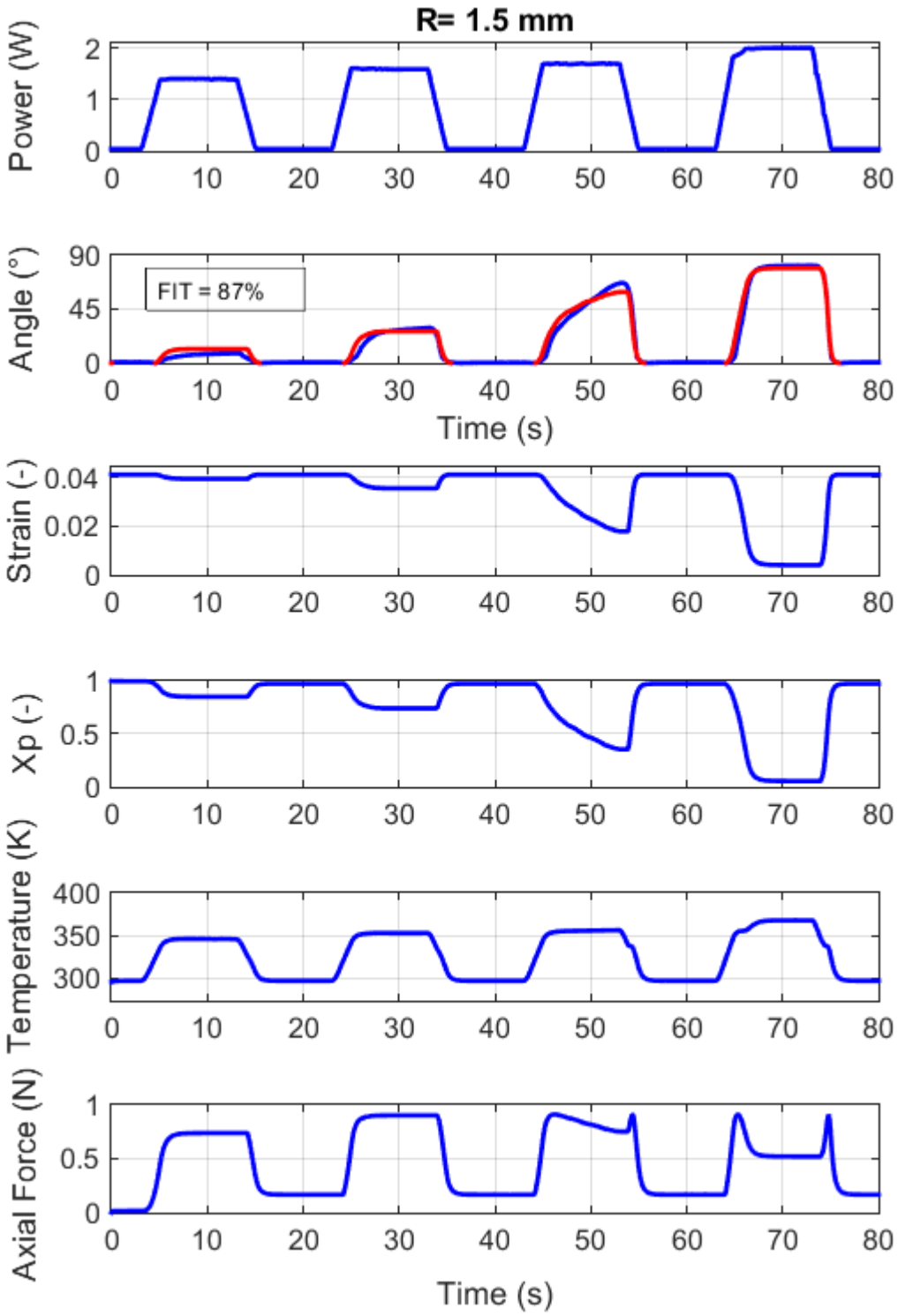

Figure 4.17: Model validation experiments, *r* = 1.5 mm, trapezoidal power signal at 1.4, 1.6, 1.8 and 2 W. Wire strain, phase fraction and temperature are displayed. Experiment (blue line), simulation (red line).

Since the system motion depends on the interaction between the SMA and spring moment, the spring not monotonic behavior is directly reflected in the SMA force (Figure 4.17).
From the results depicted in Figure 4.17, we can notice that a complete rotation of the finger phalanx is never achieved. Using a 2W input power, indeed, the SMA strain stabilizes around 0.01.

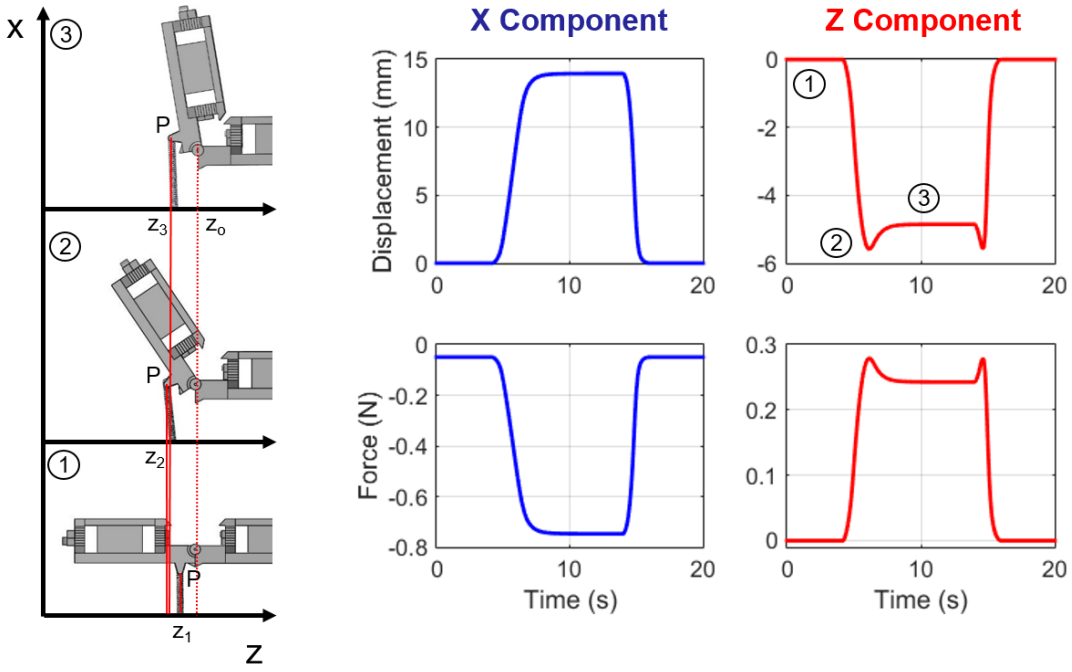

Figure 4.18: Spring force and displacement evaluated at the spring attaching point.

This means that the SMA wires are long enough to enable a 90° rotation of the prototype phalanx, but do not exert sufficient force to entirely overcome the influence of the linear spring. Increasing *r* or the number of SMA wires arranged in parallel could lead to a resolution of this issue. In Figure 4.19, the achieved rotation varying the SMA wires distance *r* and the input power level is shown. From this picture, it is noticeable that, increasing *r*, the maximum performed rotation angle decreases. This result is strictly connected to the structure geometry, since, as soon as *r* increases, the SMA strain required to achieve a desired motion increases.
Therefore, the design of the parameter *r* results challenging, since it is important to ensure enough bending moment to enable a full rotation of the prototype phalanx together with a contained SMA wires length.
A satisfactory adherence is obtained also varying the value of *r*, ranging from 1.5 to 5.5 mm, at different power levels, as shown in Figure 4.19. While the model is able to well capture the transient branches of displacement profiles, small deviations are visible between the simulated and measured angle heights reached for each power input and value of *r*. This disagreement could be due to intrinsic limitations of the adopted model, since, as previously described, internal loops are not well captured.

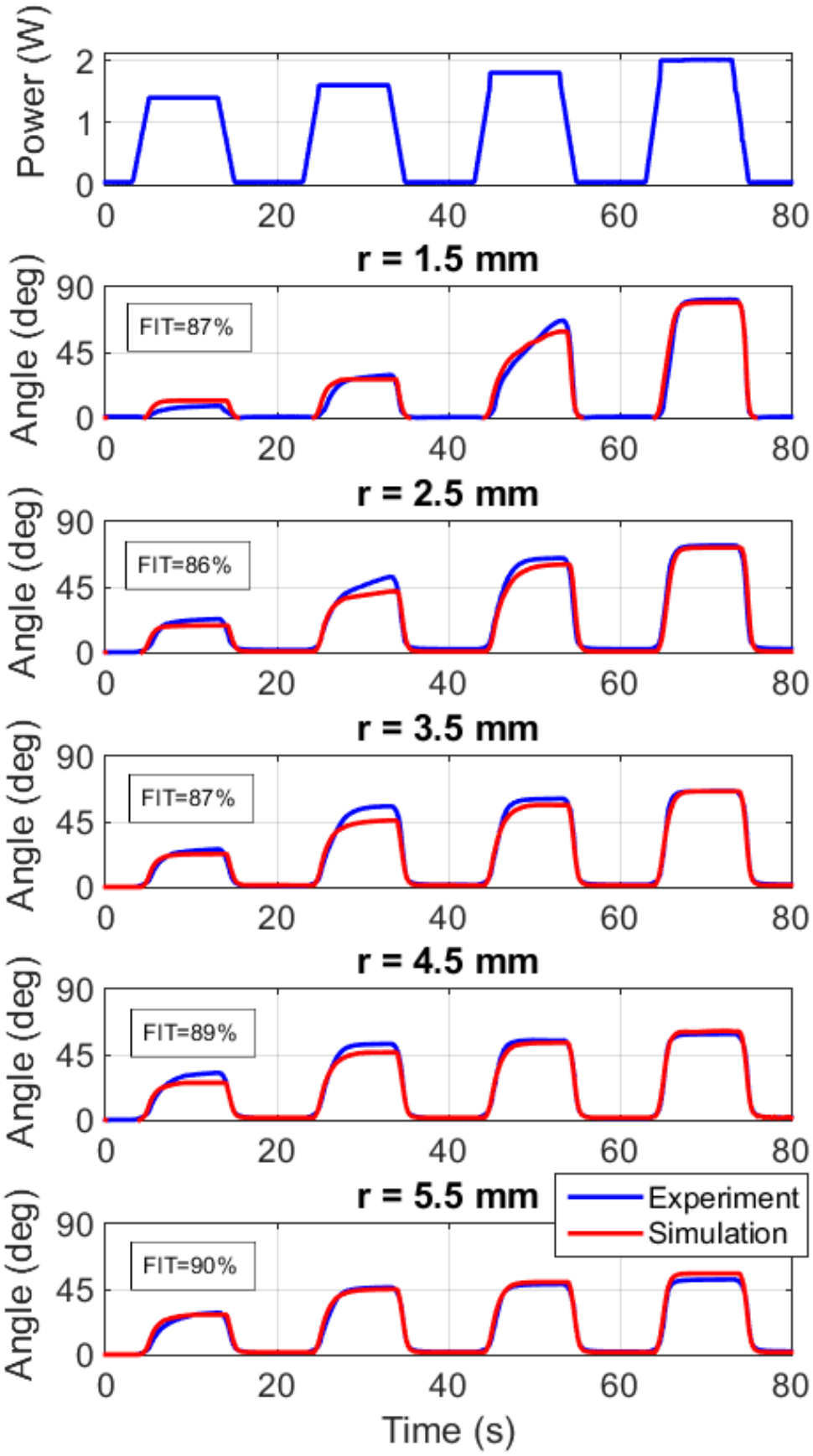

Figure 4.19: Model validation experiments, *r* = 1.5, 2.5, 3.5, 4.5, 5.5 mm, trapezoidal power signal at 1.4, 1.6, 1.8 and 2 W.. Experiment (blue line), simulation (red line).

4.7 Summary and Chapter conclusion

In this Chapter, a new concept for modeling an SMA-actuated robotic finger has been introduced. The goal is to develop a reliable physics-based model to be used for system simulation and structural optimization. At first, a finger structure close to the one described in Chapter 2 has been presented, and its COMSOL model implementation has been exposed. Then, a simplified version of the MAS model has been introduced for the SMA wire, together with its COMSOL implementation. A novel procedure to couple the 3D structure with the MAS model has then been presented, which requires only 30% of the computational time needed by conventional coupling algorithms commonly adopted in COMSOL. Subsequently, different sets of experiments have been performed by varying the prototype geometry (i.e., the distance between SMA wire and the phalanx center of rotation) and the system power input. Experimental measurements have been compared with the simulation results, showing a satisfactory agreement between acquired and simulated data trend. Some discrepancies can be noticed between simulations and experiments, mostly due to the use of a simplified SMA model. The polycrystalline extension of the MAS model has been implemented in the FE framework improving the simulation adherence to the real model behavior. A good agreement has been observed changing both the prototype geometry and the SMA wire input power.
In future works, a 3 DOF system actuated by protagonist-antagonist wire configuration will be consider in the simulation in order to better represent the behavior of the full SMA finger prototype described in Chapter 2. Finally, phenomena such as friction or heat exchange between wires in the bundle will be systematically investigated and, if needed, included in the modeling framework.

5 Concentrated Parameter Model for SMA Finger

In Chapter 2, a first concept for a 3D printed finger prototype actuated by SMA wires arranged in a protagonist-antagonist configuration is described. Despite the many features enabled by SMA technology, the prototype presented in Chapter 2 is still not able to completely fulfil the basic requirements for real life applications [11]. Along with the same purpose, in Chapter 3, a second generation of a bioinspired SMA hand prototype with soft features (SMA Soft Hand) has been presented. Encouraging performances in term of force, responsiveness and dexterity have been observed, even if some structural improvements are still strongly needed in order to properly meet human hand standards [11]. On the other hand, the limited SMA stroke, together with the material hysteresis, significantly increase the difficulties in the design, model and control of the devices based on this technology. According to this, in Chapter 4, a finite element framework is introduced to help improving the finger structure design, with a particular focus on the wire behavior and arrangement inside the structure.

Aside to an optimal structure design, in order to drive SMA hands fast and accurately in closed loop, reliable and computationally efficient models are necessary to compensate the material nonlinearities. A common approach to control SMAs consists of performing hysteresis compensation based on purely mathematical operators [56], [60]. It is remarked, however, that those models generally lack robustness with respect to changes in hysteresis with respect to different external conditions (e.g., contact forces and environmental temperature). For this reason, the development of physics-based models capable of explicitly accounting for the effects of external condition, as well as for material hysteresis and structural nonlinearities, is of high importance for the control of SMA hands in real life applications.

In literature, several authors have presented the kinematic and dynamic model of SMA-actuated robotic hands, see, e.g., [117]–[119]. These kinds of models, however, normally take into consideration only the device structure, while completely neglect the influence of the SMA wires. If the complex material hysteresis is not considered, the obtained model can be significantly simplified. On the other hand, neglecting the hysteresis can influence the accuracy of the resulting model, thus affecting the performance of the control system. In general, the coupled nonlinearities of both robotic structure and SMA material make modeling and control of SMA-actuated prosthetic hands a highly challenging task.

In this Chapter, a first attempt to develop a concentrated parameter model (for future control purposes) of a SMA-actuated finger is presented and experimentally validated. The finger structure is inspired to the ones used for the evaluations of Chapter 4.

The remainder of this Chapter is organized as follows. At first, the description of the prototype structure is presented. The overall system model is developed in Section 5.2.

Parametric identification and experimental validation are then performed on the complete model (SMA wire coupled with the mechanical structure) using both versions of the MAS model for shape memory alloys. The results are presented and compared in Section 5.3. Finally, in the last Section, some concluding remarks are provided.

5.1 Finger Prototype Structure

As mentioned previously, the goal of the work presented in this Chapter is the development of a concentrated parameter model for the SMA finger. The high energy density and flexibility of SMA alloys permits the design of compact actuation solutions with possible applications in robotics fields, ranging from industrial to biomedical ones. On the other hand, the hysteretic and highly nonlinear response of SMAs complicates system design, modeling, and control. In order to gradually approach the problem, a simple finger structure is, at first, considered to obtain the concentrated parameter model.
The prototype, depicted in Figure 5.1, is composed by a 3D printed structure having two phalanxes, the first one fixed and the second one free to rotate around a joint. First and second phalanx have a length of 200 mm and 50 mm, respectively. The base of both phalanxes is a square with side of 19 mm.

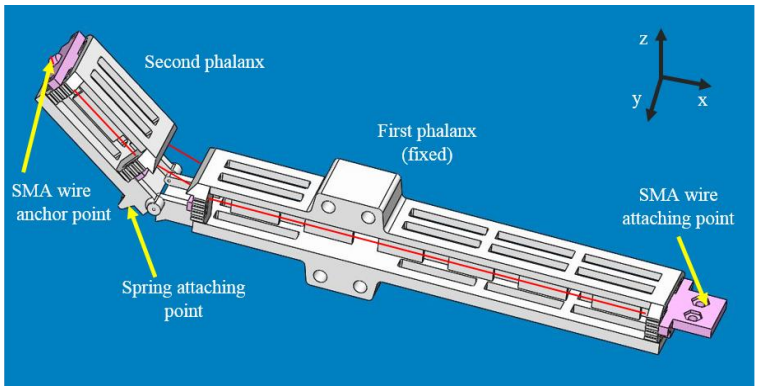

Figure 5.1: Finger CAD model

The first phalanx represents the finger middle phalanx, and bottom phalanx and part of the metacarpus, while the second one represents the human finger top phalanx.
The finger prototype actuation is based on a SMA-spring mechanism**.** When the wire is powered, a contraction is induced along its length, and generates a pulling force at the second phalanx wire attachment point. This leads to a rotation of the first phalanx. The linear spring connected to the second phalanx, shown in Figure 5.2, provides the force necessary to restore the finger initial position (Figure 5.2, a) once the SMA is unactuated. In order to ensure sufficient force to oppose to the restoring spring, the SMA wire has been wrapped twice along the two phalanxes. To insert it inside the structure, one wire side is

initially clamped at the first phalanx bottom side, then routed around the anchor point at the tip of the second phalanx, and finally fixed at the first phalanx bottom side. In this way, a bundle of two SMA wires mechanically in parallel is created. To ensure safe stress conditions for the wire, and avoid any residual strains, the wire is mounted while heated. This procedure thus permits to insert the wire always in a systematic way, and also to improve the material lifetime. To keep the wire in place inside the entire structure, some guides are designed inside the four brackets, mounted at the extremities of each phalanx (depicted in pink in Figure 5.1). Other than keeping the SMA wire in position, the brackets permits to vary the wire distance from the phalanx center of rotation. We define this distance as *r*. By varying *r*, it is possible to modify the conversion factor between stroke/force and angle/moment.

5.2 System Modeling

In this Section, a model of the finger actuator is developed. The model, based on a coupling between the finger structure with the Müller-Achenbach-Seelecke model for SMA material, allows to describe the dynamic and hysteretic response of the device in a physics-based fashion. In the following, two formulations for the finger structure model will be introduced and, then, the complete SMA finger model exposed.

5.2.1 Finger structure model: classic formulation

Kinematic and dynamic models of the finger structure are developed in this Section. The kinematic model relates the bending angle of the joint to the SMA length, while the dynamic model considers the SMA force as input and the resulting bending angle as output. Since all the finger structural components are manufactured with hard plastic, they are modeled as rigid bodies. Let us introduce first a fixed reference system, named Frame 0, whose origin O_0 coincides with the finger hinge joint center. We also introduce a rotating reference system, denoted as Frame 1, which is rigidly connected to the second phalanx, has origin O_1 coincident to the hinge joint center (i.e., $O_1 = O_0$), and *x* axis directed along the link connecting joint center and second phalanx. Both frames are shown in Figure 5.2. The following geometrical parameters are now introduced: SMA wire attachment points to the first and second phalanx, denoted as P_1 and P_2; restoring spring end-points, denoted as S_0 and S_1; distance *d* between the hinge joint center and both phalanxes; distance *r* between the SMA wire and the joint attachment point to the same phalanx, the rotation angle θ. All these quantities are illustrated in Figure 5.2.The coordinates of P_1 in Frame 0, as well as the coordinates of P_2 in Frame 1, are constant and can be obtained as follows

$$P_1^{(0)} = \begin{bmatrix} P_{1x}^{(0)} \\ P_{1y}^{(0)} \end{bmatrix} = \begin{bmatrix} -d \\ r \end{bmatrix}, \tag{5.1}$$

$$P_2^{(1)} = \begin{bmatrix} P_{2x}^{(1)} \\ P_{2y}^{(1)} \end{bmatrix} = \begin{bmatrix} d \\ r \end{bmatrix}. \tag{5.2}$$

When the SMA wire is activated the upper phalanx starts to rotate, therefore the coordinates of P_2 in Frame 0 will depend on θ. It is possible to define the following rotation matrix between Frame 1 and Frame 0

$$R_1^0(\theta) = \begin{bmatrix} \cos(\theta) & -\sin(\theta) \\ \sin(\theta) & \cos(\theta) \end{bmatrix}. \tag{5.3}$$

Through a coordinate transformation, we can now define the position vector P_2 in Frame 0 as follows

$$P_2^{(0)} = \begin{bmatrix} P_{2x}^{(0)} \\ P_{2y}^{(0)} \end{bmatrix} = R_1^0(\theta) P_2^{(1)} = \begin{bmatrix} d\cos(\theta) - r\sin(\theta) \\ r\cos(\theta) + d\sin(\theta) \end{bmatrix}. \tag{5.4}$$

By using (5.2) and (5.4), it is now possible to express distance between P_1 and P_2 in Frame 0 as follows

$$\left\| P_2^{(0)} - P_1^{(0)} \right\| = \sqrt{2d^2 + 2r^2 + 2\left(d^2 - r^2\right)\cos(\theta) - 4dr\sin(\theta)}, \tag{5.5}$$

where $||x||$ denotes the Euclidean norm of vector x. The SMA wire is composed by two fixed length parts, situated inside the two phalanxes having lengths L_1 and L_2 respectively, and a variable length portion, which connects points P_1 and P_2. It is assumed that the wire portion connecting points P_1 and P_2 follows a straight line. This is in good agreement with experimental observations. By using equation (5.5), the current SMA length l_{SMA} can then be finally obtained as follows

$$l_{SMA}(\theta) = L_1 + L_2 + \sqrt{2d^2 + 2r^2 + 2\left(d^2 - r^2\right)\cos(\theta) - 4dr\sin(\theta)}. \tag{5.6}$$

Equation (5.6) represents the finger kinematic model.

To develop a dynamic model for the finger, we consider the following equation describing the balance of moments

$$F_{SMA}\, b_{SMA}(\theta) - F_S(\theta) b_S(\theta) - b\dot{\theta} = I\ddot{\theta}, \tag{5.7}$$

where F_{SMA} represents the SMA force and b_{SMA} its lever arm, F_S the linear spring force and b_S its lever arm, I the second phalanx moment of inertia, and b is a viscous friction coefficient. To fully characterize model (5.7), we must find analytical expressions of b_{SMA}, F_S, and b_S as functions of θ. It is assumed that F_{SMA} produces a moment on the upper phalanx by acting along the straight line connecting P_1 and P_2. Therefore, the SMA force

lever arm is expressed as the distance between the rotation joint center O_0 and the straight line joining P_1 and P_2, i.e.,

$$b_{SMA}(\theta) = \frac{\left| P_{1x}^{(0)} P_{2y}^{(0)}(\theta) - P_{2x}^{(0)}(\theta) P_{1y}^{(0)} \right|}{\sqrt{\left(P_{2y}^{(0)}(\theta) - P_{1y}^{(0)} \right)^2 + \left(P_{2x}^{(0)}(\theta) - P_{1x}^{(0)} \right)^2}}. \tag{5.8}$$

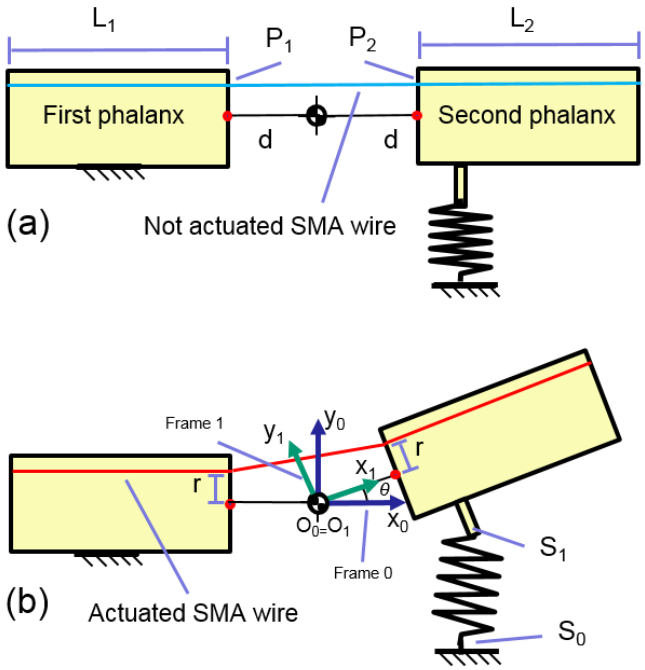

Figure 5.2: SMA finger actuator, unactivated (a) and activated (b). The model geometrical parameters are highlighted

To obtain the spring force F_S and its lever arm b_S, we must express both S_0 and S_1 in Frame 0. Coordinates of S_0 in Frame 0, as well as coordinates of S_1 in Frame 1, are constant and are given by the system geometrical design, thus we have

$$S_0^{(0)} = \begin{bmatrix} S_{0x}^{(0)} \\ S_{0y}^{(0)} \end{bmatrix}, \tag{5.9}$$

$$S_1^{(1)} = \begin{bmatrix} S_{1x}^{(1)} \\ S_{1y}^{(1)} \end{bmatrix}. \tag{5.10}$$

By using of the rotation matrix in (5.3), it is possible to express S_1 in Frame 0 as well

$$S_1^{(0)} = \begin{bmatrix} S_{1x}^{(0)}(\theta) \\ S_{1y}^{(0)}(\theta) \end{bmatrix} = R_1^0(\theta) S_1^{(1)} = \begin{bmatrix} S_{1x}^{(1)} \cos(\theta) - S_{1y}^{(1)} \sin(\theta) \\ S_{1x}^{(1)} \sin(\theta) + S_{1y}^{(1)} \cos(\theta) \end{bmatrix}, \tag{5.11}$$

where $S_{1x}^{(0)}$ and $S_{1y}^{(0)}$ represent the coordinates of S_1 in Frame 0. We can describe the spring force F_S by using Hooke's law, as follows

$$F_S(\theta) = k\left(\left\| S_1^{(0)} - S_0^{(0)} \right\| - l_{s0} \right) \tag{5.12}$$

where ls_0 is the spring initial length and k its stiffness. Force F_S produces a moment on the second phalanx by acting on the straight line connecting S_0 and S_1. The lever arm of this force is finally obtained by considering the distance between O_0 and the straight line connecting the points S_1 and S_2, i.e.,

$$b_s(\theta) = \frac{\left| S_{0x}^{(0)} S_{1y}^{(0)}(\theta) - S_{1x}^{(0)}(\theta) S_{0y}^{(0)} \right|}{\sqrt{\left(S_{1y}^{(0)}(\theta) - S_{0y}^{(0)} \right)^2 + \left(S_{1x}^{(0)}(\theta) - S_{0x}^{(0)} \right)^2}}. \tag{5.13}$$

The overall finger dynamic model can then be obtained by combining equations (5.7), (5.8) , (5.12) and (5.13).

5.2.2 Finger structure model: Lagrangian formulation

In the present Section, an alternative formulation of the finger structure model will be developed based on a Lagrangian formalism. Such a formulation is expected to provide the same results of the standard one based on moment calculations, by simply exploiting a scalar energy argument [120]. For consistency reasons, both model formulations have been implemented and compared.

To develop this alternative formulation of the model, let us first express the Lagrangian $\mathcal{L}$ as:

$$\mathcal{L} = T - U = \frac{1}{2} I \dot{\theta}^2 - \frac{1}{2} k (l_s(\theta) - l_{s0})^2 \tag{5.14}$$

where T and U represent the kinetic and potential energy respectively, I the structure inertia, θ the second phalanx rotation angle, k the spring stiffness, ls the spring length and ls_0 is the spring initial length. The equation of motion is given by:

$$\frac{d}{dt}\frac{\partial \mathcal{L}}{\partial \dot{\theta}} + \frac{\partial \mathcal{L}}{\partial \theta} = \tau \rightarrow I\ddot{\theta} + k(l_s(\theta) - l_{s0}) \frac{\partial l_s(\theta)}{\partial \theta} = \tau \tag{5.15}$$

where τ represents the torque produced by the SMA wires, plus an additional friction term. The principle of virtual works allows us to express τ as a function of the SMA force, as follows:

$$\tau = -F_{SMA} \frac{\partial l_{SMA}(\theta)}{\partial \theta} - b\dot{\theta} \tag{5.16}$$

By combining (5.15) and (5.16), we obtain

$$I\ddot{\theta} + k(l_s(\theta) - l_{s0}) \frac{\partial l_s(\theta)}{\partial \theta} + F_{SMA} \frac{\partial l_{SMA}(\theta)}{\partial \theta} + b\dot{\theta} = 0 \tag{5.17}$$

From the kinematic equations (5.11) and (5.6) we know that:

$$l_s(\theta) = \left\| S_1^{(0)} - S_0^{(0)} \right\|, \qquad l_{SMA}(\theta) = L_1 + L_2 \left\| P_2^{(0)} - P_1^{(0)} \right\| \tag{5.18}$$

We denote:

$$J_s(\theta) = \frac{\partial l_s(\theta)}{\partial \theta}, \qquad J_{SMA}(\theta) = \frac{\partial l_{SMA}(\theta)}{\partial \theta} \tag{5.19}$$

as the spring Jacobian and SMA Jacobian respectively. By comparing (5.7) and (5.17), the Jacobians can be interpreted as the lever arms of the corresponding forces. Therefore, by using (5.19), we can avoid the complex calculation involved in (5.8) and (5.13).

5.2.3 Complete Model

The models shown in the previous Sections can be systematically coupled to the SMA wire model described in Chapter 1, and used to simulate the overall actuator wire behavior. A scheme of such interconnections is reported in Figure 5.3. In this figure, each partial model is represented as a black box, in order to highlight the interconnections among them. In particular, the block labeled as Dynamic Model implements equations (5.7), (5.8) , and (5.11)-(5.13) to relate F_{SMA} to θ. Then, the Kinematic Model block implements (5.6) to transform θ into SMA length l_{SMA}. Finally, through the SMA Wire Model block is possible to obtain F_{SMA} as a function of l_{SMA}. F_{SMA} can then be used as input for the Dynamic Model block, allowing to close the loop. Note also that the SMA Material Model block depends on a second input, representing the electric power density used to control the finger. By changing J, it is possible to modify the wire reaction force, and change the bending angle θ consequently. The presented interconnection allows to simulate the complete model in any ODE simulation environment (e.g., Matlab/Simulink) in a causal way. In this Chapter, both the single crystal (SC) and the polycrystal (PC) extension of the SMA MAS model are implemented and their performances compared. Usually, the SC model, even if embodies a simplified representation of the real SMA behavior, is often chosen for its computational efficiency. On the other hand, when high accuracy is requested, the use of the PC model becomes essential, at the expense of simulation time. For this reason, in this Chapter, both models are implemented and compared. More details about MAS model versions are reported in Chapter 1.

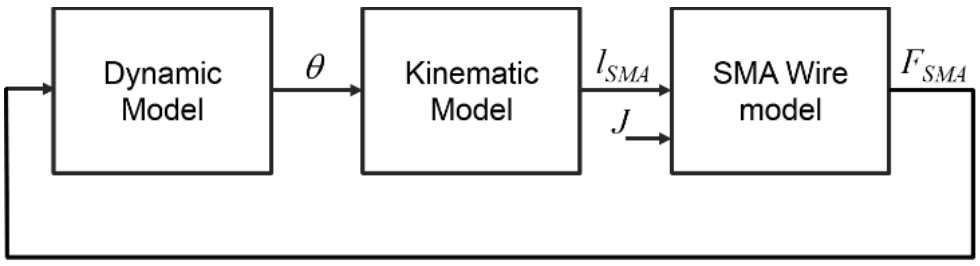

Figure 5.3: Complete model block diagram.

5.3 Experiments and parameter identification: single- crystal MAS model

In this Section, the experimental setup is first discussed. Then, model calibration and validation for the SC and PC SMA models are shown and compared.

5.3.1 Experimental setup

The experimental setup is composed by the finger prototype connected with a National Instruments cRIO-9074 real-time data acquisition system, programmed via LabVIEW 2012. The prototype motion is controlled via a NI-9472 module, working as a digital switch, capable of handling up to 30 volts at 100 μs switch time, while a NI-9472 constant voltage source is used to supply 28 V DC. A NI-9227 is used to read the current which flows in wires, and a NI-9229 module permits to measure its voltage. Based on voltage and current measurements, a PWM power control strategy is implemented in order to allow for direct control of *J*, in agreement with the developed model (see [64] and Chapter 4 for details). Before starting the experimental campaign, voltage and current, corresponding to a wire actuation of 500 μs, are measured.

Model Variables			
Model Variable Name	**Symbol**	**Value**	**Unit**
Modulus of austenite	E_A	50	GPa
Modulus of martensite	E_M	20	GPa
Transf. strain	ε_T	0.03	-
Width of stress-strain hysteresis	$\Delta\sigma$	50	MPa
Austenitic transf. stress at temperature T_L	σ_L	378	MPa
Gradient transf. stress respect to the temperature	$d\sigma/dT$	7	MPa/K
Reference temperature	T_L	373	K
Specific heat	c	512	J/kg
Heat convection coefficient	α	220	W/m^{2}K
Latent heat of phase transf.	h	24	kJ/kg

Table 5.1: Optimized Model Parameter for Single Crystalline Model.

This procedure permits to evaluate the maximum power for each wire. The desired input power profile is created on a host computer running LabVIEW. During the data acquisition, the host is connected to a Logitech web camera, synchronized with the power PWM signal. The acquired frames are then saved in a video file and post processed using MATLAB embedded libraries in order to compute the prototype motion. All the experiments are conducted in a controlled temperature environment.

As described in Chapter 2, for prosthetic hands, the force exerted at the tip of each finger represents an important design and evaluation quantity. To be able to predict the prototype force by varying its geometry, input power and external load, can enable an easier design

of both the finger prototype structure and also of a force control algorithm. In general, force measurements of rotating bodies are not an easy task. On the market several force sensors are available to fulfil this purpose, but all of them result expensive and not easily integrable with every system [10], [121], [122].
In order to obtain systematic and accurate measurements using standard lab equipment, the experiments previously described have been executed using two different springs, having a stiffness of 89 N/m and 250 N/m respectively. Recording the prototype displacement using different returning springs, indeed, gives us an idea of how an external load influences the SMA finger behavior. This enables the reconstruction of the SMA finger force.

5.3.2 Parameter Identification and Validation: Single crystal Model

In this Section, model identification and validation are performed by testing the finger actuator for several power inputs and geometries. At first, only the spring having a stiffness of 89 N/m is used. A sequence of three power profiles trapezoidal shaped, having the same period but different amplitude of 1.4, 1.7, and 2W respectively, is adopted as input. Such a signal is shown in Figure 5.4, upper part. This experiment is repeated for different distances between wire and hinge joint center of rotation, i.e., r = 2.5, 3.5, 4.5 mm. The measured angles obtained for different values of r are shown in Figure 5.4, blue lines.
It can be observed that, given the same input power, increasing this distance leads to a reduction of the resulting bending angle.
In order to predict the behavior of the finger prototype, a parameter identification is initially performed for the unknown model parameters. This procedure aims at finding the parameters which makes the angle computed using the mathematical model as close as possible to the measured one, for a predefined set of data. Parameters related to geometry and biasing spring, can be easily measured. The unknown parameters which require identification are the ones related to the SMA wire, i.e., E_A, E_M, ε_T, σ_L, T_L, $\Delta\sigma$, α, c and h. In principle, most of these material parameters are listed in the producer's datasheet [78]. We remark that that when this material is embedded inside a structure, undergoes an additional thermo-mechanical training which modifies its behavior. Therefore, these material parameters need to be fine-tuned in order to accurately reproduce the system behavior. The parameter identification is performed in MATLAB, by using embedded functions of the *Optimization Toolbox* to implement a nonlinear least-squares optimization. To increase the solver convergence speed, an admissible range is selected for each parameter according to physical considerations, as follows: $E_A \in$ [30, 70] GPa, $E_M \in$ [15, 30] GPa, $T_L \in$ [295, 395] K, $\Delta\sigma \in$ [40,150] MPa, $\sigma_L \in$[100, 600] MPa, $\varepsilon_T \in$ [0.02, 0.04], $\alpha \in$ [90, 400] W/K·m^2, $c \in$ [450, 550] J/kg·K; $h \in$ [12, 25] kJ/kg.
The identification is performed considering the experiments realized using r = 2.5 mm and a spring stiffness of k = 89 N/m and r = 4.5 mm and a spring stiffness of k = 240 N/m.

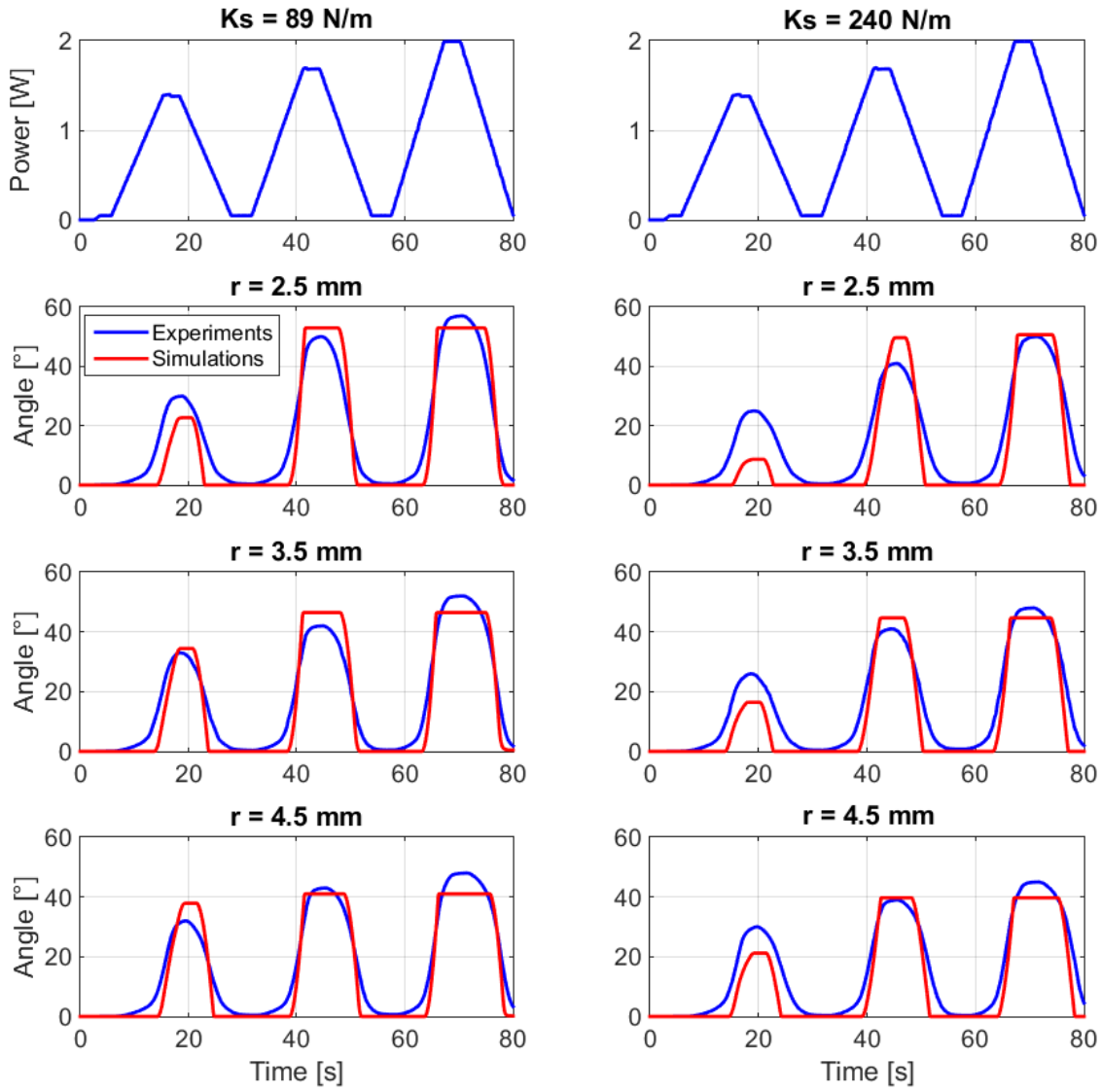

Figure 5.4: SC Model validation experiments, r = 2.5, 3.5,4.5 mm, trapezoidal power signal at 1.4,1.6,1.8 W, experiment (blue line), simulation (red line). (Left-hand side): Experiments performed using a 89 N/m restoring spring. (Right-hand side): Experiments performed using a 240 N/m restoring spring

The remaining experiments are used for the model validation. In Figure 5.4 a comparison between experimental and simulated curves is shown. Analyzing the model performance for different values of *r*, *k* and input powers, it can be noticed that the accuracy of the predicted angle (Figure 5.4, red line) is generally good for high value of power. For lower values of power, and for *r* = 2.5 mm, the model accuracy decreases. In general, the accuracy decreases when reducing the value of *r*, for which a larger bending angle is observed. This is mostly due to the adopted material model, which is based on a single-crystal approximation of the SMA behavior. The use of this kind of model introduces also sharp edges in the angle profile, which are more evident for higher input power.

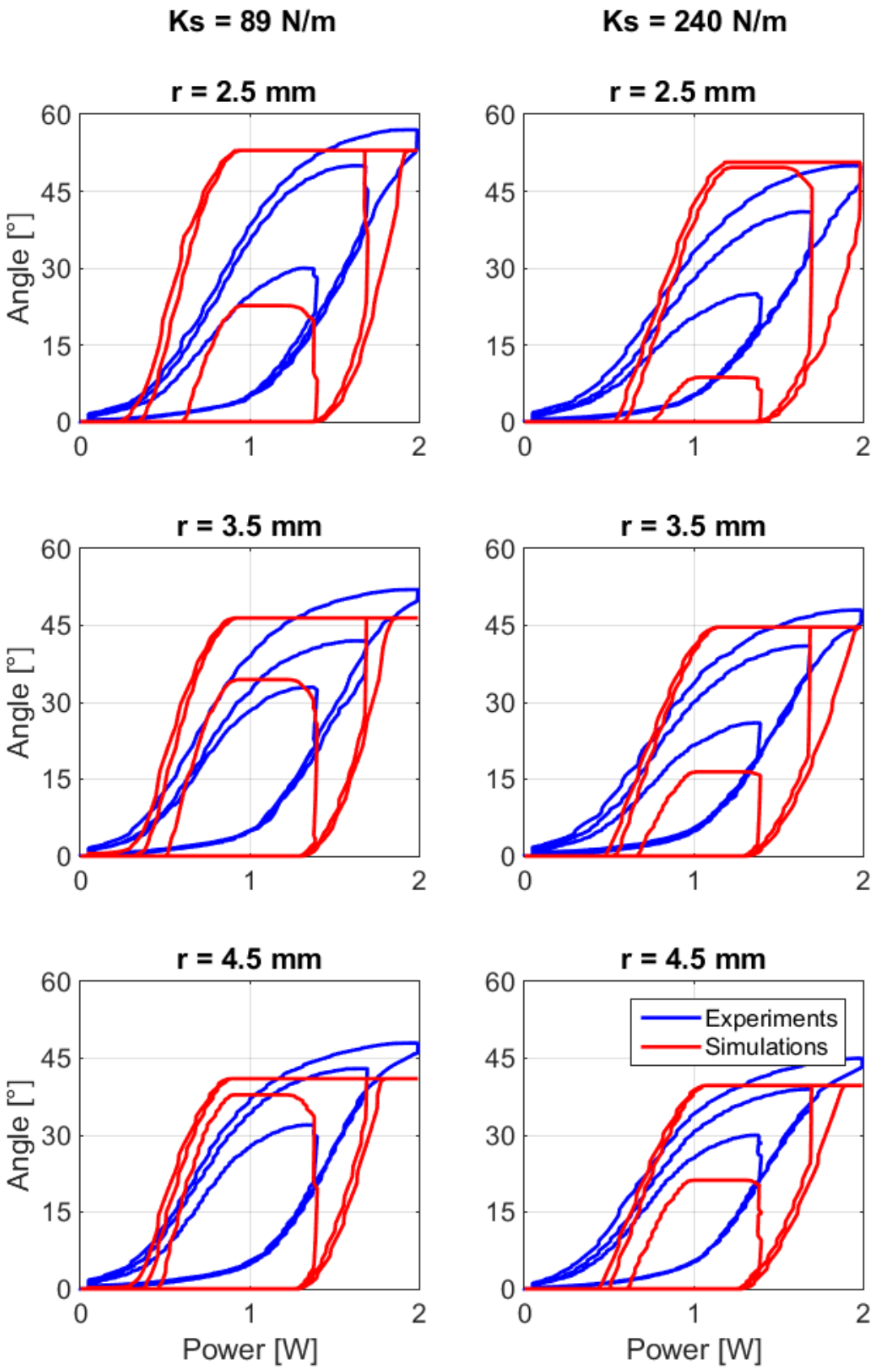

Figure 5.5 : SC Hysteresis for r = 2.5, 3.5,4.5 mm, trapezoidal power signal at 1.4,1.6,1.8 W, experiment (blue line), simulation (red line). (Left-hand side): Experiments performed using a 89 N/m restoring spring. (Right-hand side): Experiments performed using a 240 N/m restoring spring.

In Figure 5.5, the power-rotation angle hystereses are represented. Even though Figure 5.4 seems to suggest that the model has a good adherence to the real system behavior, Figure 5.5 shows how each simulated hysteresis significantly deviates from the corresponding measured one. The model is able to well capture the internal loops rising fronts, but not their shape. As a result of this inaccuracy, hysteresis compensation based on this model may turn out to be ineffective in real-life applications.

5.3.3 Parameter Identification and Validation: Polycrystalline Model

In the previous Section, the parameters of the MAS single crystal model have been identified. The real and the simulated system behavior have been compared, and a significant deviation between the two behavior has been highlighted. In order to increase the adherence to the real system behavior, the polycrystalline extension of the MAS model, accurately described in Chapter 1 of this dissertation, is adopted.

The PC model is characterized by several parameters, which permit to better shape the SMA hysteresis. On the other hand, the high number of parameters makes the identification procedure more challenging. To simplify this procedure, a two-step algorithm is adopted. As a first step, single-crystal model parameters are identified. Based on the single-crystal parameters, proper functions for σ_A, σ_M, σ_S as a function of x_+ are then characterized.

This two-step procedure permits to simplify the overall process, since a smaller number of parameters has to be identified at each step. The obtained single crystal parameters are used as a starting point for the calculation of the polycrystalline hysteresis as described in [115], [116]. This means that the same values of E_A, E_M, ε_T, T_L, α, c, and h obtained for the single-crystal model are used as initial parameters for the identification routine (Table 5.1). Therefore, the only parameters which have to be identified are the scaling curves $\sigma_A(x_+,T_L)$, $\sigma_M(x_+,T_L)$ and $\sigma_S(x_+)$. These curves are implemented via standard interpolation methods, based on sigmoid. The weights of every sigmoid are the solution of a least-square objective function, which computes the mean squared error between the simulated angle (variable of the model) and the measured one.

For the model identification, the experiments corresponding to r = 2.5 mm and restoring spring k = 240 N/m and r = 4.5 mm and restoring spring k = 89 N/m are used. The remaining experiments are used for the model validation. The identification results are shown in Figure 5.6 and Figure 5.7, where the finger angular displacements over time and the finger rotation angle-power hystereses are respectively depicted. Analyzing the model performance for different values of r, k and input powers, it can be noticed that the accuracy of the predicted angle (red line) is very high both for high and for low powers. The PC simulated behavior is very smooth and the angle profile does not anymore show a sharp profile (in contrast to the SC model). The greatest improvement is appreciable in Figure 5.7, where the identified hystereses shape (red line) fit very good the real model behavior (blue line). Both the internal and the external loops are well captured by the model also

varying *r* and *k*, with an average fit of 88%. This high precision of the simulated system behavior allows a good estimation of the SMA finger force when an external force is applied.

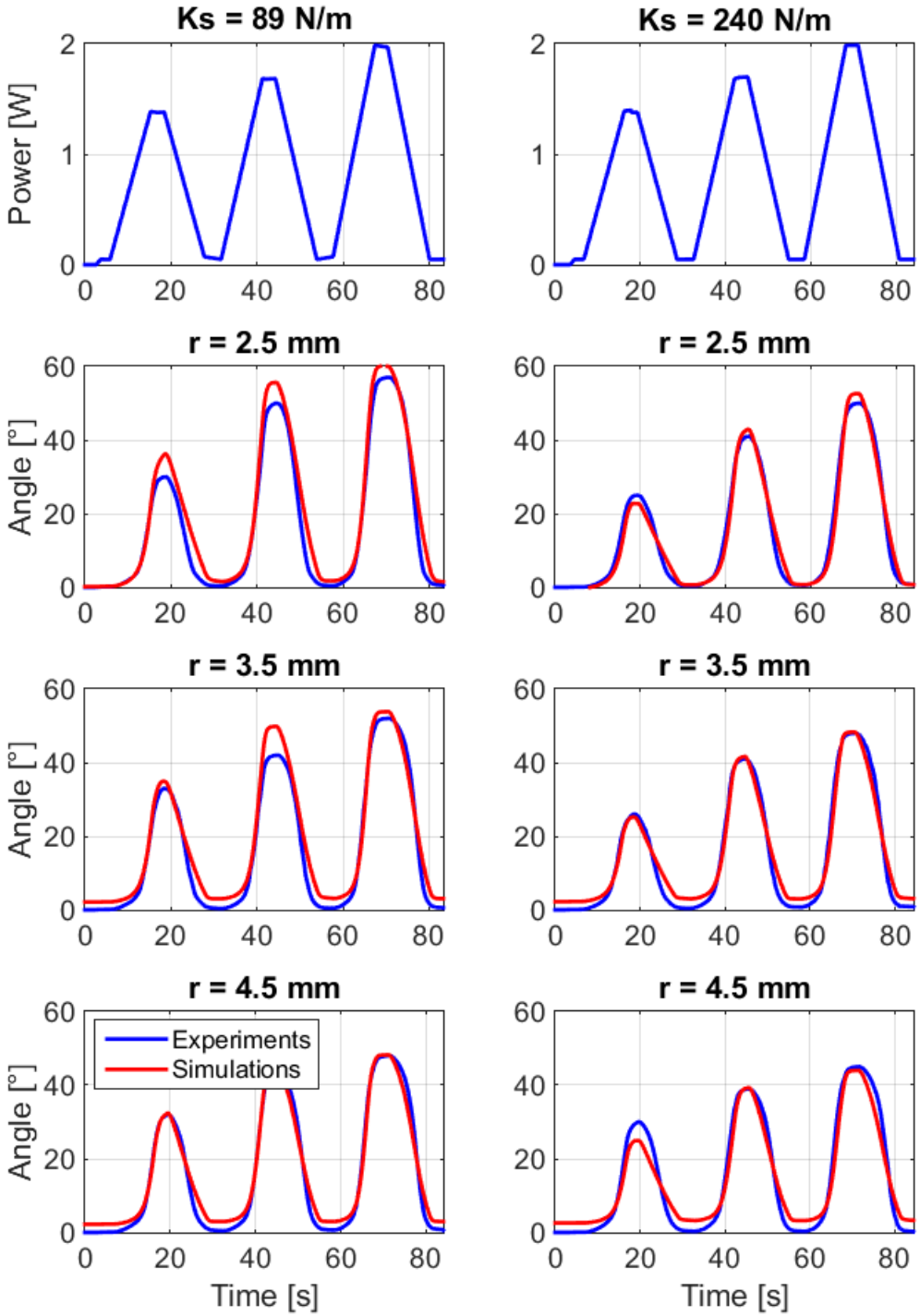

Figure 5.6: PC Model validation experiments, r = 2.5, 3.5,4.5 mm, trapezoidal power signal at 1.4,1.6,1.8 W, experiment (blue line), simulation (red line). (Left-hand side): Experiments performed using a 89 N/m restoring spring. (Right-hand side): Experiments performed using a 240 N/m restoring spring.

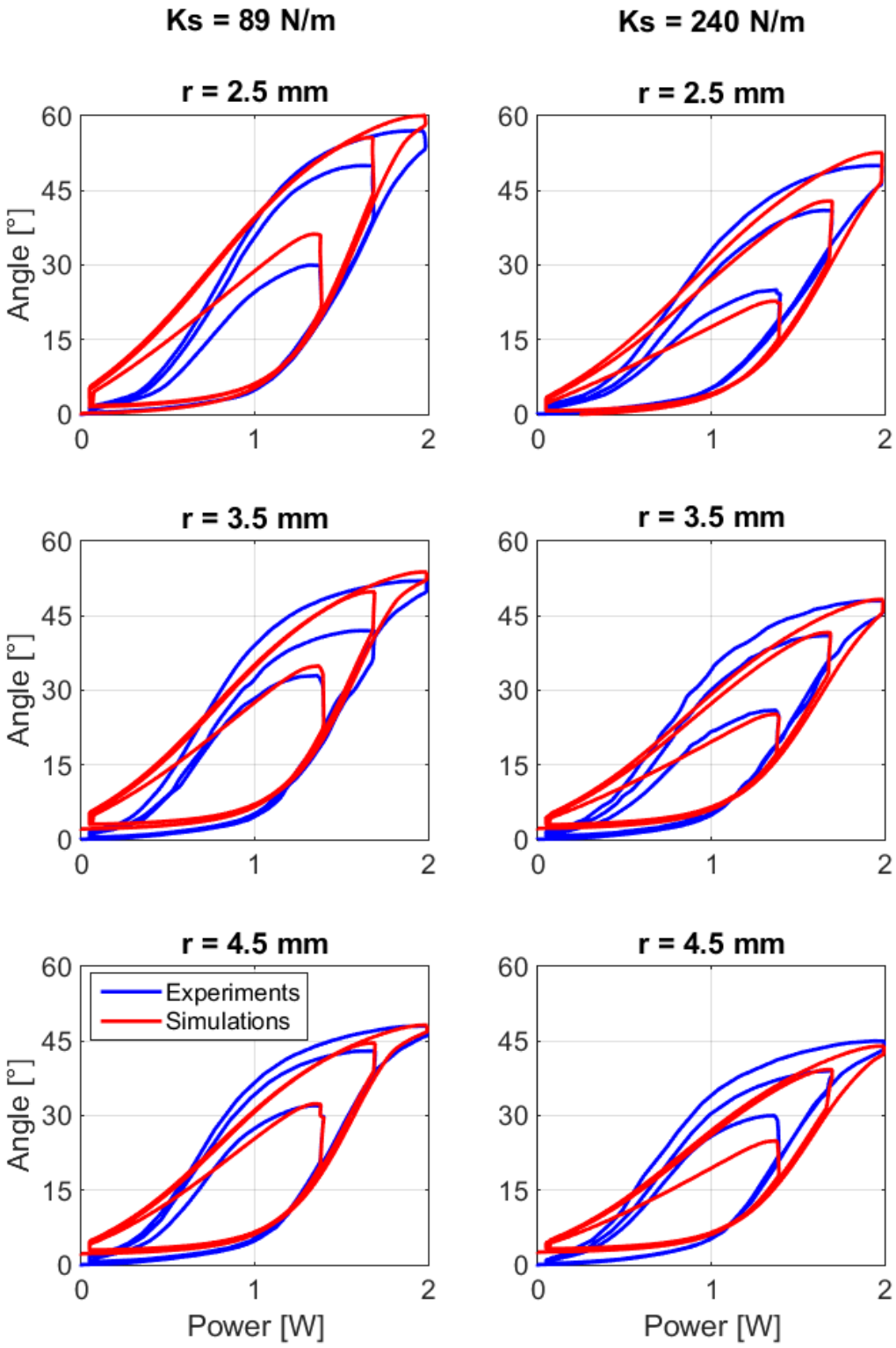

Figure 5.7: PC Hysteresis for r = 2.5, 3.5,4.5 mm, trapezoidal power signal at 1.4,1.6,1.8 W, experiment (blue line), simulation (red line). (Left-hand side): Experiments performed using a 89 N/m restoring spring. (Right-hand side): Experiments performed using a 240 N/m restoring spring.

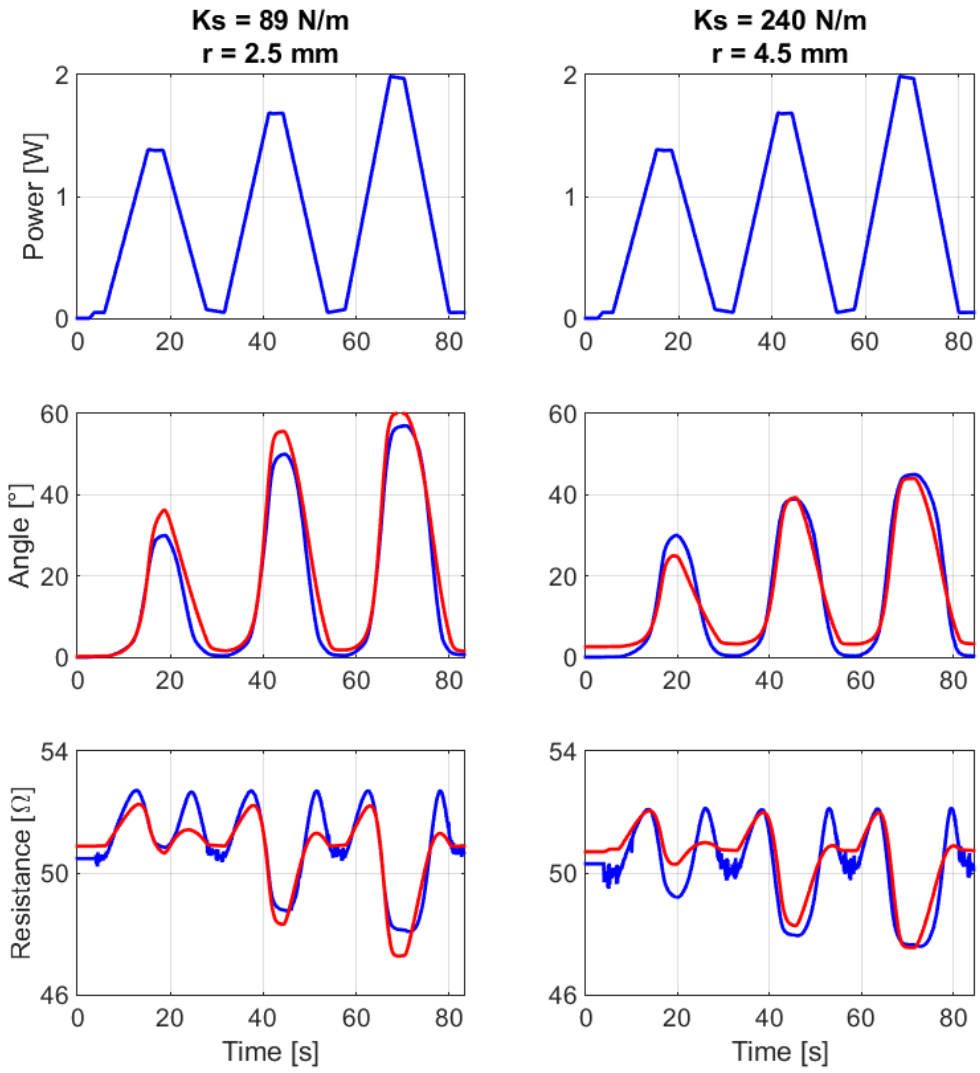

Figure 5.8: SMA finger resistance and angular displacement using trapezoidal power signal at 1.4,1.6,1.8 W, experiment (blue line), simulation (red line). (Left-hand side): Experiments performed using a 89 N/m restoring spring. (Right-hand side): Experiments performed using a 240 N/m restoring spring.

5.3.4 SMA finger self-sensing: consideration on resistance

As demonstrated in Chapter 2, it is possible to relate the SMA finger angular displacement to the change in resistance in the SMA wires mounted inside the prototype. By exploiting this property, it is possible to know the state of the alloy inside any structure without using any additional sensor, but only via a measurement of the SMA resistance. Such a unique SMA feature is often referred to as self-sensing.

In Chapter 1, the MAS model for the SMA resistance has been described. Combining it with the PC model, it is possible to directly relate the finger model identified in the previous Section to the SMA resistance. In order to identify the parameters characterizing the resistance behavior without further complicating the algorithm used for hysteresis

parameter identification, a least square problem is formulated and used as a third step after the identification of the PC angular displacement- power hysteresis. In Figure 5.8, the SMA identified and measured resistance behaviors are compared. Even if the identification of the thermo-mechanical behavior of the SMA finger is quite satisfactory (Figure 5.8, center part), the least square approach did not return parameters able to perfectly depict the real SMA resistance behavior (Figure 5.8, bottom part). Even though the average trend is captured, for every experiment the second resistance peak, corresponding to the austenite-martensite transition, is not well described by the model. This mismatch is also visible in Figure 5.9, where the model describes an unrealistic hysteresis in the left part of both resistance characteristics.

In future research works, this discrepancy will be further investigated in order to understand if the error in the identified resistance behavior is determined by unmodeled phenomena (e.g., R-phase of the SMA, thermal exchange between the SMA wires and the structure), which have a non-negligible effect on the overall resistance behavior.

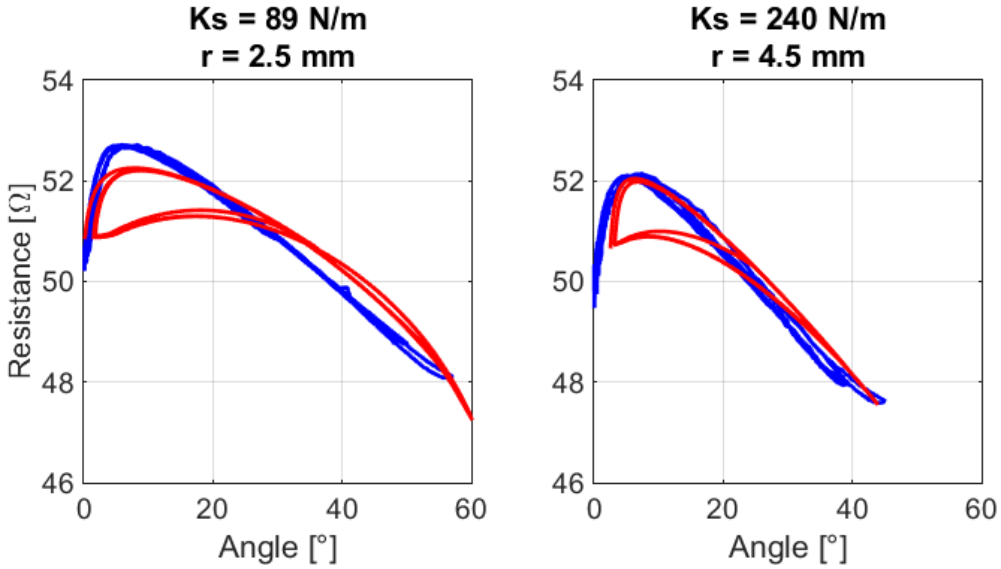

Figure 5.9: SMA finger resistance over angular, experiment (blue line), simulation (red line). (Left-hand side): Experiments performed using a 89 N/m restoring spring. (Right-hand side): Experiments performed using a 240 N/m restoring spring.

5.4 Summary and Chapter conclusion

In this Chapter, a dynamic concentrated parameter model for a SMA actuated finger has been presented. The model accounts for both the structure and the material behavior. At first, the prototype structure has been described, and its dynamic model has been developed. Then, the model has been coupled with a single crystal version of the MAS model for SMA wires. Several experiments have been conducted by varying the SMA wire input power and

distance from the second phalanx rotation center, to be used for parameter identification and validation. Experiments and simulations have subsequently been compared. The model remarkably agrees with experiments for larger values of *r* and input power, while the accuracy becomes poor for smaller *r* and *J*. The error between model and experimental system behavior is mostly due to the use of a simplified SMA model, which is based on single-crystal assumptions. As a consequence of these inaccuracies, hysteresis compensation based on this model may turn out to be ineffective in real-life applications. To overcome this issue, the polycrystalline extension of the MAS model is subsequently introduced. The simulations obtained used this new model show a very good adherence to the experiments, both for high and for low input power values. A model for the SMA resistance is introduced and used to identify the real SMA resistance behavior. An average agreement is showed between real and simulated behavior, even though several mismatches can be noticed. In future works, the SMA resistance behavior and its model will be further investigated in order to improve the inaccuracies observed in this work. The presented approach will be expanded to a protagonist-antagonist SMA wires system. Then, model-based control approaches will be developed and tested.

6 Conclusions and Outlook

In this thesis, the development of performant and cost-effective hand prostheses is presented. Shape Memory Alloy (SMA) wires are proposed as actuators of the developed hand prototypes, since this technology is potentially attractive for the realization of artificial hands. In fact, SMA wires can be easily integrated in mechanical structures without requiring large amount of space and complex gearing mechanisms, therefore favoring the optimization of production costs and device weight. Moreover, SMA wires are completely silent when activated. Although these advantages, devices based on SMA technology oftentimes are accompanied by preconceptions of slow actuation and limited stroke output. The hand prototypes presented in this work of thesis demonstrate how to design a performant and innovative prostheses, exploiting all the advantages and overcoming most limitations of the SMA technology. Moreover, the developed finite element framework aims at modelling the fingers hand behavior and enable future structure optimizations. Aside this, the presented concentrated parameter model will favor future implementation of optimal control strategies.

The aim of this work is to favor the development of affordable prostheses ensuring at the same time good performances and higher acceptance rate by the users.

In Chapter 2, a first concept for a SMA actuated hand is developed. The design makes use of bundles of thin protagonist-antagonist SMA wires wrapped several times along the finger phalanxes. When heated via an electric current, the SMA wires contract and produce a rotation of the finger joints, mimicking the fibers of human muscles. This bio-inspired solution leads to devices with relatively high compactness and power density. The protagonist-antagonist configuration allows to achieve a higher actuation speed with respect to a simple, standard SMA-spring arrangement. Furthermore, each finger phalanx can be driven independently of the others, increasing the overall dexterity. The prototype has been tested in order to evaluate its force, motion and reactiveness. The experiments have shown performances sufficient to use the SMA finger as prosthetic device, but still strongly improvable modifying the prototype structure.

In order to design a hand device with better performances, in Chapter 3, a second generation of SMA actuated finger having soft features (SMA Soft Hand) is described. The modular finger structure uses superelastic SMA wires in the joint in order to enable soft features. These wires have been arranged according to a X-shaped pattern in order to avoid undesired joint configurations under induced lateral moments. Bundles of actuated SMA wires have been systematically manufactured using a welding method, in order to ensure an identical behavior of each wire in the same bundle. The use of SMA wires as actuators permits the

design of a compact, lightweight, and silent hand devices. A protagonist-antagonist configuration has been chosen for the SMA bundles, in order to enable higher prototype reactiveness. In addition, the modular structure permits a simple and fast replacement of possible damaged SMA actuator bundles, avoiding to replace the entire finger assembly. A five-fingered hand prosthesis having an entirely 3D printed structure is then presented.
Several tests have been performed in order to demonstrate the hand prototype capabilities. Force measurements have been realized at the finger top phalanx, while activating all the protagonist bundles in the finger. A force of about 9 N per finger has been evaluated, which leads to an overall hand prototype force of about 45 N. Such a value is within the range of human hand force. The complete motion of each finger phalanx has also been recorded, showing also in this case values comparable with human fingers (45° for the tip phalanx, 90 ° for the middle and bottom phalanxes). Using a short pulse power excitation, a settling time between 0.2 s and 0.3 s has been observed for both rising and falling rotation phases. The described method can enable better performances if an adequate hardware is used. Objects with different sizes and shapes have been grasped by the SMA hand prototype, demonstrating its high gripping versatility. Comparing the SMA hand prototype with the most important prostheses developed so far, relevant advantages especially in term of noiseless actuation, cost, weight, responsiveness and force can be highlighted. Despite the big improvements achieved with this second generation of a SMA actuated Hand, several nonnegligible problems are detected also in this prototype concept. Overheating, wires friction and poor possibility of dimensions scaling represent the main limitations in the SMA Soft Hand.

In order to better understand the interaction between the SMA actuators and the finger structure and, in turn, improve the prototype design and wire placement, a finite element (FE) based framework is developed in Chapter 4. Due to high nonlinearity of the SMA model and to its complex interaction with the structure (i.e. contact phenomena), it is necessary, as first step, to focus on modeling and simulation of a two phalanxes SMA-actuated finger. The considered system consists of a rotational joint activated by a bundle of SMA wires. A restoring spring is also connected to the joint, and allows to recover initial configuration when the wire is not activated. The approach accounts for a fully coupled system, in which each SMA wire reacts to different power stimuli inducing a motion in the finger prototype, according to the system input. The model is developed in a FE framework, since this environment permits to naturally implement highly nonlinear phenomena observed in the considered structure such as contact problems and kinematic constraints. For describing SMA material dynamics, the physics-based Müller-Achenbach–Seelecke (MAS) model is adopted, and its two versions, the single crystal and the polycrystalline, implemented and their performances compared**.** The contact problem between SMA wire and structure makes the SMA model implementation highly involved on a computational standpoint. For this reason, a novel strategy is proposed for implementing such a contact in

a computationally efficient way. After discussing model equations and COMSOL implementation, experimental identification and validation are performed for different geometries and input commands.

To drive the SMA finger fast and accurately in closed loop, reliable and computationally efficient models are necessary to compensate the material nonlinearities. Therefore, in the last Chapter, a concentrated parameters physics-based model capable of explicitly accounting for the effects of external conditions, as well as for material hysteresis and structural nonlinearities, is developed. Such type of model can be used for controlling the SMA finger in real life applications. Due to high nonlinearity of the SMA model and to its complex interaction with the structure, as first attempt to develop a concentrated parameter model of a SMA-actuated finger, the simplified finger structure used in Chapter 4, is adopted. The model takes into account the coupling between the finger structure and the SMA dynamic behavior in a physics-based fashion. In order to take into accounts the SMA internal dynamics in a thermodynamically consistent way, the Müller-Achenbach–Seelecke (MAS) models (single crystal and polycrystalline extension) are used**.** After deriving the model equations, the parameters are identified and validated thought different experiments performed for different input commands and geometries.

In future works, the thumb mechanism will be improved by adding also adduction/abduction and opposition movements in order to increase the hand dexterity. The FE framework and the concentrated parameter model will be extended also for the antagonist wire arrangement. Advanced simulation tools and motion/interaction control algorithms will be also developed. In this way, it will be possible to further optimize the prototype design, as well as to mimic the motion and gesture of a real human hand and perform a more precise grasping of both fragile and small-size objects.

7 References

[1] C. Connolly, "Prosthetic hands from Touch Bionics", *Industrial Robot: An International Journal*, pp. 290–293, 2008.

[2] C. Medynski and B. Rattray, "Bebionic Prosthetic Design", *Symposium MyoElectric Controls/Powered Prosthetics Symposium (MEC)*, pp. 1–4, 2011.

[3] J. M. Miguelez, "Clinical Experiences With The Michelangelo Hand: A Four-Year Review", *Symposium MyoElectric Controls/Powered Prosthetics Symposium (MEC)*, 2011.

[4] C. Cipriani, M. Controzzi and M.C. Carrozza,"The SmartHand transradial prosthesis", *J. Neuroeng. Rehabil.,*vol. 8, no.1, pp. 8-29, 2011.

[5] F. Lotti, P. Tiezzi, G. Vassura, L. Biagiotti, G. Palli and C. Melchiorri, "Development of UB Hand 3: Early results", *IEEE International Conference on Robotics and Automation*, pp. 4488–4493, 2005.

[6] Shadow Robot Company, "Shadow Dexterous Hand Technical Specification", *Shadow Dexterous Hand E1 Series*, 2013.

[7] Exiii Hand [Online]: http://www.exiii.jp.

[8] G. Jones, G and R. Stopforth, "Mechanical Design and Development of the Touch Hand II Prosthetic Hand", *R&D J.*, vol. 32, pp. 22–34, 2016.

[9] J. T. Belter, J. L. Segil, A. M. Dollar and R. F. Weir, "Mechanical design and performance specifications of anthropomorphic prosthetic hands: a review", *J. Rehabil. Res. Dev.*, vol. 50, no. 5, pp. 599–618, 2013.

[10] H. Kawasaki, T. Komatsu and K. Uchiyama, "Dexterous anthropomorphic robot hand with distributed tactile sensor: Gifu hand II", *IEEE/ASME Trans. Mechatronics*, vol. 7, no. 3, pp. 296–303, 2002.

[11] E. Biddiss, D. Beaton and T. Chau, "Consumer design priorities for upper limb prosthetics", *Disabil. Rehabil. Assist. Technol.*, vol. 2, no. 6, pp. 346–357, 2007.

[12] D. Trivedi, C. D. Rahn, W. M. Kier and I. D. Walker, "Soft robotics: Biological inspiration, state of the art, and future research", *Appl. Bionics Biomech.*, vol. 5, no. 3, pp. 99–117, 2008.

[13] P. H. Kyberd, P. J., Gow and D. Chappell, "Research and the future of myoelectric prosthetics", *Powered Up. Limb Prostheses*, pp. 175-190, 2004.

[14] V. Bundhoo, E. Haslam, B. Birch and E. J. Park, "A shape memory alloy-based tendon-driven actuation system for biomimetic artificial fingers, part I: design and evaluation", *Robotica*, vol. 27, no. 1, p. 131, 2008.

[15] H. Takeda, N. Tsujiuchi, T. Koizumi, H. Kan, M. Hirano and Y. Nakamura, "Development of prosthetic arm with pneumatic prosthetic hand and tendon-driven wrist", *Annu. Int. Conf. IEEE EMBS*, pp. 5048-5051, 2009.

[16] S. Schulz, C. Pylatiuk and G. Bretthauer, “A new ultralight anthropomorphic hand”, *IEEE International Conference on Robotics and Automation*, vol. 3, pp. 2437–2441, 2001.

[17] J. R. Amend, E. Brown, N. Rodenberg, H. M. Jaeger and H. Lipson, “A positive pressure universal gripper based on the jamming of granular material”, *IEEE Trans. Robot.*, vol. 28, no. 2, pp. 341–350, 2012.

[18] B. Finio, R. Shepherd and H. Lipson, “Air-powered soft robots for K-12 classrooms”, *IEEE Integrated STEM Education Conference*, pp. 1-6, 2013.

[19] S. Wakimoto, K. Ogura, K. Suzumori and Y. Nishioka, “Miniature Soft Hand with Curling Rubber Pneumatic Actuators”, *IEEE Int. Conf. Robot. Autom.*, pp. 556–561, 2009.

[20] K. O’Toole, *A methodology towards comprehensive evaluation of shape memory alloy actuators for prosthetic finger design*. University of Dublin, 2011.

[21] D. C. Lagoudas, *Shape memory alloys : modeling and engineering applications*. Springer, 2008.

[22] F. J. Gil and J. A. Planell, “Shape memory alloys for medical applications”, *Proc. Inst. Mech. Eng. H.*, vol. 212, no. 6, pp. 473–488, 1998.

[23] J.Jung, *Aufbau eines Greifmechanismus mit FGL-Drahtaktoren*. Fraunhofer-Institut Dresden, 2009.

[24] J. H. Lee, S. Okamoto and S. Matsubara, “Development of Multi-Fingered Prosthetic Hand Using Shape Memory Alloy Type Artificial Muscle”, *Comput. Technol. Appl. 3*, vol. 3, pp. 477–484, 2012.

[25] T. Maeno and T. Hino, “Miniature of a Five-fingered Root Hand driven with Shape Memory Alloys”, in *Proc. 12th IASTED International Conference*, 2006.

[26] K. Andrianesis and A. Tzes, “Development and Control of a Multifunctional Prosthetic Hand with Shape Memory Alloy Actuators”, *J. Intell. Robot. Syst.*, vol. 78, no. 2, pp. 257–289, 2014.

[27] K. Otsuka and C. M. Wayman, *Shape memory materials*. Cambridge university, 1999.

[28] L. Lecce, *Shape memory alloy engineering: for aerospace, structural and biomedical application*s. Elsevier, 2014.

[29] R. Smith, *Smart material systems: model development.* Society for Industrial and Applied Mathematics, 2005.

[30] J. Ortín and L. Delaey, “Hysteresis in shape-memory alloys”, *Int. J. Non. Linear. Mech.*, vol. 37, no. 8, pp. 1275-1281, 2002.

[31] F. Zanaboni, E. Massarotti, V. Auricchio, *One Way and Two Way–Shape Memory Effect: Thermo–Mechanical Characterization of Ni–Ti wires.* Pavia University, 2008.

[32] Y. Huo, I. Müller and S. Seelecke, “Quasiplasticity and pseudoelasticity in shape memory alloys”, *Phase transitions and hysteresis*, Springer, Berlin, Heidelberg, pp. 87-146, 1994.

[33] C. Lexcellent, S. Leclercq, B. Gabry and G. Bourbon, “Two way shape memory effect of shape memory alloys: an experimental study and a phenomenological model”, *Int. J. Plast.*, vol. 16, no. 10, pp. 1155- 1168, 2000.

[34] H. Scherngell and A. C. Kneissl, “Training and stability of the intrinsic two-way shape memory effect in Ni-Ti alloys”, *Scr. Mater.*, vol. 39, no. 2, 1998.

[35] D. A. Hebda and S. R. White, “Effect of training conditions and extended thermal cycling on nitinol two-way shape memory behavior”, *Smart Mater. Struct.*, vol. 4, p. 298, 1995.

[36] S. J. Savage, “Engineering aspects of shape memory alloys”, *International Materials Reviews*, vol. 36, p. 273, 1991.

[37] J. A. Shaw and S. Kyriakides, “Thermomechanical aspects of NiTi”, *J. Mech. Phys. Solids*, vol. 43, pp. 1243-1281, 1995.

[38] K. Otsuka, H. Sakamoto and K. Shimizu, “Successive stress-induced martensitic transformations and associated transformation pseudoelasticity in Cu-Al-Ni alloys”, *Acta Metall.*, vol. 24, n. 4, 1979.

[39] C. Yu, G. Kang and Q. Kan, “Study on the rate-dependent cyclic deformation of super-elastic NiTi shape memory alloy based on a new crystal plasticity constitutive model”, *Int. J. Solids Struct.*, vol. 51, pp. 4386-4405, 2014.

[40] J. G. Boyd and D. C. Lagoudas, “A thermodynamical constitutive model for shape memory materials. Part I. The monolithic shape memory alloy”, *Int. J. Plast.*, vol. 12, no. 6, pp. 805–842, 1996.

[41] J. G. Boyd and D. C. Lagoudas, “A thermodynamical constitutive model for shape memory materials. Part II. The SMA composite material”, *Int. J. Plast.*, vol. 12, no. 7, pp. 843–873, 1996.

[42] K. Tanaka and S. Nagaki, “A thermomechanical description of materials with internal variables in the process of phase transitions”, *Ingenieur-Archiv*, vol. 51, no. 5, pp. 287–299, 1982.

[43] L. C. Brinson, “One-Dimensional Constitutive Behavior of Shape Memory Alloys: Thermomechanical Derivation with Non-Constant Material Functions and Redefined Martensite Internal Variable”, *J. Intell. Mater. Syst. Struct.*, vol. 4, no. 2, pp. 229–242, 1993.

[44] C. Liang and C. A. Rogers, “One-Dimensional Thermomechanical Constitutive Relations for Shape Memory Materials”, *J. Intell. Mater. Syst. Struct.*, vol. 1, no. 2, pp. 207–234, 1990.

[45] I. Müller and S. Seelecke, “Thermodynamic aspects of shape memory alloys”, *Math. Comput. Model.*, vol. 34, no. 12–13, pp. 1307–1355, 2001.

[46] M. Achenbach, “A model for an alloy with shape memory”, *Int. J. Plast.*, vol. 5, no. 4, pp. 371–395, 1989.

[47] S. Seelecke, “Modeling the dynamic behavior of shape memory alloys”, *Int. J. Non. Linear. Mech.*, vol. 37, no. 8, pp. 1363–1374, 2002.

[48] A. Paiva and M. A. Savi, “An overview of constitutive models for shape memory alloys,” *Math. Probl. Eng.*, vol. 2006, pp. 1–30, 2006.

[49] C. Cisse, W. Zaki and T. Ben Zineb, “A review of constitutive models and modeling techniques for shape memory alloys”, *Int. J. Plast.*, vol. 76, pp. 244–284, 2016.

[50] F. Auricchio, E. Bonetti, G. Scalet and F. Ubertini, “Theoretical and numerical modeling of shape memory alloys accounting for multiple phase transformations and martensite reorientation”, *Int. J. Plast.*, vol. 59, pp. 30–54, 2014.

[51] Y. Chemisky, A. Duval, E. Patoor and T. Ben Zineb, “Constitutive model for shape memory alloys including phase transformation, martensitic reorientation and twins accommodation”, *Mech. Mater.*, vol. 43, no. 7, pp. 361–376, 2011.

[52] D. Grandi, M. Maraldi and L. Molari, “A macroscale phase-field model for shape memory alloys with non-isothermal effects: Influence of strain rate and environmental conditions on the mechanical response”, *Acta Mater.*, vol. 60, no. 1, pp. 179–191, 2012.

[53] Y. Ivshin and T. J. Pence, “A Thermomechanical Model for a One Variant Shape Memory Material”, *J. Intell. Mater. Syst. Struct.*, vol. 5, no. 4, pp. 455–473, 1994.

[54] M. O. Moussa, Z. Moumni, O. Doaré, C. Touzé and W. Zaki, “Non-linear dynamic thermomechanical behaviour of shape memory alloys”, *J. Intell. Mater. Syst. Struct.*, vol. 23, no. 14, pp. 1593–1611, 2012.

[55] R. B. Gorbet, D. W. L. Wang and K. A. Morris, “Preisach model identification of a two-wire SMA actuator”, *IEEE International Conference on Robotics and Automation*, vol. 3, pp. 2161–2167, 1998.

[56] L. F. Toledo, J. Z. Ge, J. M. Oxoby, Y. Chen and N. O. Perez-Arancibia, “System identification of a NiTi-based SMA actuator using a modified Preisach model and adaptive control,” *American Control Conference (ACC)*, pp. 183–190, 2017.

[57] D. Hughes and J. T. Wen, “Preisach modeling of piezoceramic and shape memory alloy hysteresis”, *Smart materials and structures*, vol. 6, no. 3, pp. 287, 1997.

[58] Y. Matsuzaki, K. Funami and H. Naito, “Inner loops of pseudoelastic hysteresis of shape memory alloys: Preisach approach”, *Smart Structures and Materials: Active Materials: Behavior and Mechanics, SPIE*, vol. 4699, pp. 355–364, 2002.

[59] G. V. Webb, D. C. Lagoudas and A. J. Kurdila, “Hysteresis modeling of SMA actuators for control applications”, *Journal of Intelligent Material Systems and Structures*, vol. 9, no. 6, pp. 432-448, 1998.

[60] M. R. Zakerzadeh, H. Sayyaadi and M. A. V. Zanjani, “Characterizing Hysteresis Nonlinearity Behavior of SMA Actuators by Krasnosel’skii-Pokrovskii Model”, *J. Appl. Math.*, vol. 1, no. 1, pp. 28-38, 2012.

[61] M. F. Al Janaideh and M. F. Al Janaideh, *Generalized Prandtl-Ishlinskii hysteresis model and its analytical inverse for compensation of hysteresis in smart actuators*, Concordia University, 2009.

[62] G. Rizzello, M. A. Mandolino, M. Schmidt, D. Naso and S. Seelecke, “An accurate dynamic model for polycrystalline shape memory alloy wire actuators and sensors”, *Smart Mater. Struct.*, vol. 28, no. 2, pp. 025020, 2019.

[63] S. Seelecke and I. Müller, “Shape memory alloy actuators in smart structures: Modeling and simulation”, *Appl. Mech. Rev.*, vol. 57, no. 1, pp. 23, 2004.

[64] S. Furst, J. Crews and S. Seelecke, “Numerical and experimental analysis of inhomogeneities in SMA wires induced by thermal boundary conditions”, *Contin. Mech. Thermodyn.*, vol. 24, pp. 485-504, 2012.

[65] S. J. Furst and S. Seelecke, “Modeling and experimental characterization of the stress, strain, and resistance of shape memory alloy actuator wires with controlled power input”, *J. Intell. Mater. Syst. Struct.*, vol. 23, no. 11, pp. 1233–1247, 2012.

[66] P. Sedlák, M. Frost, B. Benešová, T. Ben Zineb and P. Šittner, “Thermomechanical model for NiTi-based shape memory alloys including R-phase and material anisotropy under multi-axial loadings”, *Int. J. Plast.*, vol. 39, pp. 132–151, 2012.

[67] D. Cui, G. Song and H. Li, “Modeling of the electrical resistance of shape memory alloy wires”, *Smart Mater. Struct.*, vol. 19, no. 5, p. 055019, 2010.

[68] R. Romano and E. A. Tannuri, “Modeling, control and experimental validation of a novel actuator based on shape memory alloys”, *Mechatronics*, vol. 19, pp. 1169–1177, 2009.

[69] A. R. Shahin, P. H. Meckl and J. D. Jones, “Modeling of SMA Tendons for Active Control of Structures”, *J. Intell. Mater. Syst. Struct.*, vol. 8, no. 1, pp. 51–70, 1997.

[70] E. Williams and M. H. Elahinia, “An Automotive SMA Mirror Actuator: Modeling, Design, and Experimental Evaluation”, *J. Intell. Mater. Syst. Struct.*, vol. 19, no. 12, pp. 1425–1434, 2008.

[71] X. D. Wu, Y. Z. Fan and J. S. Wu, “A study on the variations of the electrical resistance for NiTi shape memory alloy wires during the thermo-mechanical loading”, *Mater. Des.*, vol. 21, no. 6, pp. 511–515, 2000.

[72] X. D. Wu, J. S. Wu and Z. Wang, “The variation of electrical resistance of near stoichiometric NiTi during thermo-mechanic procedures”, *Smart Mater. Struct.*, vol. 8, no. 5, pp. 574–578, 1999.

[73] D. C. Lagoudas, *Shape Memory Alloys: Modeling and Engineering Applications*. Springer, 2008.

[74] K. Cho, J. Rosmarin and H. Asada, “SBC Hand : A Lightweight Robotic Hand with an SMA Actuator Array implementing C-segmentation”, *IEEE Int. Conf. Robot. Autom.*, pp. 921-926, 2007.

[75] J.-M. T. and E. M. R. Tubiana, *Examination of the Hand and the Wrist*. CRC Press, 1998.

[76] B. Siciliano, L. Sciavicco, L. Villani and G. Oriolo, *Robotics: Modelling, Planning and Control*. Springer Science & Business Media, 2009.

[77] S. Furst, *Design, Fabrication , and Control Methods for Exploiting the Multifunctional Sensing and Actuation Capabilities of Shape Memory Alloy Wires*. Saarland University, 2012.

[78] Dynalloy, “Technical Characteristics of FLEXINOL ® Actuator Wires.” [Online]. Available: http://dynalloy.com/pdfs/TCF1140.pdf.

[79] S. Furst and S. Seelecke, “Experimental validation of different methods for controlling a flexible nozzle using embedded SMA wires as both positioning actuator and sensor,” *Behavior and Mechanics of Multifunctional Materials and Composites, SPIE*, vol. 7978, 2011.

[80] S. Vollach and D. Shilo, “The mechanical response of shape memory alloys under a rapid heating pulse”, *Exp. Mech.*, vol. 50, no. 6, pp. 803–811, 2010.

[81] S. Vollach, D. Shilo and H. Shlagman, “Mechanical Response of Shape Memory Alloys Under a Rapid Heating Pulse - Part II”, *Exp. Mech.*, vol. 56, no. 8, pp. 1465–1475, 2016.

[82] Solidwork, http://www.solidworks.it/.

[83] Stratalis, [Online]: http://www.stratasys.com/3d-printers/production-series/connex3-systems.

[84] A. M. Dollar and R. D. Howe, “A robust compliant grasper via shape deposition manufacturing”, *IEEE/ASME Trans. Mechatronics*, vol. 11, no. 2, pp. 154–161, 2006.

[85] M. Cianchetti and C. Laschi, “Pleasant to the Touch: By Emulating Nature, Scientists Hope to Find Innovative New Uses for Soft Robotics in Health-Care Technology”, *IEEE Pulse*, pp. 34–37, 2016.

[86] R. Deimel and O. Brock, “A compliant hand based on a novel pneumatic actuator”, *IEEE International Conference on Robotics and Automation (ICRA)*, pp. 2047–2053, 2013.

[87] R. Deimel and O. Brock, “A novel type of compliant and underactuated robotic hand for dexterous grasping”, *Int. J. Rob. Res.*, vol. 35, pp. 161–185, 2016.

[88] B. S. Homberg, R. K. Katzschmann, M. R. Dogar and D. Rus, “Robust proprioceptive grasping with a soft robot hand”, *Auton. Robots*, vol. 43, no. 3, pp. 681- 696, 2019.

[89] I. Hussain, F. Renda, Z. Iqbal, M. Malvezzi, G. Salvietti, L. Seneviratne and D. Prattichizzo, “Modeling and prototyping of an underactuated gripper exploiting

joint compliance and modularity", *IEEE Robotics and Automation Letters*, vol. 3. No. 4, pp. 2854-2861, 2018.

[90] M. G. Catalano, G. Grioli, E. Farnioli, A. Serio, C. Piazza and A. Bicchi, "Adaptive synergies for the design and control of the Pisa/IIT SoftHand", *Int. J. Rob. Res.*, vol. 33, no. 5, pp. 768–782, 2014.

[91] H. Il Kim, M. W. Han, S. H. Song and S. H. Ahn, "Soft morphing hand driven by SMA tendon wire", *Compos. Part B Eng.*, vol. 105, pp. 138-148, 2016.

[92] H. Rodrigue, W. Wang, D. R. Kim and S. H. Ahn, "Curved shape memory alloy-based soft actuators and application to soft gripper", *Compos. Struct.*, vol. 176, pp. 398-406, 2017.

[93] W. Wang, H. Rodrigue, H.-I. Kim, M.-W. Han and S.-H. Ahn, "Soft composite hinge actuator and application to compliant robotic gripper", *Compos. Part B Eng.*, vol. 98, pp. 397–405, 2016.

[94] F. Simone, G. Rizzello and S. Seelecke, "Metal muscles and nerves—a self-sensing SMA-actuated hand concept", *Smart Mater. Struct.*, vol. 26, no. 9, p. 095007, 2017.

[95] SAES Getters "SmartFlex®" [Online]: https://www.saesgetters.com/sites/default/files/SmartFlex%20Brochure_2.pdf

[96] D. Scholtes, R. Zäh, M. Schmidt, P. Motzki, B. Faupel and S. Seelecke, "Resistance Welding of NiTi Actuator Wires", *Actuator 18 - 16th International Conference on New Actuators*, 2018.

[97] F. Simone, G. Rizzello and S. Seelecke, "A finite element framework for a shape memory alloy actuated finger", *J. Intell. Mater. Syst. Struct.*, vol. 30, no. 14, pp. 2052–2064, 2019.

[98] G. Bunget and S. Seelecke, *BATMAV: A Biologically-Inspired Micro-Air Vehicle for Flapping Flight – Kinematic Modelling*. North Carolina State University, 2007.

[99] S. Hirose and Y. Umetani, "The development of soft gripper for the versatile robot hand", *Mech. Mach. Theory*, vol. 13, no. 3, pp. 351–359, 1978.

[100] L. J. Garner, L. N. Wilson, D. C. Lagoudas and O. K. Rediniotis, "Development of a shape memory alloy actuated biomimetic vehicle", *Smart Mater. Struct.*, vol. 9, no. 5, p. 673, 2000.

[101] J. K. Strelec, D. C. Lagoudas, M. A. Khan and J. Yen, "Design and Implementation of a Shape Memory Alloy Actuated Reconfigurable Airfoil", *Journal of Intelligent Material Systems and Structures*, vol. 14, no 4-5, pp. 257-273, 2003.

[102] L. C. Brinson and R. Lammering, "Finite element analysis of the behavior of shape memory alloys and their applications", *Int. J. Solids Struct.*, vol. 30, no. 23, pp. 3261- 3280, 1993.

[103] P. Terriault, F. Viens and V. Brailovski, “Non-isothermal finite element modeling of a shape memory alloy actuator using ANSYS”, *Comput. Mater. Sci.*, vol. 36, no. 4, pp. 397- 410, 2006.

[104] M. Ben Jaber, H. Smaoui and P. Terriault, “Finite element analysis of a shape memory alloy three-dimensional beam based on a finite strain description”, *Smart Mater. Struct.*, vol. 14, no. 4, p. 045005, 2008.

[105] M. A. El-Sheikh, M. F. Taher and S. M. Metwalli, “New optimum humanoid hand design for prosthetic applications”, *Int. J. Artif. Organs*, vol. 35, no. 4, pp. 251-262, 2012.

[106] N. M. Lewis and S. Seelecke, “FE modeling of multiple SMA wire actuated adaptive structures”, *Behavior and Mechanics of Multifunctional Materials and Composites (SPIE)*, vol. 7978, p. 79781D, 2012.

[107] S. Yang and S. Seelecke, “FE analysis of SMA-based bio-inspired bone–joint system”, *Smart Mater. Struct.*, vol. 18, no. 10, p. 104020, 2009.

[108] COMSOL, “Introduction to COMSOL Multiphysics 5.0”, Manual, 2014.

[109] W. G. Jiang, “A concise finite element model for pure bending analysis of simple wire strand”, *Int. J. Mech. Sci.*, vol. 54, no.1, pp. 69-73, 2012.

[110] Y. Yu, Z. Chen, H. Liu and X. Wang, “Finite element study of behavior and interface force conditions of seven-wire strand under axial and lateral loading”, *Constr. Build. Mater.*, vol. 66, pp.10-18, 2014.

[111] M. Schmidt, J. Ullrich, A. Wieczorek, J. Frenzel, A. Schütze, G. Eggeler and S. Seelecke, “Thermal Stabilization of NiTiCuV Shape Memory Alloys: Observations During Elastocaloric Training”, *Shape Mem. Superelasticity*, vol. 1, no. 2, pp. 132–141, 2015.

[112] C. Urbina, S. De la Flor, F. Gispert-Guirado and F. Ferrando, “New Understanding of the Influence of the Pre-Training Phase Transformation Behaviour on the TWSME in NiTi SMA Wires”, *Exp. Mech.*, vol. 53, no. 8, pp. 1415–1436, 2013.

[113] F. Auricchio, S. Marfia and E. Sacco, “Modelling of SMA materials: Training and two way memory effects”, *Computers & Structures*, vol. 81, no. 24, pp. 2301-2317, 2003.

[114] Y. Liu and H. Yang, “The concern of elasticity in stress-induced martensitic transformation in NiTi”, *Mater. Sci. Eng. A*, vol. 260, pp. 240-245, 1999.

[115] O. Heintze and S. Seelecke, “A coupled thermomechanical model for shape memory alloys-From single crystal to polycrystal”, *Mater. Sci. Eng. A*, vol. 481, pp. 389-394, 2008.

[116] G. Rizzello, M. Schmidt, S. Seelecke, M. Mandolino and D. Naso, “Modeling and Simulation of a Valve System Actuated by Polycrystalline Shape Memory Alloy Wires”, *Adv. Motion Control Conf. (AMC)*, pp. 402-407, 2018.

[117] V. Bundhoo and E. J. Park, “Design of an artificial muscle actuated finger towards biomimetic prosthetic hands”, *12th International Conference on Advanced Robotics (ICAR)*, pp. 368–375, 2005.

[118] Y. Haibin, K. Cheng, L. Junfeng and Y. Guilin, “Modeling of grasping force for a soft robotic gripper with variable stiffness”, *Mech. Mach. Theory*, vol. 128, pp. 254–274, 2018.

[119] A. D. Price, A. Jnifene and H. E. Naguib, “Design and control of a shape memory alloy based dexterous robot hand”, *Smart Mater. Struct.*, vol. 16, no. 4, pp. 1401–1414, 2007.

[120] H. Goldstein, C. Poole and J. Safko, *Classical Mechanics*. 2007.

[121] J. R. Martin, M. L. Latash and V. M. Zatsiorsky, “Coordination of contact forces during multifinger static prehension.”, *J. Appl. Biomech.*, vol. 27, no. 2, pp. 87–98, 2011.

[122] M. Fontana, S. Marcheschi, F. Salsedo and M. Bergamasco, “A Three-Axis Force Sensor for Dual Finger Haptic Interfaces”, *Sensors*, vol. 12, no. 10, pp. 13598–13616, 2012.

8 List of Figures

9 List of Tables

10 Publications

Patents

Roth, Lukas, Simone, Filomena and Thinnes, Felix, " Exoprothese, insbesondere Handprothese", DE 202019105925 U1, 2019.

Peer-reviewed Journal Papers

F. Simone, G. Rizzello and S. Seelecke. "Metal muscles and nerves—a self-sensing SMA-actuated hand concept." *Smart Materials and Structures.* Vol. 26, no. 9, 2017.

F. Simone, P. Linnebach, G. Rizzello and S. Seelecke. "A finite element model of rigid body structures actuated by dielectric elastomer actuators". *Smart Materials and Structures*, vol. 27, no. 6, 2018.

P. Linnebach, F. Simone, G. Rizzello and S. Seelecke. "Development, manufacturing, and validation of a dielectric elastomer membrane actuator–driven contactor". *Journal of Intelligent Material Systems and Structures*, vol. 30, no. 4, pp. 636-648, 2019.

F. Simone, G. Rizzello and S. Seelecke. "A finite element framework for a shape memory alloy actuated finger". *Journal of Intelligent Material Systems and Structures*, vol. 30, no. 14, pp. 2052-2064, 2019.

F. Simone, G. Rizzello, S. Seelecke and P. Motzki. "A soft five-fingered hand actuated by Shape Memory Alloy wires: design, manufacturing, and evaluation." Frontiers in Robotics and AI 7, 2020.

Book Section

F. Simone, P. Motzki, B. Holz and S. Seelecke. "Bio-inspirierter Drei-Finger-Greifer mit Formgedächtnisaktorik." *Technische Unterstützungssysteme*, R. Weidner, T. Redlich and J. P. Wulfsberg, Eds. Hamburg, Germany: Springer Berlin Heidelberg, pp. 194–195, 2015.

S. Seelecke, F. Simone. "Eine bioinspirierte künstliche Hand mit Muskel- und Nervendrähten aus NiTi -A bio-inspired artificial hand with NiTi wires for muscles and nerves", *Orthopädie Technik*, 2016.

Conference Papers and Presentations

P. Motzki, F. Simone and S. Seelecke. “Shape Memory Alloy Actuators in Industrial Applications.” *VDI/VDE-Fachbereich Mechatronik, Robotik und Aktorik, Workshop der Nachwuchswissenschaftler*. VDI, Saarbrücken, Germany, 2014.

F. Simone, P. Motzki, B. Holz and S. Seelecke. “Ein bio-inspirierter 3-Finger-Greifer mit Formgedächtnisaktorik - A Bio-Inspired SMA-Based 3-Finger-Gripper.” *Erste transdisziplinäre Konferenz zum Thema “Technische Unterstützungssysteme, die die Menschen wirklich wollen“,* pp. 420–426, 2014.

P. Motzki, B. Holz, F. Simone and S. Seelecke. “Formgedächtnislegierungen in Applikationen der Greif- und Handhabungstechnologie - Shape Memory Alloys in Applications of Gripping- and Material-Handling-Technology.” *Fachtagung Mechatronik 2015*, pp. 55–60, 2015.

F. Simone, A. York and S. Seelecke. “Design and fabrication of a three-finger prosthetic hand using SMA muscle wires”. In *Bioinspiration, Biomimetics, and Bioreplication 2015, SPIE NDE,* vol. 9429, p. 94290T, 2015.

F. Simone, P. Linnebach, G. Rizzello and S. Seelecke. “FE Simulation eines durch einen dielektrischen Elastomer Aktor (DEA) angetriebenen elektrischen Schützes in COMSOL - FE Simulation of a Dielectric Elastomer Actuator (DEA) driven Contactor in COMSOL.“, *Fachtagung Mechatronik 2017,* 2017.

P. Linnebach, F. Simone and S. Seelecke. “Entwicklung eines durch einen dielektrischen Elastomer-Membran Aktor angetriebenen elektrischen Schützes.“ *Fachtagung Mechatronik 2017,* 2017.

R. Britz et al. “SMA Wire Bundles – Mechanical and Electrical Concepts.” *Actuator 18 - 16th International Conference on New Actuators,* 2018.

F. Simone, G. Rizzello, P. Motzki and S. Seelecke. “Design of a dexterous Finger actuated by SMA bundle wires”. *Technische Unterstützungssysteme, die die Menschen wirklich wollen,* 2018.

P. Loew, G. Rizzello, S. Simone and S. Seelecke. “Finite element simulation of plane strain dielectric elastomer membranes actuated by discretized electrodes”. In *Electroactive Polymer Actuators and Devices (EAPAD) XXI, SPIE NDE, v*ol. 10966, p. 109660W, 2019.

F. Simone, D. Meli, G. Rizzello, D. Naso and S. Seelecke. “Finite element modeling and simulation of a robotic finger actuated by Ni-Ti shape memory alloy wires”. In *Behavior and Mechanics of Multifunctional Materials XIII* , *SPIE NDE*, vol. 10968, p. 109680F, 2019.

F. Simone, G. Rizzello, S. Seelecke, S. Borreggine, and D. Naso. “Modeling and Identification of a Shape Memory Alloy Robotic Finger Actuator”. In *) IEEE 18th European Control Conference (ECC)*, pp. 1097-1102, 2019.

Acknowledgments

I am grateful to a number of friends and colleagues who encouraged me to persevere during my PhD journey.

Foremost, I would like to express my sincere gratitude to my advisor Prof. Stefan Seelecke, for his continuous support during my research, his patience and enthusiasm. His guidance helped me even when I was demotivated or whenever I lost the right path. I can say that now I know to whom I would like to resemble.

I would like to thank Prof. Matthias Nienhaus for agreeing to oversee my defense and review this dissertation.

A special thanks goes to the entire iMSL Team, former and present members, who always cheered me up and gladdened my working days. Thanks to them, I never had one boring or uninteresting day during my permanence at Zema.

I would like to thank Federica, Paul, Gloria, Arianna and the little Mathy, all members of my second family here in Saarbrücken.

Finally, I would like to thank my husband. It is difficult to express with words my gratitude for all the love, emotional support, encouragements he gave me in these years. He really inspired me to continuously improve and, I am sure, I will never be able to adequately repay his endless care.

11 Eidesstattliche Versicherung

Hiermit versichere ich an Eides statt, dass ich die vorliegende Arbeit selbstständig und ohne Benutzung anderer als der angegebenen Hilfsmittel angefertigt habe. Die aus anderen Quellen oder indirekt übernommenen Daten und Konzepte sind unter Angabe der Quelle gekennzeichnet. Die Arbeit wurde bisher weder im In- noch im Ausland in gleicher oder ähnlicher Form in einem Verfahren zur Erlangung eines akademischen Grades vorgelegt.

Ort, Datum

_____

Unterschrift

_____